

**Synthesis and Characterization of  $\text{TiO}_2\text{-Bi}_{0.9}\text{Ho}_{0.1}\text{FeO}_3$   
Composite Thin Film**

by

Md. Rafiqul Islam

MASTER OF SCIENCE IN MATERIALS AND METALLURGICAL ENGINEERING



Department of Materials and Metallurgical Engineering

BANGLADESH UNIVERSITY OF ENGINEERING AND TECHNOLOGY

July, 2018

## **CANDIDATE'S DECLARATION**



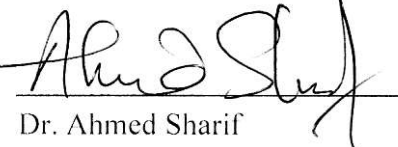

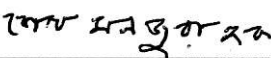
IT IS HEREBY DECLARED THAT THIS THESIS PAPER OR ANY PART OF IT HAS  
NOT BEEN SUBMITTED ANYWHERE ELSE FOR THE AWARD OF ANY DEGREE

-----

**Md. Rafiqul Islam**  
**B.Sc. Engg., MME, BUET**

The thesis titled “**Synthesis and Characterization of  $\text{TiO}_2\text{-Bi}_{0.9}\text{Hf}_{0.1}\text{FeO}_3$  Composite Thin Film**” submitted by Md. Rafiqul Islam, Student No. 1015112017, Session October 2015 has been accepted as satisfactory in partial fulfillment of the requirements for the degree of Master of Science in Materials and Metallurgical Engineering on July 4, 2018.

### BOARD OF EXAMINERS

- (i)   
Dr. A. K. M. Bazlur Rashid  
Professor, Department of MME  
BUET, Dhaka-1000  
Supervisor  
(Chairman)
- (ii)   
Dr. Md. Moniruzzaman  
Professor, Head, Department of MME  
BUET, Dhaka-1000  
Member  
(Ex-Officio)
- (iii)   
Dr. Ahmed Sharif  
Professor, Department of MME  
BUET, Dhaka-1000  
Member
- (iv)   
Dr. Kazi Md. Shorowordi  
Professor, Department of MME  
BUET, Dhaka-1000  
Member
- (v)   
Dr. Engr. Sheikh Monjura Hoque  
Chief Scientific Officer and  
Head, Materials Science Division  
Atomic Energy Centre, Dhaka-1000  
Member  
(External)

## **DEDICATION**

To My beloved Parents  
And  
Teachers

## ACKNOWLEDGEMENTS

Alhamdulillah, all praises to almighty Allah for the strengths and His blessing in completing this thesis.

I would like to express my sincere gratitude to my thesis supervisor Prof. A. K. M. B. Rashid for his kind supervision, indispensable guidance, valuable and constructive suggestions, liberal help and continuous encouragement during this thesis work. I truly appreciate and value his esteemed guidance and encouragement from the beginning to the end of this thesis.

I would like to thank Prof. Md. Moniruzzaman, Head, MME, for his continuous support and encouragement to excel in research and academia, and for allowing me to use the various facilities of MME without hindrance. The same gratitude goes to Dr. M. A. Matin, Head, GCE, and all of its members. Without their constant assistance this work would not have been possible. Without the lab facilities and raw materials provided by GCE my research project would have remained undone.

I am immensely grateful to Dr. M. A. Zubair, Assistant Professor, GCE, BUET, for his interest in my work, and encouragement and insight through these years. It was his guidance and support that helped me through all the difficult time. Without his co-operation with many experimental aspects, especially XRD and UV-Vis spectrometer, this project would have remained incomplete.

I profoundly thank Mr. M. S. Bashar, Senior Scientific Officer, IFRD, BCSIR for letting me use the hall effect measurement system, giving me permission to use various facilities available and for the support and advice he continues to give me, without which the research work would have become unduly lengthened.

I am grateful to Dr. Sheikh Manjura Hoque, Head, Materials Science Division, AECD, for her permission to use vibrating sample magnetometer equipment.

Above all, I would like to thank all my family members and friends whose direct and indirect support helped me completing my project in time.

## ABSTRACT

A visible light active  $\text{TiO}_2$  -  $\text{Bi}_{0.9}\text{Ho}_{0.1}\text{FeO}_3$  nanoparticles composite thin films with different mol. % of  $\text{Bi}_{0.9}\text{Ho}_{0.1}\text{FeO}_3$  were successfully prepared via non-aqueous sol-gel method. The incorporation of 5, 10 and 20 mol. %  $\text{Bi}_{0.9}\text{Ho}_{0.1}\text{FeO}_3$  nanoparticles in the precursor solution of  $\text{TiO}_2$  brings modifications in the functional properties of the composite thin films. X-ray diffraction analysis confirms that  $\text{TiO}_2$  and  $\text{Bi}_{0.9}\text{Ho}_{0.1}\text{FeO}_3$  retain anatase and orthorhombic phase respectively in composite films. Field emission scanning electron microscopy reveals that small clusters of  $\text{Bi}_{0.9}\text{Ho}_{0.1}\text{FeO}_3$  nanoparticles are distributed throughout the  $\text{TiO}_2$  matrix. The composite thin film containing 20 mol.%  $\text{Bi}_{0.9}\text{Ho}_{0.1}\text{FeO}_3$  nanoparticles exhibits the most prominent absorption phenomenon in visible region and has significantly reduced indirect band gap of 2.46 eV compared to that of pure  $\text{TiO}_2$  (3.4 eV). Hall effect measurements affirm that the resistivity of composite film increases by  $\sim 2.33$  orders of magnitude and its carrier concentration decreases by 1.8 orders of magnitude at 5 mol.%  $\text{Bi}_{0.9}\text{Ho}_{0.1}\text{FeO}_3$  nanoparticles addition compared to the pure  $\text{TiO}_2$  film. Moreover, the pure film exhibits diamagnetism, whereas the composite films have both large ferromagnetic and small diamagnetic components. The diamagnetic susceptibility of composite films decreased 4.8 times compared to pure one at 20 mol. %  $\text{Bi}_{0.9}\text{Ho}_{0.1}\text{FeO}_3$  addition

# TABLE OF CONTENTS

CANDIDATE’S DECLARATION .....	ii
ACKNOWLEDGEMENTS.....	v
ABSTRACT.....	vi
LIST OF FIGURES .....	xi
LIST OF TABLES.....	xv
<b>1 INTRODUCTION.....</b>	<b>1</b>
1.1 Introduction and Motivation .....	2
1.2 Objectives of The Present Study.....	4
<b>2 LITERATURE REVIEW.....</b>	<b>5</b>
2.1 Titania (TiO <sub>2</sub> ).....	6
2.1.1 Crystal structure of TiO <sub>2</sub> phase.....	6
2.1.2 Optical properties.....	7
2.1.2.1 The electronic structures of intrinsic TiO <sub>2</sub> materials .....	7
2.1.2.2 Band gap engineering of TiO <sub>2</sub> .....	9
2.1.3 Magnetism of TiO <sub>2</sub> .....	15
2.1.3.1 Types of magnetism.....	15
2.1.3.2 Tuning of magnetism in TiO <sub>2</sub> .....	17

2.1.4 Electrical properties of TiO <sub>2</sub> .....	22
2.1.4.1 Engineering of electrical properties in TiO <sub>2</sub> .....	23
2.1.5 Application of TiO <sub>2</sub> .....	24
2.1.5.1 Visible light photocatalysis of TiO <sub>2</sub> on organic compounds .....	24
2.1.5.2 TiO <sub>2</sub> in spintronics .....	28
2.1.6 Processing of TiO <sub>2</sub> film .....	29
2.1.6.1 Spray pyrolysis deposition technique .....	29
2.1.6.2 Pulse laser deposition technique .....	30
2.1.6.3 Spin coating method .....	31
2.2 Bismuth Ferrite (BiFeO <sub>3</sub> ).....	34
2.2.1 Crystal structure of BiFeO <sub>3</sub> .....	37
2.2.2 Magnetism of BiFeO <sub>3</sub> .....	39
2.2.2.1 Tuning of magnetism in BiFeO <sub>3</sub> .....	40
2.2.3 Electrical properties of BiFeO <sub>3</sub> .....	42
2.2.3.1 Engineering of electrical properties in BiFeO <sub>3</sub> .....	42
2.2.4 Optical properties of BiFeO <sub>3</sub> .....	43
2.2.4.1 Tuning of optical properties in BiFeO <sub>3</sub> .....	44
2.2.5 Application of BiFeO <sub>3</sub> .....	44
2.2.5.1 Ferroelectric and piezoelectric devices .....	44
2.2.5.2 Spintronics .....	45
2.2.5.3 Photocatalyst .....	48



2.2.6 Synthesis of BiFeO <sub>3</sub> .....	48
2.2.6.1 Microwave associated hydrothermal synthesis.....	49
2.2.6.2 Co-precipitation route .....	50
2.2.6.3 Pechini sol-gel route .....	50
<b>3 EXPERIMENTAL .....</b>	<b>52</b>
3.1 Introduction.....	53
3.2 Materials .....	53
3.3 Synthesis of BHFO Nanoparticles .....	53
3.4 Synthesis of Thin Films .....	54
3.4.1 Synthesis of pure titania (TiO <sub>2</sub> ) thin film .....	54
3.4.2 Synthesis of TiO <sub>2</sub> - BHFO composite thin film.....	54
3.5 Characterization .....	55
3.5.1 Field emission scanning electron microscopy (FESEM).....	55
3.5.2 Crystal structure determination and phase identification.....	56
3.5.3 Optical absorption measurement.....	56
3.5.4 Magnetic properties determination .....	56
3.5.5 Electrical characterization.....	56
<b>4 RESULTS AND DISCUSSION.....</b>	<b>57</b>
4.1 X-Ray Diffraction Analysis .....	58

4.2 Morphological And Elemental Analysis.....	63
4.3 Optical Properties Study .....	67
4.4 Electrical Properties Analysis .....	73
4.5 Magnetic Properties Study.....	76
<b>5 CONCLUSION .....</b>	<b>80</b>
<b>6 SUGGESTION FOR FUTURE WORK.....</b>	<b>83</b>
<b>REFERENCE.....</b>	<b>85</b>

## LIST OF FIGURES

Fig. 2.1. The octahedrons of (a) rutile and (b) anatase structure. <sup>29</sup> .....	6
Fig. 2.2. Crystal structures of anatase and rutile <sup>29</sup> .....	7
Fig. 2.3. Energy band structures of TiO <sub>2</sub> . <sup>29</sup> .....	8
Fig. 2.4. Diffuse reflectance UV-visible spectra of TiO <sub>2</sub> implanted with (a) V, (b) Cr, (c) Fe, (d) Ni ions <sup>46</sup> .....	10
Fig. 2.5. The optical absorption curves calculated for various N concentrations in the polycrystalline TiO <sub>2</sub> : (I) undoped TiO <sub>2</sub> ; (II) 12.5 mol.% nitrogen doped; (III) 6.2 mol.% nitrogen doped; and (IV) 3.1 mol.% nitrogen doped. <sup>52</sup> .....	11
Fig. 2.6. UV-Vis absorption spectra of amorphous TiO <sub>2</sub> nanoparticles, ZnO nanorods, TZO nano hybrids and the annealed products TZO300 and TZO600. <sup>16</sup> .....	12
Fig. 2.7. Enhanced photocatalytic performance of TiO <sub>2</sub> -ZnO hybrid nanostructures <sup>16</sup> .....	13
Fig. 2.8. Postulate of the visible light-induced photodegradation mechanism of BiFeO <sub>3</sub> /TiO <sub>2</sub> nanofibers <sup>18</sup> .....	14
Fig. 2.9. UV-vis spectra of (a) TiO <sub>2</sub> , (b) TiO <sub>2</sub> -5% BiFeO <sub>3</sub> , (c) TiO <sub>2</sub> - 8%BiFeO <sub>3</sub> , (d) TiO <sub>2</sub> -10%BiFeO <sub>3</sub> , (e) TiO <sub>2</sub> - 15%BiFeO <sub>3</sub> , (f) TiO <sub>2</sub> - 20%BiFeO <sub>3</sub> (g) BiFeO <sub>3</sub> <sup>18</sup> .....	14
Fig. 2.10. Example Tauc plot extrapolations showing the spectra of the as-deposited C <sup>33</sup> T <sup>67</sup> films. Here C <sup>33</sup> T <sup>67</sup> stands for 33% CdSe and 67% TiO <sub>2</sub> . <sup>19</sup> .....	15
Fig. 2.11. Common examples of magnetic dipole ordering <sup>55</sup> .....	16
Fig. 2.12. Electronic configuration of Ti atom. ....	18
Fig. 2.13. M–H curves of Mn-doped TiO <sub>2</sub> at 400, 500 and 600 °C. The inset shows M–H curve of undoped TiO <sub>2</sub> . <sup>61</sup> .....	20

Fig. 2.14. Magnetization versus the magnetic field at 300 K for TiO <sub>2</sub> single crystals, annealed in O <sub>2</sub> at 1173 K for 2 h, 5 h, and 8 h. The anomalous protrusions in the curve are described by arrows. Note that the signals of substrates were removed. <sup>63</sup> .....	21
Fig.2.15. Magnetic hysteresis loop at 300K of magnetic iron oxide (Fe <sub>3</sub> O <sub>4</sub> ), TiO <sub>2</sub> /Fe <sub>3</sub> O <sub>4</sub> and TiO <sub>2</sub> /SiO <sub>2</sub> /Fe <sub>3</sub> O <sub>4</sub> nanoparticles <sup>65</sup> .....	22
Fig. 2.16. Schematic diagram of photocatalysis process of TiO <sub>2</sub> <sup>73</sup> . .....	24
Fig. 2.17. (A) spray pyrolysis apparatus used and (B) substrate and holder .....	29
Fig. 2.18. Illustration of pulsed laser deposition process.....	31
Fig. 2.19. Simplified chart of sol-gel technologies and their application. ....	32
Fig. 2.20. Schematic view of the R3c structure built up from two cubic perovskite BFO unit cells. The cations are displaced along the [111] direction relative to the anions, and the oxygen octahedra rotate with alternating sense around the [111] axis. In the ideal cubic perovskite structure the oxygen ions would occupy the face-centered sites. ....	35
Fig. 2.21. (a) Magnetization versus magnetic field curves and (b) Electric field dependence of polarization (P–E) hysteresis loops for Bi <sub>1-x</sub> Ho <sub>x</sub> FeO <sub>3</sub> samples where x= 0.0,0.05, 0.1 25.....	36
Fig. 2.22. Schematic illustration of a structural transition process (a) ideal cubic structure Pm-3m without tilting (a0a0a0); (b) R-3c structure tilted along three axes with the same angle (a-a-a-); (c) Displacement of Bi ion towards [111] direction based on R3c. ....	37
Fig. 2.23. Crystal structure of bismuth ferrite (a) in the hexagonal setting, (b) in the hexagonal setting with the distorted perovskite sub-structure shown, and (c) viewed along the c-axis. In the figure, the displacement of the Bi <sup>2+</sup> ions along the [001] direction can be easily seen. ....	38
Fig. 2.24. Schematic showing different types of magnetic ordering – the last three are types of antiferromagnetism .....	40
Fig. 2.25. Spin canting due to anti-symmetric exchange.....	40
Fig. 2.26: Schematics of the 64 nm antiferromagnetic circular cycloid. ....	41

Fig. 2.27. Band structure for doped BFO.....	43
Fig. 2.28. MERAM based on exchange-bias coupling between a multiferroic that is ferroelectric and antiferromagnetic (FE-AFM, green layer), and a thin ferromagnetic electrode (blue). A tunneling barrier layer between the two top ferromagnetic layers provides the two resistive states. Interestingly, BFO could act not only as the magnetoelectric active layer, but also as the tunneling barrier. ....	47
Fig. 2.29. (a) The experiment device schematic diagrams for synthesis and (b) reaction.....	49
Fig. 3.1. Schematic representation of preparation process of composite thin films .....	55
Fig.4.1. XRD patterns of the prepared pure film, composite films and nanoparticles. Here B and T stand for some major peaks of BHFO and TiO <sub>2</sub> respectively.....	58
Fig. 4.2. Magnified XRD patterns of BHFO nanoparticles in the range of (a) 2 theta/degree = 21.5-23.5° and (b) 2 theta/degree = 30- 34°. ....	59
Fig. 4.3. Plot showing the observed (red dot), calculated (black line), and difference (blue line) patterns obtained from Rietveld refinement. First and second row of ticks indicates Bragg positions for the Pnma phase and Pbam phase respectively. ....	60
Fig. 4.4. FESEM images of (a) BHFO nanoparticles (b) TiO <sub>2</sub> film (c) T <sup>95</sup> B <sup>5</sup> film (d) T <sup>90</sup> B <sup>10</sup> film and (e) T <sup>80</sup> B <sup>20</sup> film along with the films' cross-section micrographs. The magnification for all the images is x50000. ....	64
Fig. 4.5. Elemental mapping of (b) Ti (green), (c) Bi (blue), (d) Ho (pink), (e) Fe (yellow), and (f) O (red) taken from the selected area of the FESEM image of T <sup>95</sup> B <sup>5</sup> film as shown in (a). (g) EDS pattern with the composition of the elements for the film.....	66
Fig. 4.6. UV-vis absorbance spectra of films. The inset shows the absorbance spectra of BHFO nanoparticles. ....	68
Fig. 4.7. (a) [E*F(R)] <sup>2</sup> vs energy, E plot to calculate band gap energy of nanoparticles (b) indirect and (c) direct Tauc's plots demonstrating the band gap energies of pure and composite thin films .....	69

Fig. 4.8. Schematic illustration for the calculated energy level diagram indicating the conduction and valence band potentials of TiO<sub>2</sub> film and BHFO nanoparticles. .... 72

Fig. 4.9. (a) Resistivity, carrier concentration and mobility of films with different mol. % of BHFO (b) Conductivity ( $\Omega$  -cm) vs. Electric Field, E (kV/cm) plot of BHFO nanoparticles. .... 74

Fig. 4.10. Room temperature (a) M-H hysteresis loop for BHFO nanoparticles with inset showing its magnified M-H loop (b) M-H hysteresis loops for pure and composite films with inset showing magnified M-H loops of T<sup>95</sup>B<sup>5</sup>, T<sup>90</sup>B<sup>10</sup> and T<sup>80</sup>B<sup>20</sup> films. .... 78

Fig. 4.11. Diamagnetic susceptibility of films with different mol. % of BHFO nanoparticles 79

## LIST OF TABLES

Table 2.1: Comparison of the electron configurations and unpaired electrons for various ions .....	19
Table 4.1. Summary of data obtained from Rietveld refinement and agreement factors of BHFO nanoparticles .....	61
Table 4.2. Position ( $2\theta$ ) and lattice parameters values obtained from XRD for pure film and composite films.....	62
Table 4.3. EA, FIP, and calculated electronegativity for several atoms.....	71

# **1 INTRODUCTION**



## 1.1 Introduction and Motivation

TiO<sub>2</sub> as powders or thin film has been comprehensively investigated due to their excellent photo-chemical stability, low cost and non-toxicity.<sup>1</sup> However, pure TiO<sub>2</sub> responds only to ultraviolet (UV) light, which comprises only 4% of the total sunlight. The absorption occurs in the UV light due to large band gap (3.2 eV), which eventually restricts its practical application in degradation of organic pollutants such as dyes, detergents and pesticides etc.<sup>1-4</sup> Besides, diamagnetism and lower resistivity of the TiO<sub>2</sub> have become a concern in the field of spintronics, resistors, sensors and multistate memory devices.<sup>5,6</sup> These limitations have galvanized endeavors to enhance photocatalytic activity, induce magnetism and raise resistivity of TiO<sub>2</sub>.

One of the attempts is to substitute a portion of the titanium with different electropositive atoms. Transition metals (e.g. Fe, Mn, Cr etc ) are the most commonly used constituents that induce visible light absorption.<sup>2-4</sup> Besides, transition metal (TM) doped TiO<sub>2</sub> has exhibited improved ferromagnetism at room temperature.<sup>7,8</sup> Moreover, Mn and Fe dopants in TiO<sub>2</sub> have increased the resistivity significantly.<sup>7,8</sup> Another endeavor involves substitution of oxygen with electronegative atoms (N, C and S) which aids TiO<sub>2</sub> to absorb visible light efficiently.<sup>9</sup> However, the introduction of substitutional elements creates scattering centers, which decrease the photochemical activity. It has been reported that substitutional TM serves as a center for charge carrier recombination.<sup>2</sup> Besides, it has been controversial as to whether Co or Fe doped TiO<sub>2</sub> is a true magnetic semiconductor or if the effect is due to the clustering of a ferromagnetic second phase.<sup>10,11</sup> Indeed, according to these reports doped TiO<sub>2</sub> has failed to exhibit magnetism to any greater extent.

Since, the physical quantities like electrical, magnetic, and optical properties come in the category of sum or product properties, many have tried to make composites of TiO<sub>2</sub> to utilize this criteria.<sup>12,13</sup> Magnetic properties have been improved by the fabrication of Fe<sub>x</sub>O<sub>y</sub>-TiO<sub>2</sub> or TiO<sub>2</sub>-Fe<sub>3</sub>O<sub>4</sub>-SiO<sub>2</sub> composites.<sup>14,15</sup> Similarly the nanostructured ZnO/ TiO<sub>2</sub> has been found to improve the optical properties, even though, ZnO is a wide band gap semiconductor.<sup>16</sup> Now-a-days, the visible light activity of titanium is increased by coupling TiO<sub>2</sub> with other narrow bandgap semiconductors. The proposition is that coupled semiconductors form a hetero-junction structure which can transfer electrons from an excited small band gap semiconductor into another attached one in the case of proper band potentials. In<sub>2</sub>O<sub>3</sub><sup>17</sup>, BiFeO<sub>3</sub><sup>18</sup> or CdSe co-

sensitized TiO<sub>2</sub><sup>19</sup> heterostructures have been reported for showing better visible light activity. Multiferroic BiFeO<sub>3</sub> (BFO) deserves a special mention for its narrow band gap (2.2 eV) and chemical stability which have made it a suitable visible- light responsive photocatalyst.<sup>1</sup> The coupling of TiO<sub>2</sub> with BFO has been accomplished through different synthesis processes. For instance, core-shell structured BFO/TiO<sub>2</sub> by hydrolysis precipitation approach,<sup>1</sup> deposition of TiO<sub>2</sub> on ferroelectric BFO substrate by pulsed laser deposition,<sup>20</sup> growth of TiO<sub>2</sub> nanofibers on BFO nanoparticles by electrospinning.<sup>18</sup> These reports focus on enhancing visible light activity of TiO<sub>2</sub>. Subsequently, several studies ponder on improving electrochemical energy storage capacity and solar energy conversion efficiency of titania by anchoring BFO nanoparticles on TiO<sub>2</sub>.<sup>21,22</sup>

The magnetic and electrical properties (e.g. resistivity, carrier concentration and mobility) still remain unreported with BFO nanoparticles due to its various limitations. Literature survey indicates that BFO nanoparticles are antiferromagnetic<sup>23</sup> and have higher leakage current due to oxygen vacancies (OVs) formation.<sup>24</sup> Recently, doping with tri-positive rare-earth ions (R<sup>3+</sup>) at the Bi site has been proposed to mitigate some of the issues mentioned above.<sup>25</sup> Previous reports suggest that 10 mol.% Holmium (Ho<sup>3+</sup>) doping at Bi site increases the magnetization by 6 times compared to pure BFO and exhibits higher resistivity than the pure one.<sup>25</sup> Since Ho<sup>3+</sup> is a rare earth metal it is expected that Bi<sub>0.9</sub>Ho<sub>0.1</sub>FeO<sub>3</sub> nanoparticles will have better absorbance in the visible region and lower band gap than BFO.<sup>23</sup> The aforementioned advantages make Bi<sub>0.9</sub>Ho<sub>0.1</sub>FeO<sub>3</sub> nano particles a good candidate for incorporation in TiO<sub>2</sub>.

TiO<sub>2</sub> thin film is a better candidate for spintronics, sensors and magnetic memory devices creating faster, smaller and more energy efficient devices compared to titania nanoparticles, nanowire, nanorod or nanofiber. Both undoped and doped TiO<sub>2</sub> thin films have been of immense interest due to their enhanced photocatalytic activity, better electrical properties and room temperature ferromagnetism.<sup>3,7,26,27</sup> To the best of our knowledge the optical, magnetic and electrical properties based on incorporation of Bi<sub>0.9</sub>Ho<sub>0.1</sub>FeO<sub>3</sub> nanoparticles in TiO<sub>2</sub> thin film have not been explored yet. Herein motivated by the above concerns, TiO<sub>2</sub> - Bi<sub>0.9</sub>Ho<sub>0.1</sub>FeO<sub>3</sub> composite thin films were prepared by non-aqueous sol-gel method and their structural, magnetic, optical and electrical properties were investigated in detail.

## 1.2 Objectives of The Present Study

The specific aim of this work is to focus on the synthesis of  $\text{TiO}_2\text{-Bi}_{0.9}\text{Ho}_{0.1}\text{FeO}_3$  composite thin film with a concentration on improving the optical, electrical and magnetic properties of the material.

Keeping this in mind, there are two principal objectives of this work. These are:

- (a) Synthesis of  $\text{TiO}_2\text{-Bi}_{0.9}\text{Ho}_{0.1}\text{FeO}_3$  composite thin film, and
- (c) Investigation of the structural and functional properties of  $\text{Bi}_{0.9}\text{Ho}_{0.1}\text{FeO}_3$  nanoparticles,  $\text{TiO}_2$  thin film and  $\text{TiO}_2\text{-Bi}_{0.9}\text{Ho}_{0.1}\text{FeO}_3$  composite thin film.

The expected outcome of this research work is that the composite thin film will have good magnetic properties and reduced band gap energy. This will have a two-fold benefit. Firstly, having a lower band gap will make this composite a good candidate for solar cells and optoelectronic devices in the visible region. Secondly, good magnetic properties and reduced band gap energy will make this composite a magnetoresistive material, suitable for using in magnetic data storage technology. Besides, the composite will also find applications in spintronics, actuators, and sensor devices due to the existence of both ferroelectric and ferromagnetic ordering.

# **2 LITERATURE REVIEW**

## 2.1 Titania (TiO<sub>2</sub>)

### 2.1.1 Crystal structure of TiO<sub>2</sub> phase

TiO<sub>2</sub> materials naturally occur in three available crystal forms, known as anatase, rutile and brookite, in which well crystallized anatase and rutile have been widely studied owing to their practical uses. Both anatase and rutile phase of TiO<sub>2</sub> crystal structures are comprised of  $TiO_6^-$  octahedrons that each Ti atom is surrounded octahedrally by six oxygen atoms, as that presented in Fig. 2.1. Actually, the octahedrons in both structures are more or less distorted leading to two kinds of bonds between titanium and oxygen atoms in  $TiO_6^-$  octahedron no matter the phases, marked as  $T - O_1$  and  $T - O_2$  in Fig. 2.1. In rutile, the distortion of octahedron only stretches the  $T - O_2$  bonds along diagonal direction, resulting in longer TiO<sub>2</sub> bonds along diagonal direction than the other four  $T - O_1$  bonds in lateral plane, the angles between  $T - O_1$  and  $T - O_2$  bonds are still 90°. While in anatase structure, except for the stretching of  $T - O_2$  bonds,  $T - O_1$  bonds are deviated from lateral plane therefore the angles between TiO<sub>1</sub> and TiO<sub>2</sub> are not now 90°.  $T - O_2$  bonds in both structures have the same distance of 0.198 nm while the  $T - O_1$  bond in anatase is shorter than that in rutile, with distances of 0.1934 nm versus 0.1949 nm.<sup>28</sup>

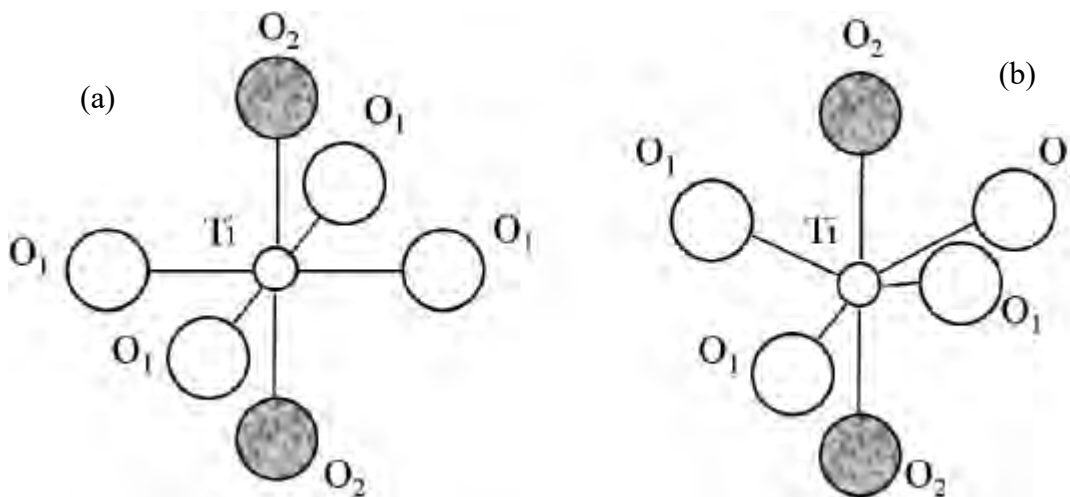


Fig. 2.1. The octahedrons of (a) rutile and (b) anatase structure.<sup>29</sup>

The connecting manners with different lattice distortion lead to different crystal structures with corresponding chemical and physical properties though both of them have tetragonal lattice structure. As shown in Fig. 2.2, each distorted octahedron in rutile contacts with ten neighbour octahedrons, in which two share edge oxygen pairs and eight share corner oxygen atoms forming a liner chain. Each octahedron in anatase is connecting with eight neighbours, four sharing edges and four sharing corners, to form a zig-zag chain.<sup>30</sup> The difference in distortion and connecting manner results in distinctive Ti-Ti distances, 0.379 nm and 0.304 nm in anatase versus 0.357 nm and 0.296 nm in rutile. Therefore, anatase phase is considered to have a more open structure with corresponding higher specific surface.

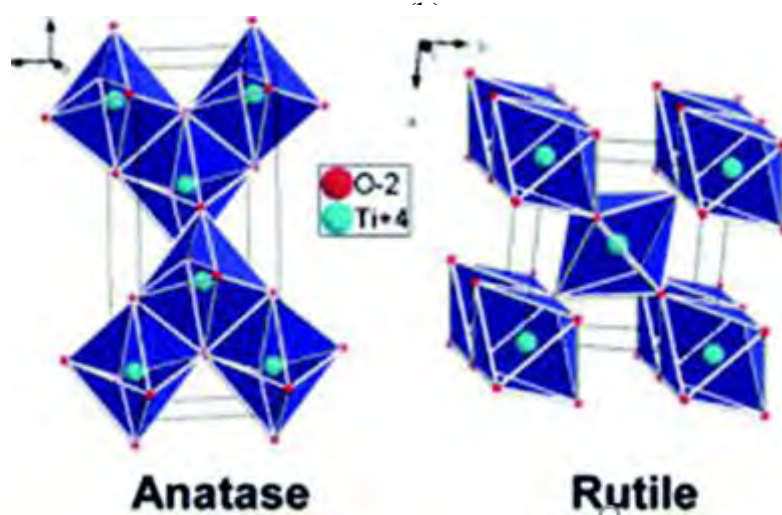


Fig. 2.2. Crystal structures of anatase and rutile<sup>29</sup>

## 2.1.2 Optical properties

### 2.1.2.1 The electronic structures of intrinsic TiO<sub>2</sub> materials

Electrons in the crystalline semiconductors are confined to certain energy levels, which are also known as electron movement orbitals, and forbidden from other region, as shown in Fig. 2.3. The highest range of energy levels which electrons occupy at absolute zero degree is called valence band and the range of energy levels, higher than that, is called conduction band. Each energy band has a large number of quantum states. The valence band describes a state of electrons tightly bound to the atomic nuclei and the conduction band reflects the electrons

escaped from the materials to move entirely free in crystal lattice. As for  $\text{TiO}_2$ , the bottom of the conduction band (CB) is dictated by the Ti 3d electron states and the top of the valence band (VB) is dominated by the oxygen 2p electron states. The energy difference between the top of valence band and the bottom of conduction band is dubbed as band gap ( $E_g$ ). Therefore, the band gap determines the specific minimum amount of energy in order for an electron to jump from valence band to conduction band. When a semiconductor is illuminated with light of energy higher than the band gap, electrons receive the energy from incident photons and jump from the valence band to the conduction band leaving as many positive holes in the valence band. This process is equivalent to the movement of electrons from bonding orbital to anti-bonding orbital.

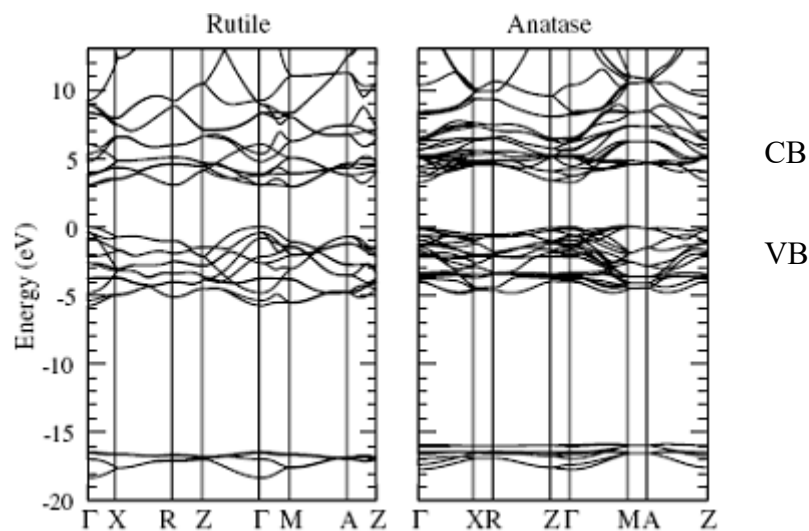


Fig. 2.3. Energy band structures of  $\text{TiO}_2$ .<sup>29</sup>

In most cases, the excited electrons are unstable and can easily jump back into the valence band and recombine with holes quickly with the release of heat. There are two kinds of band gaps, direct band gap which means carriers at the highest point of valence band and the lowest point of conduction band have the same momentum and electrons can directly jump into conduction band without changing momentum, and indirect band gap which means electrons must pass through an intermediate state to reach conduction band and transfer momentum to crystal lattice. Rutile phase  $\text{TiO}_2$  has a direct band gap of 3.0 eV while anatase phase has an indirect band gap of 3.2 eV.

### 2.1.2.2 Band gap engineering of TiO<sub>2</sub>

As it was mentioned, the functionality for pure TiO<sub>2</sub> can be excited only by ultraviolet (UV) light that only accounts for less than 5% of solar irradiance because of the wide band gaps (3.2 eV for anatase and 3.0 eV for rutile). This wide gap nature of TiO<sub>2</sub> phases seriously limits their practical applications in most circumstances including photocatalysis, photo induced hydrophilicity and production of hydrogen, as the UV light can be readily absorbed even by pure water vapor and clear glass. It is very important and urgent therefore to fabricate modified TiO<sub>2</sub> thin films and powders with a narrowed band gap to utilize the visible light from solar irradiance. To extend the light absorption spectrum toward the visible light range, intense efforts have been made in order to modify the optical absorption properties of TiO<sub>2</sub> phases, including ions doping and compositing TiO<sub>2</sub> with other semiconductors of narrower band gap. The most feasible modification method seems to be doping TiO<sub>2</sub> with metal and nonmetal atoms to tune the band structures.<sup>31,32</sup> Although TiO<sub>2</sub> materials have been widely explored by doping and making composites, the extensive exploration of TiO<sub>2</sub>, especially experimental research, has never been concluded because the practical application of TiO<sub>2</sub> under visible light is nevertheless restricted.

#### *Single metal ions doped TiO<sub>2</sub>*

The main objective of single metal ions doping on band gap narrowing is to shift up valence band or shift down conduction band of intrinsic TiO<sub>2</sub> or create shallow intermediate band levels into forbidden band through substituting Ti atoms by dopants in TiO<sub>2</sub> lattice, since deep intermediate band levels would predicatively act as recombination centre and thereby arouse significant electron and hole recombination. On the ground of this, various single metal ions have been widely studied to address the optical limitation of TiO<sub>2</sub> materials, including transition metal (such as V<sup>4</sup>, Cr<sup>4,33</sup>, Mn<sup>3,34</sup>, Fe<sup>2,35</sup>, Co<sup>36</sup>, Ni<sup>37</sup>, Cu<sup>38</sup>, rare earth metals<sup>39-41</sup> such as Ce<sup>42</sup>, Sm<sup>43</sup>, other metals such as Mg<sup>44</sup>, Sr<sup>45</sup> and so on.

Among these, TM ions, especial 3d transition metal ions has merited extensive attention, since substituting Ti atoms by these ions would result in mixing of intrinsic energy and of TiO<sub>2</sub> with partial occupied d orbitals of dopants, and thus being expected to effectively alter the electronic structure of TiO<sub>2</sub>. Another attractive reason for the extensive studies on 3d transition ions



doping is their comparable ionic size to  $\text{Ti}^{4+}$ , which is not expected to introduce serious lattice distortion and defect states into  $\text{TiO}_2$  crystal and would be much easier to be incorporated into  $\text{TiO}_2$  matrix. Fig. 2.4 depicts that the TM doping in  $\text{TiO}_2$  leads to red shift in absorbance spectra implying that absorbance occur to longer wavelength.

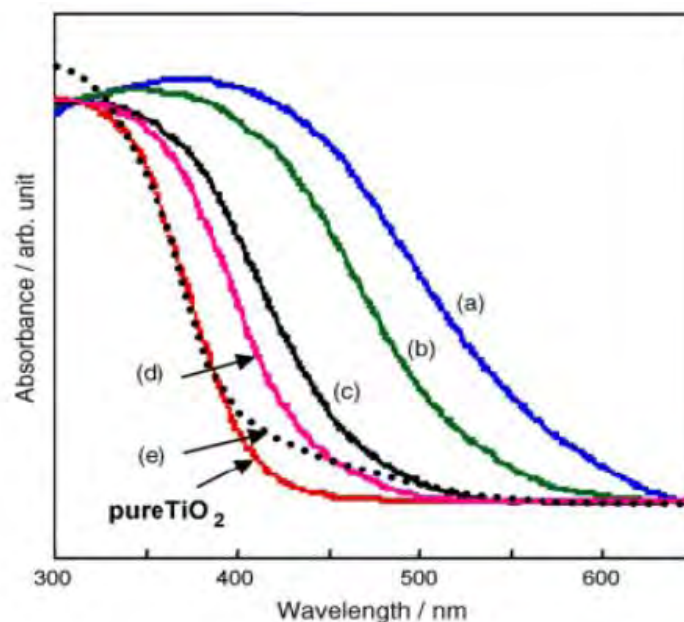


Fig. 2.4. Diffuse reflectance UV-visible spectra of  $\text{TiO}_2$  implanted with (a) V, (b) Cr, (c) Fe, (d) Ni ions<sup>46</sup>

### ***Single nonmetal ions doped $\text{TiO}_2$***

Nonmetal ions were also extensively studied as a means to address the absorption edge towards long wavelength region by substituting oxygen with various kinds of nonmetal ions in  $\text{TiO}_2$  lattice<sup>47</sup>. For nonmetal ions doped  $\text{TiO}_2$ , the p states of dopants were either mixed with O 2p to shift the valence band edge upwards or located above valence band to act as stepping stones to relay electrons from valence band to conduction band, making the absorption edge is shifted into visible region. Among all nonmetal dopants, N<sup>9,48</sup> has been most studied since the first report by Sato in 1986. Fig. 2.5 depicts the effect of N content on the absorbance of  $\text{TiO}_2$ . In addition to this, C<sup>9,49</sup>, S<sup>9,50</sup>, and F<sup>51</sup> were also widely exploited as nonmetal dopants.

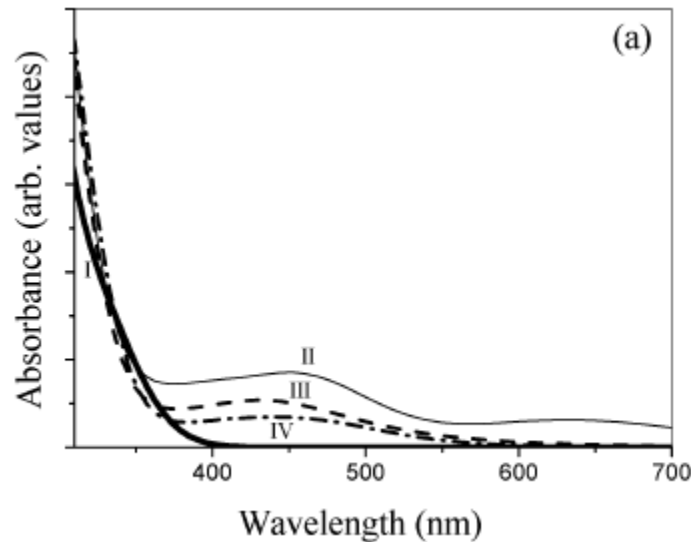


Fig. 2.5. The optical absorption curves calculated for various N concentrations in the polycrystalline TiO<sub>2</sub>: (I) undoped TiO<sub>2</sub>; (II) 12.5 mol.% nitrogen doped; (III) 6.2 mol.% nitrogen doped; and (IV) 3.1 mol.% nitrogen doped.<sup>52</sup>

### ***Problems with ion doping in TiO<sub>2</sub>***

The introduction of substitutional elements creates scattering centers and this can cause a decrease in the photochemical activity. For example, it has been reported that substitutional TM serves as a center for charge carrier recombination<sup>2</sup>. On the other hand, the states introduced by C in forbidden band were too deep to helpfully transfer photo excited carriers from valence band to conduction band, whereas the F 2p states were localized below valence band edge without any gap in forbidden gap or mixing with valence band or conduction band<sup>47</sup>. Nevertheless, some studies proposed distinctive issue that substitutional doping of C in TiO<sub>2</sub> resulted in significant overlap between C states and O 2p states near the top of valence band<sup>53</sup>. Apart from N, S, C and F other nonmetal ions doping into TiO<sub>2</sub> have been exploited likewise but with less extent.

### ***Tuning of optical properties via composite making***

The nanostructured ZnO/ TiO<sub>2</sub> has been found to improve the optical properties, even though, ZnO is a wide band gap semiconductor.<sup>16</sup>

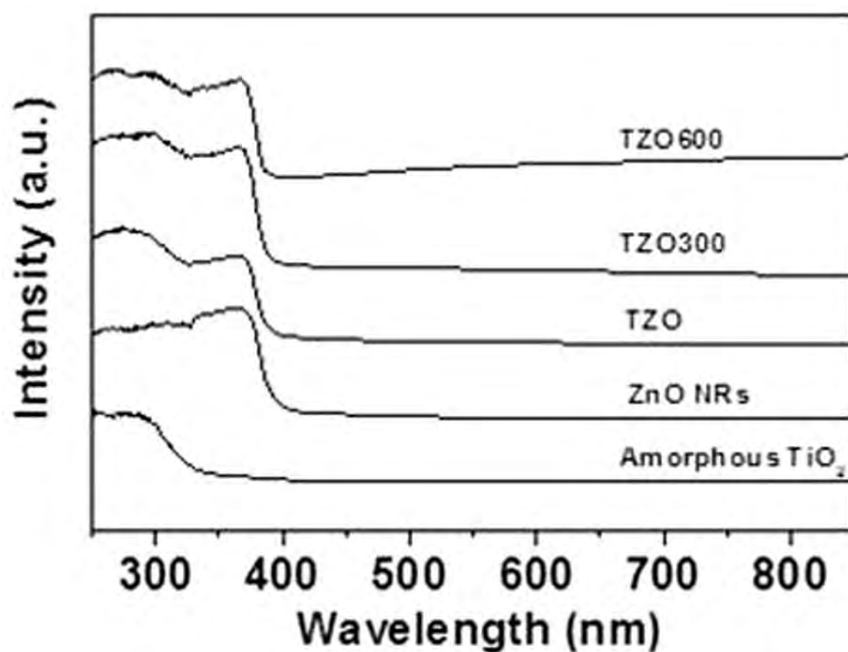


Fig. 2.6. UV-Vis absorption spectra of amorphous  $\text{TiO}_2$  nanoparticles, ZnO nanorods, TZO nano hybrids and the annealed products TZO300 and TZO600.<sup>16</sup>

The UV-Vis absorption spectra of amorphous  $\text{TiO}_2$  nanoparticles, ZnO nanorods,  $\text{TiO}_2$ -ZnO (TZO) nano hybrids and the annealed products at 300 °C (TZO300) and 600 °C (TZO600) are compared in Fig. 2.6. ZnO and all TZOs have strong adsorption in the UV region at the absorption edge of 380 nm, with a corresponding ZnO band gap of 3.26 eV. The amorphous  $\text{TiO}_2$  nanoparticles have a strong adsorption in the deep-UV region at the absorption edge 313 nm. For TZO, a higher absorbance below 320 nm ensures that the  $\text{TiO}_2$  nanoparticles, which are attached to ZnO nanorods, dominate the deep UV absorption. This may enhance the use of UV light compared with pure ZnO nanorods.

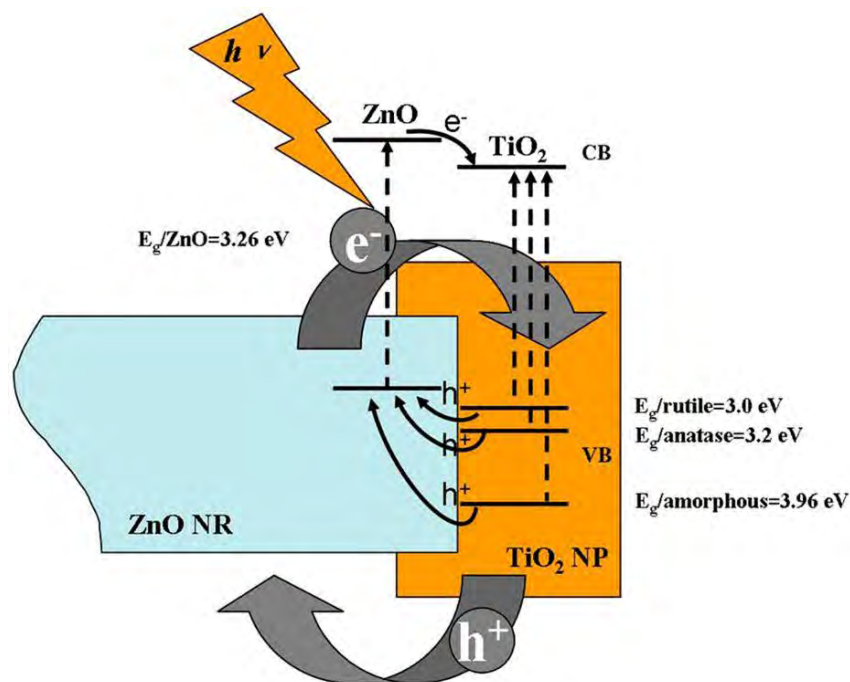


Fig. 2.7. Enhanced photocatalytic performance of TiO<sub>2</sub>-ZnO hybrid nanostructures<sup>16</sup>

The TZO nanohybrids form a type II semiconductor heterostructure as shown in Fig. 2.7. In this case, electrons and holes in semiconductors are at their lowest energy states. Therefore, the energy gradient at the interfaces tends to spatially separate those electrons and holes which are excited by UV light on different sides of the hetero-junction. Under illumination, the electrons are transferred from the conduction band (CB) of ZnO to CB of TiO<sub>2</sub>. In addition, the holes are transferred from the valence band (VB) of TiO<sub>2</sub> to VB of ZnO. This process isolates active electrons and holes and, hence, accelerates the decrease in the electron-hole pair recombination and erodes the increase in lifespan.

Nowadays, the visible light activity of titanium is increased by coupling TiO<sub>2</sub> with other narrow bandgap semiconductors. The proposition shown in Fig. 2.8 is that coupled semiconductors form a hetero-junction structure which can transfer electrons from an excited small band gap semiconductor into another attached one in the case of proper band potentials.

In<sub>2</sub>O<sub>3</sub><sup>17</sup>, BiFeO<sub>3</sub><sup>18</sup> or CdSe co-sensitized TiO<sub>2</sub><sup>19</sup> heterostructures have been reported for showing better visible light activity. Multiferroic BiFeO<sub>3</sub> (BFO) deserves a special mention for its narrow band gap (2.2 eV) and chemical stability which have made it a suitable visible-light responsive photocatalyst.<sup>1</sup>

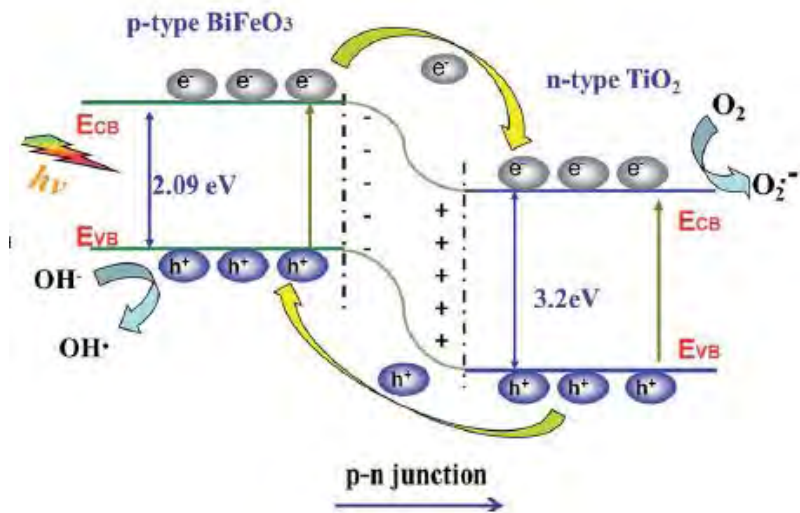


Fig. 2.8. Postulate of the visible light-induced photodegradation mechanism of BiFeO<sub>3</sub>/TiO<sub>2</sub> nanofibers<sup>18</sup>

Fig. 2.9 shows the red shift in absorbance of TiO<sub>2</sub> due to the addition of higher percentage of BiFeO<sub>3</sub>.

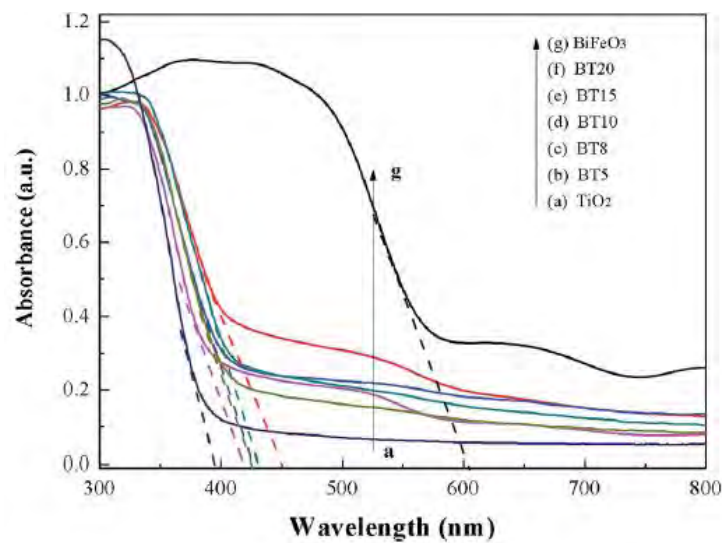


Fig. 2.9. UV-vis spectra of (a) TiO<sub>2</sub>, (b) TiO<sub>2</sub>-5% BiFeO<sub>3</sub>, (c) TiO<sub>2</sub>-8%BiFeO<sub>3</sub>, (d) TiO<sub>2</sub>-10%BiFeO<sub>3</sub>, (e) TiO<sub>2</sub>-15%BiFeO<sub>3</sub>, (f) TiO<sub>2</sub>-20%BiFeO<sub>3</sub> (g) BiFeO<sub>3</sub><sup>18</sup>

The optical band gap of CdSe-TiO<sub>2</sub> composite films<sup>19</sup> shown in Fig. 2.10 was calculated using the Tauc's law<sup>54</sup> as given below:

$$(\alpha h\nu) = A' (E - E_g)^n$$

Where  $A'$  is a constant,  $E$  is the photon energy,  $E_g$  is the band gap energy,  $\alpha$  is absorption coefficient and  $n$  is the power factor of the optical transition mode in a semiconductor, i.e., direct transition ( $n=1/2$ ) or indirect transition ( $n=2$ ). The indirect band gap of CdSe-TiO<sub>2</sub> film had decreased tremendously, however direct band gap had decreased slightly.

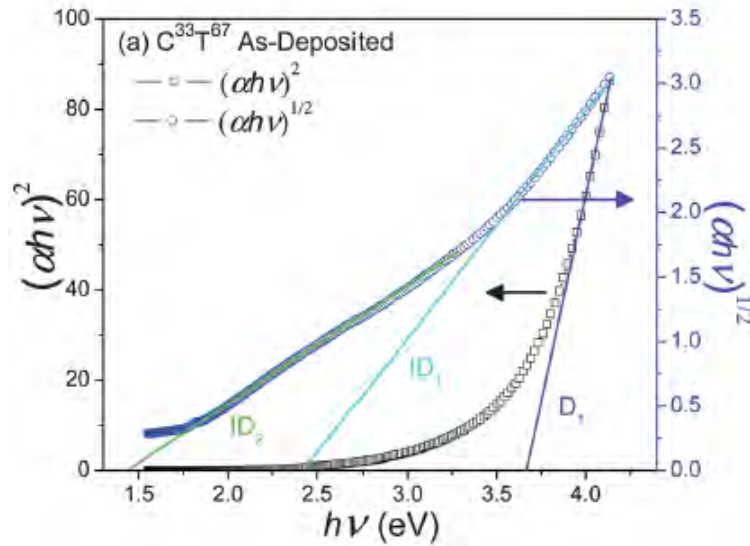


Fig. 2.10. Example Tauc plot extrapolations showing the spectra of the as-deposited C<sup>33</sup>T<sup>67</sup> films. Here C<sup>33</sup>T<sup>67</sup> stands for 33% CdSe and 67% TiO<sub>2</sub>.<sup>19</sup>

## 2.1.3 Magnetism of TiO<sub>2</sub>

### 2.1.3.1 Types of magnetism

In TiO<sub>2</sub>, the overall magnetic property depends on two factors: (i) the magnetic response associated with each atom/ion, and (ii) the interactions between these magnetic moments. In the case that there are no unpaired electrons around each atom/ion, there will be no net magnetic moment associated with them (bearing in mind that both orbital moments and electron spins cancel to zero in a fully filled orbital). This material will show diamagnetic behavior; the orbital and spin magnetic moments will oppose the external magnetic field, just as a conducting loop of wire opposes a changing magnetic flux by inducing its own oppositely oriented magnetic field (Lenz's law). When there are unpaired electrons, every atom/ion has a net magnetic moment. Depending on the interactions between the magnetic dipoles, the material may show

(i) paramagnetism (PM); (ii) ferromagnetism (FM); (iii) antiferromagnetism (AFM) and (iv) ferrimagnetism (FIM). In a paramagnetic material, alignment of adjacent moments is not observed due to thermal fluctuations being stronger than any driving force which might align the moments as shown in Fig. 2.11.

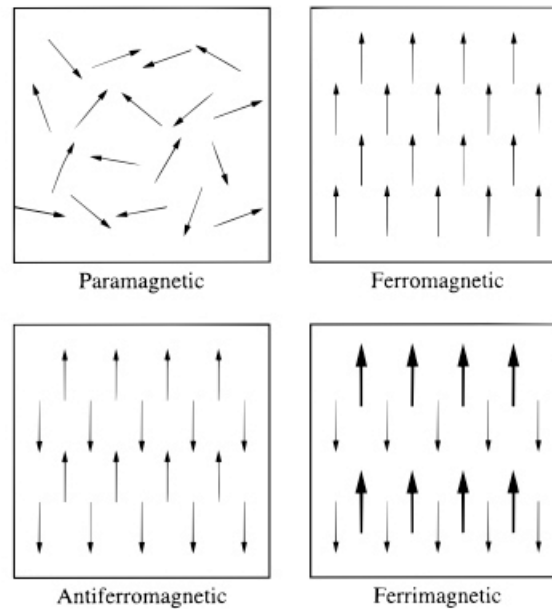


Fig. 2.11. Common examples of magnetic dipole ordering<sup>55</sup>

Ferromagnetism, anti-ferromagnetism and ferrimagnetism are all manifestations of the same quantum mechanical interaction; exchange interaction. This interaction is purely quantum mechanical with no classical analogue. It has connections with Pauli's exclusion principle. Basically, according to Pauli's exclusion principle two electrons cannot occupy the same state without having different spin magnetic moments. An implication of this is, since oppositely aligned spins can occupy the same state they can be much closer to each other on the average. This would increase the coulombic forces between them and thus make the system energy higher. Consequently parallel spins stay further away from each other and their net coulombic energy is lower, which is a very simplified account of the origin of ferromagnetism.

In some cases, the overall energy might be lowered if spins are aligned anti-parallel. Such ordering gives rise to anti-ferromagnetism with a net zero magnetization. Ferrimagnetic order consists of anti-parallel unequal moments, resulting in a non-zero net magnetization.

Ferromagnetism is a very strong magnetic response compared with paramagnetic and diamagnetic behaviors. It is characterized by a transition temperature (Neel temperature,  $T_N$ ). Above this temperature, the material is paramagnetic. Below this temperature, it is ferromagnetic. The magnetic susceptibility,  $\chi = M/H$ , which defines the degree of magnetization of a material in response to a magnetic field, is a good indication of their magnetic properties. If  $\chi$  is positive the material is paramagnetic, and the magnetic field is strengthened by the presence of the material. If  $\chi$  is negative then the material is diamagnetic and the magnetic field is weakened in the presence of the material. The magnetic susceptibility of a ferromagnetic substance is not linear and much larger than unity.

### 2.1.3.2 Tuning of magnetism in $TiO_2$

A more modern theory of magnetism is based on the electron spin principle. From the study of atomic structure it is known that all matter is composed of vast quantities of atoms, each atom containing one or more orbital electrons. The electrons are considered to orbit in various shells and sub shells depending upon their distance from the nucleus. It is believed that the electrons revolve on its axis as it orbits the nucleus of an atom. The effectiveness of the magnetic field of an atom is determined by the number of electrons spinning in each direction. If an atom has equal numbers of electrons spinning in opposite directions, the magnetic fields surrounding the electrons cancel one another, and the atom is unmagnetized. However, if more electrons spin in one direction than another, the atom is magnetized. It has been experimentally proven that an electron has a magnetic field about it along with an electric field.

Electronic structure shown in Fig. 2.12 depicts that titanium with an atomic number of 22, has 22 protons in the nucleus and 22 revolving electrons orbiting its nucleus. In this case 11 electrons are spinning in a clockwise direction and 11 electrons are spinning in a counterclockwise direction, the opposing magnetic fields is neutralized. Thus  $TiO_2$  exhibits diamagnetic behavior. However, it is possible to induce magnetism in  $TiO_2$  by doping, changing the synthesis parameter and coupling with other magnetic materials.



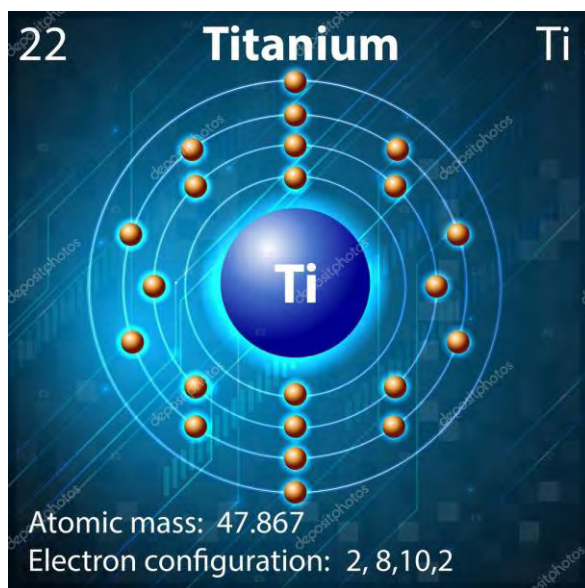


Fig. 2.12. Electronic configuration of Ti atom.

### ***Doping with transition metals (TM)***

The magnetism in  $\text{TiO}_2$  has been tuned by doping with TM metals. Among the TM, metals with unfilled 'd' orbital such as Mn, Fe, Co, Ni etc. (see Table 2.1) are best option for inducing magnetism in  $\text{TiO}_2$ . After the first discovery of room-temperature ferromagnetism in Co-doped anatase  $\text{TiO}_2$  thin films<sup>56</sup>, several researches have been performed on the magnetism of  $\text{TiO}_2$  doped with Mn<sup>8</sup>, V<sup>57</sup>, Cr<sup>58</sup> and Fe<sup>7</sup> etc. Fig. 2.13 depicts that pure  $\text{TiO}_2$  exhibit diamagnetism while Mn doped  $\text{TiO}_2$  exhibit magnetism. Different research groups<sup>57,59</sup> learned about the magnetic properties of TM-doped  $\text{TiO}_2$  samples using the first-principles method, but the origin of ferromagnetism in magnetic-transition-element-doped oxide semiconductors is still under debate as to whether ferromagnetism is intrinsic<sup>58,60</sup> or whether it comes from the precipitation of magnetic clusters.

Table 2.1: Comparison of the electron configurations and unpaired electrons for various ions

Ion	Electron Configuration	Number of Unpaired Electrons	Magnetic moment in Bohr magneton ( $\mu_B$ )
$\text{Sc}^{3+}$	$3p^6$	0	0
$\text{Ti}^{4+}$ ( $\text{Ti}^{3+}$ )	$3p^6(3d^1)$	0(1)	0(1)
$\text{V}^{3+}$ ( $\text{V}^{5+}$ )	$2d^2(3p^6)$	2(0)	2(0)
$\text{Cr}^{3+}$ ( $\text{Cr}^{2+}$ )	$2d^3(3d^4)$	3(4)	3(4)
$\text{Mn}^{2+}$ ( $\text{Mn}^{3+}$ )( $\text{Mn}^{4+}$ )	$2d^5(3d^4)(3d^3)$	5(4)(3)	5(4)(3)
$\text{Fe}^{2+}$	$3d^6$	4	4
$\text{Fe}^{3+}$	$3d^5$	5	5
$\text{Co}^{2+}$ ( $\text{Co}^{3+}$ )	$3d^7(3d^6)$	3(4)	3(4)
$\text{Ni}^{2+}$	$3d^8$	2	2
$\text{Cu}^{2+}$ ( $\text{Cu}^+$ )	$3d^9(3d^{10})$	1(0)	1(0)

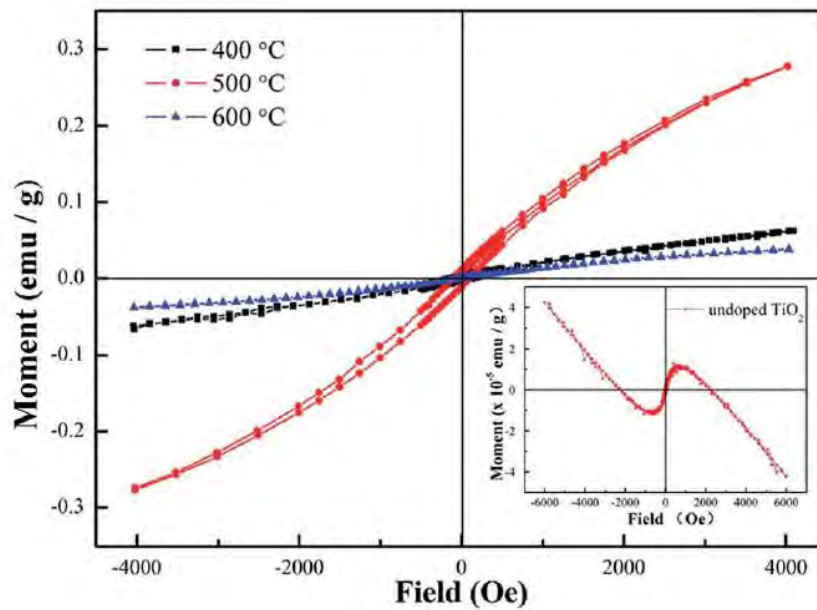


Fig. 2.13. M–H curves of Mn-doped TiO<sub>2</sub> at 400, 500 and 600 °C. The inset shows M–H curve of undoped TiO<sub>2</sub>.<sup>61</sup>

### *Synthesis technique induced magnetism in TiO<sub>2</sub>*

First-principles calculations indicated that the ferromagnetism of undoped rutile TiO<sub>2</sub> largely originates from the d orbitals of low-charge-state Ti ions converted from Ti<sup>4+</sup> ions induced by the surface oxygen vacancies.<sup>62</sup> However, few experimental studies of exploring the origin of room-temperature ferromagnetism in undoped TiO<sub>2</sub> single crystals exist. In these studies, the influence of annealing temperature in a high vacuum on structure and magnetism has been addressed.<sup>63</sup> The presence of a Ti<sup>3+</sup> species is very likely after high-temperature annealing. It is possibly associated with oxygen vacancies due to the removal of O<sub>2</sub> ions from the lattice. When O is removed, the excess electrons are unpaired.<sup>64</sup> They can occupy the nearby localized Ti 3d orbit, and therefore convert Ti<sup>4+</sup> ions to Ti<sup>3+</sup> ions. The unpaired 3d electrons in Ti<sup>3+</sup> ions provide vast spin magnetic moments which are definitely related to the observed ferromagnetism. Fig. 2.14 depicts the effect of annealing time on the magnetization of pure TiO<sub>2</sub> in the presence of oxygen.

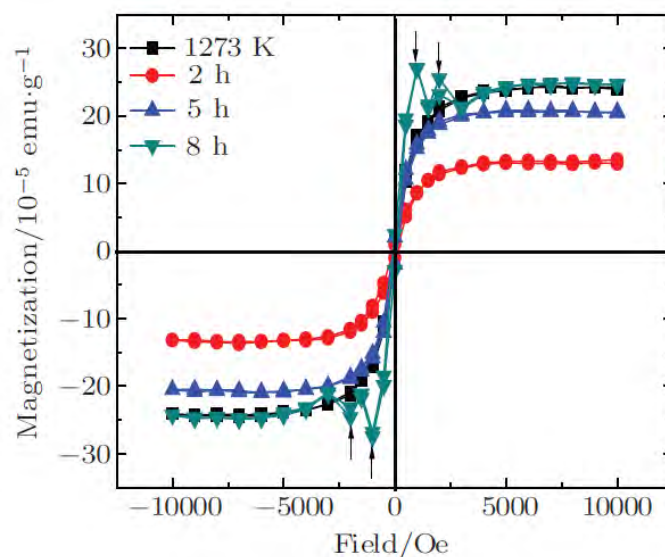


Fig. 2.14. Magnetization versus the magnetic field at 300 K for  $\text{TiO}_2$  single crystals, annealed in  $\text{O}_2$  at 1173 K for 2 h, 5 h, and 8 h. The anomalous protrusions in the curve are described by arrows. Note that the signals of substrates were removed.<sup>63</sup>

### *Tuning magnetism by making composite*

Composite materials exhibit combined properties (also known as product properties) of two different materials. The physical quantities like density, magnetization, and dielectric properties come in category of product properties. Based on this concept  $\text{TiO}_2$  has been coupled with many magnetic properties. For example, magnetic properties have been improved by the fabrication of  $\text{TiO}_2\text{-Fe}_3\text{O}_4\text{-SiO}_2$  or  $\text{Fe}_x\text{O}_y\text{-TiO}_2$  composites.<sup>14,15,65</sup>

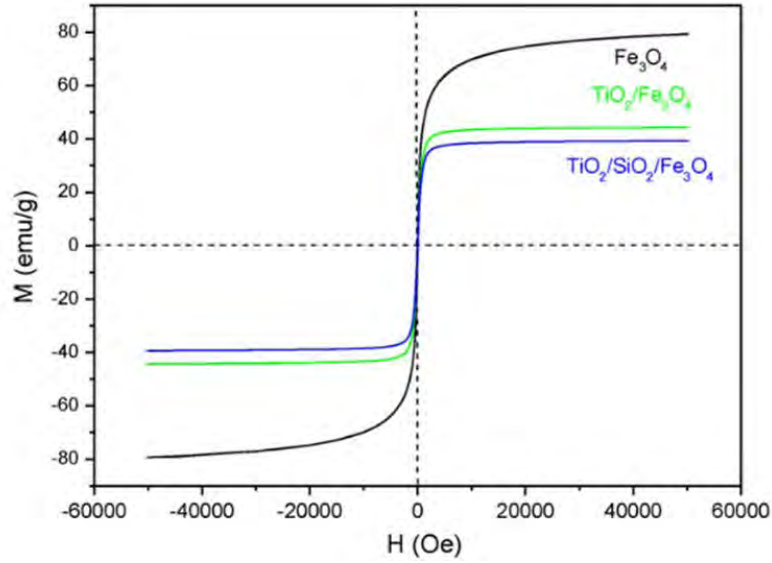
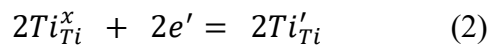
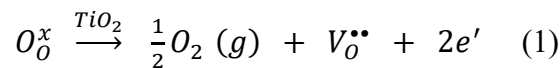


Fig.2.15. Magnetic hysteresis loop at 300K of magnetic iron oxide ( $\text{Fe}_3\text{O}_4$ ),  $\text{TiO}_2/\text{Fe}_3\text{O}_4$  and  $\text{TiO}_2/\text{SiO}_2/\text{Fe}_3\text{O}_4$  nanoparticles<sup>65</sup>

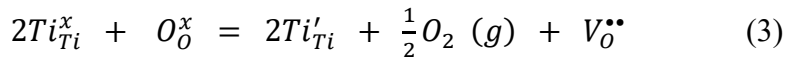
Magnetic properties of seed magnetic iron oxide,  $\text{TiO}_2/\text{Fe}_3\text{O}_4$  and  $\text{TiO}_2/\text{SiO}_2/\text{Fe}_3\text{O}_4$  nanoparticles are measured at 300K as illustrated in Fig.2.15. The observed value of saturation magnetization for the magnetic iron oxide particles used as seed was found to be lower than that of bulk magnetite (92 emu/g). The decrease in the saturation magnetization with the coating processes is due to the lower content of magnetic iron oxide in the photocatalysts and the presence of non-magnetic coating layers ( $\text{TiO}_2$  and  $\text{SiO}_2$ ).

#### 2.1.4 Electrical properties of $\text{TiO}_2$

$\text{TiO}_2$  is a n-type semiconductor even though its band gap energy is between 3 to 3.2 eV. The formation of the oxygen vacancies (OVs) and titanium interstitials are responsible for this sort of conductivity.<sup>66</sup>  $\text{TiO}_2$  is a sub-stoichiometric compound with excess titanium under standard conditions. This sub-stoichiometry is accommodated by forming OVs or titanium interstitials. The following reaction mechanisms can be considered for the formation of OVs in  $\text{TiO}_2$  crystal<sup>67</sup>:



Combining equations (1) and (2)



As follows the n-type conductivity behavior found in TiO<sub>2</sub> implies equation (3) to be the dominant step for providing two excess electrons. The carrier concentration of TiO<sub>2</sub> found in the literatures ranges from  $1 \times 10^{16} \text{ cm}^{-3}$  to  $1 \times 10^{20} \text{ cm}^{-3}$ .<sup>68,69</sup> The resistivity of conductor and semiconductor normally varies from  $10^{-3}$  to  $10^8 \Omega\text{-cm}$ .<sup>70</sup> However, the conductivity, resistivity and concentration of this pure TiO<sub>2</sub> film depends on the synthesis technique and doping elements.

#### 2.1.4.1 Engineering of electrical properties in TiO<sub>2</sub>

The elements with unpaired electron in d orbital are suitable for changing the electrical nature of TiO<sub>2</sub>. Moreover it is possible to change the stoichiometry of oxygen in TiO<sub>2</sub> by controlling the synthesis atmosphere.

##### *Doping elements to modify the electrical properties*

p-type carriers have been found in Fe, Mn, and Cr-doped TiO<sub>2</sub> films<sup>7,71</sup> suggesting the importance of the holes in the observed ferromagnetism. It may appear surprising that Mn-doped TiO<sub>2</sub> conducts via holes instead of electrons considering the existence of oxygen vacancies that favor n-type conduction. In Mn-doped TiO<sub>2</sub>, Mn occupied the Ti antisite and formed an acceptor complex under O-rich condition. The complex has a shallow acceptor level, can effectively compensate native donor defects, such as O vacancies and Ti interstitials, and is responsible for p-type conductivity of the Mn-doped TiO<sub>2</sub>.

##### *Synthesis technique to control the electrical properties*

The conductivity nature and mobility of TiO<sub>2</sub> changes depending on the synthesis technique. Normally under oxygen atmosphere condition, intrinsic TiO<sub>2</sub> behaves as p-type semiconductor. On the other hand, oxygen defects may originate from the processing of TiO<sub>2- $\delta$</sub>  films in an oxygen-deficient atmosphere.<sup>72</sup> It is established that plasma layer deposition leads to form oxygen deficient anatase TiO<sub>2- $\delta$</sub>  films which produces n type conductivity.<sup>72</sup>

## 2.1.5 Application of TiO<sub>2</sub>

### 2.1.5.1 Visible light photocatalysis of TiO<sub>2</sub> on organic compounds

Photocatalysis is defined as capture of the sun light or any incident light to turn organic matter to carbon dioxide and water by the presence of a semiconductor photocatalyst. To better understand the mechanism of photocatalysis, oxidative and reductive reaction procedures of TiO<sub>2</sub> are depicted in Fig. 2.16, in which the energy band diagram of TiO<sub>2</sub> in pH 7 solution is proposed by Fujishima<sup>73</sup>, together with redox potential of various radicals and molecules versus standard hydrogen electrode (SHE).

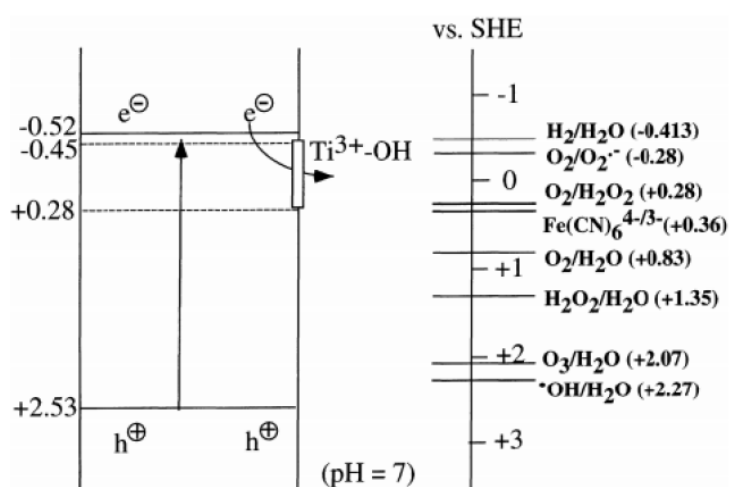
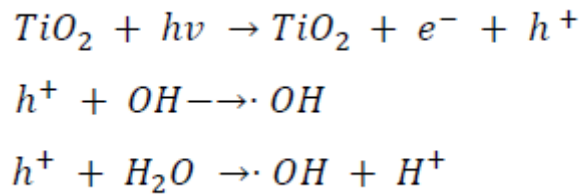


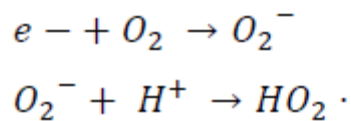
Fig. 2.16. Schematic diagram of photocatalysis process of TiO<sub>2</sub><sup>73</sup>.

The photocatalytic mechanism starts from the absorption of photons with energy equal to or greater than the band gap value of TiO<sub>2</sub>. Then electrons in valence band would be ejected into conduction band leaving an equal amount of positive holes in valence band. When TiO<sub>2</sub> is in contact with electrolyte solution, the thermodynamic equilibrium of Fermi level occurs at the interface. This would result in the formation of space charge region, normally of the order of 1-3 nm, in which the energy level is bent upwards or downwards. In this space charge region, photogenerated electrons and holes are separated and moved in a different way on account of band bending. Therefore, upon the absorption of photons, electron and hole pairs are generated in TiO<sub>2</sub> and one portion diffuses to the surface of the photocatalyst taking part in the chemical reaction with adsorbed molecules on the surface of TiO<sub>2</sub><sup>74</sup>. The oxidative potential of photogenerated hole is as high as 2.53 V, which is positive enough to not only oxidize some

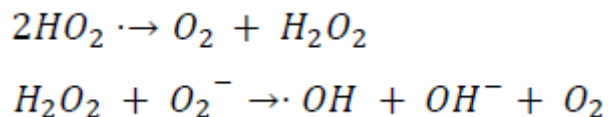
organic and inorganic matters straightly but also react with water and hydroxyl ion to generate highly oxidative compound ( $\cdot\text{OH}$ ).



On the other hand, the reducing potential for photogenerated electrons is as negative as -0.52 V, which is in principle enough to extract H from water to decompose water into  $\text{H}_2$  and  $\text{O}_2$ .<sup>73</sup> Once it diffuses to the surface of  $\text{TiO}_2$ , electrons can reduce the adsorbed oxygen to form charged super oxide anion. In high pH solution, the charged super oxide anion desorbs and can directly oxidize adjacent organic molecules. In low pH solution, the charged super oxide anion reacts with  $\text{H}^+$  to form a perhydroxyl radical  $\text{HO}_2\cdot$ , which is an oxidative agent to be able to decompose hydrocarbons.



It was also advocated that the formed perhydroxyl could directly react with absorbance or react with super oxide anion again to produce oxidative compound ( $\cdot\text{OH}$ ) or be further decomposed to oxygen and oxidative oxygen<sup>75</sup>.



Apparently, photogenerated electrons and holes are consumed through oxidation and reduction process thus the total reaction cycle is completed, resulting in the back of  $\text{TiO}_2$  to original state. At the same time, organic molecules absorbed on the surface of  $\text{TiO}_2$  have been decomposed relying on the above described process. Then another excitation happens again until organic molecules are decomposed completely into  $\text{CO}_2$  and  $\text{H}_2\text{O}$ . From Fig. 2.16, one can see that the



oxidative potential of the formed oxidative hydroxyl radical (OH) is extremely high as 2.27 V, much higher than most of oxidants such as  $O_3$ ,  $H_2O_2$ , and thus can decompose most of organic compounds completely into  $CO_2$  and  $H_2O$ <sup>76</sup>.

In effect, apart from  $TiO_2$ , a variety of semiconductor materials have been identified and studied experimentally; including  $ZnO$ ,  $CdS$ ,  $SnO_2$ ,  $WO_3$ ,  $CuO$ ,  $Fe_2O_3$  and so on. However compared to these semiconductor materials,  $TiO_2$  has incontrovertibly been the most studied photocatalyst partly, on account of it being extremely stable in the presence of aqueous solution, while other types of semiconductor could be easily dissolved in acidic or alkaline solution. What is more,  $TiO_2$  also has sufficient positive valence band edge making photogenerated positive holes can react with water and organic molecules adsorbed on semiconductor surface. As mentioned previously, in most case the photogenerated carriers recombine quickly, but in  $TiO_2$  the recombination is much slower than that of the most semiconductors. The main drawback of  $TiO_2$  is the wide band gap meaning  $TiO_2$  can only absorb the light with wavelength shorter than 380 nm, in other words, only UV part that possesses 5% of the whole energy of the sun can be used by pure  $TiO_2$ , though the absorption coefficient of  $TiO_2$  in this region is in the order of  $10^5\text{ cm}^{-1}$ .

### ***Photocatalytic activity of doped $TiO_2$ with visible light absorption***

As it was mentioned above, the band gap of  $TiO_2$  can be tuned through suitable doping to shift valence band up or conduction band down; or introduce intermediate states for effective absorption under visible light illumination. Nevertheless, photocatalytic activities, of some doped catalysts, were hardly improved despite red shift of optical absorption edges was indeed observed. The photocatalytic activity of  $TiO_2$  materials is largely affected by the following factors. The first critical factor is the light absorption properties of  $TiO_2$  materials, including absorption region and absorption coefficient, which decide the maximum amount of photons that can be converted into electrons and holes from incident light. Large absorption region and coefficient leads to more excitation of carriers. Conceivably, the doping not only narrows the electronic band gap but simultaneously alters the oxidative and redox potential of photogenerated carriers, leading to contradictory influence on photocatalytic activity. Another factor is the surface area of  $TiO_2$  photocatalyst, the larger surface area means more molecules can adsorb onto  $TiO_2$  leading to faster photocatalytic rates. In addition, the electron and hole recombination rate, normally determined by defect levels, is also central to the photocatalytic

activity. The interface is generally a defective site for carriers to recombine, as the lifespan of photogenerated carriers are approximately 10 ns.

One can improve the crystalline degree of TiO<sub>2</sub> photocatalyst to avoid defects. However, this in turn may cause undesirable aggregation of TiO<sub>2</sub> nanomaterials and decrease the relative surface area. In doped TiO<sub>2</sub>, high doping level could induce electronic defect states, crystal defects or even ions oxides separated out from TiO<sub>2</sub> crystal, to act as carrier recombination centres, whereas low doping level could act as charge transfer mediator to prolong lifespan, when carriers migrated from the inside of the photocatalyst to the surface<sup>77</sup>.

Therefore, the relationship between the photocatalytic activity of doped TiO<sub>2</sub> and the physical properties is complicated. Optimum conditions for a specific case should be pursued by taking all of these factors into consideration and may be disparate from one case to another. Generally, in ideally doped TiO<sub>2</sub> materials for visible light photocatalysis, the doping should avoid deep isolated states in forbidden band together with extending absorption region, to maintain or prolong carrier diffusion length before they are recombined, and thus offer good photocatalytic activity under visible light illumination<sup>78</sup>.

Choi et al<sup>79</sup> have systematically studied doping effects of 21 transition metal ions on the photocatalytic activity of TiO<sub>2</sub> prepared from the controlled hydrolysis of titanium tetraisopropoxide. According to their work, the presence of metal ion dopants in TiO<sub>2</sub> matrix significantly influenced its photocatalytic activity in the degradation of CHCl<sub>3</sub>. Doping TiO<sub>2</sub> with suitable ions such as Fe, V, Mo, Ru, Os, Re, and Rh at optimum concentration of 0.1-0.5 at% effectively improved the photo reactivity for both oxidation and reduction. In contrary, doping TiO<sub>2</sub> with Co and Al decreased the photocatalytic activity. It was deduced that the photocatalytic activity was predominantly dependent on the distribution of dopants within TiO<sub>2</sub> particles together with the electronic band structures of doped TiO<sub>2</sub>, which determined the role of dopants states, including mixing with intrinsic energy band, shallow acceptor/donor states for effective trap, or deep isolated states leading recombination.

Teoh and co-workers<sup>80</sup> investigated the photocatalytic activity of Fe doped TiO<sub>2</sub> that prepared via flame paralysis technique, by dissociating oxalic acid under visible light with wavelength longer than 400 nm. Although the increasing of Fe doping level resulted in gradually extended absorption region, the optimum ratio of Fe/Ti for visible light photocatalytic activity was 0.05,

as a balance existed between charge excitation and charge recombination. With respect to the same ion doping, the optimum conditions of doped TiO<sub>2</sub> for the application in visible light photocatalysis were mainly determined by synthesis methods and varied from case to case. As an example, Li et al.<sup>77</sup> similarly synthesized Fe doped TiO<sub>2</sub> particles by a hydrothermal process with conceivable red shift of absorption edge. The photocatalytic activities of doped TiO<sub>2</sub> particles were even worse compared to that of pure TiO<sub>2</sub> particle upon the degradation of methylene blue (MB) under a 300 W highly pressure mercury vapor lamp.

### 2.1.5.2 TiO<sub>2</sub> in spintronics

There is currently a lot of interest in the science and potential technological applications of spin electronics, in which the spin of the charge carriers (electrons or holes) is exploited to provide additional functionalities for microelectronic devices. Dilute magnetic semiconductors (DMSs) are, therefore, extensively studied as potential spintronic materials and expected to play an important role for devices and circuits such spin transistors and ultradense nonvolatile semiconductor memories.<sup>81</sup> For practical application, it is essential that DMS systems display ferromagnetism above room temperature. Most of the initial work in the DMS was focused on TM doped III-V semiconductors, such as Mn-doped GaAs; however, Curie temperature ( $T_c$ ) is much below room temperature. As a wide-band-gap semiconductor, TiO<sub>2</sub> is of interest for photonic, electronic, and magnetic applications.

Recently, oxide DMS systems have shown ferromagnetism above RT. One promising oxide is Ti<sub>1-x</sub>M<sub>x</sub>O<sub>2</sub> (M = magnetic dopant)<sup>56</sup>. However, evidence shows that in the anatase Co:TiO<sub>2-δ</sub> system, clustering of cobalt atoms occurs above a certain doping level (2–3%), and it is believed that the observed high-temperature ferromagnetism in such samples is manifested in these clusters.<sup>82</sup> Under specific growth and annealing conditions, samples without any obvious clusters have also been shown to exhibit ferromagnetism with a  $T_c$  close to 700 K.

## 2.1.6 Processing of TiO<sub>2</sub> film

### 2.1.6.1 Spray pyrolysis deposition technique

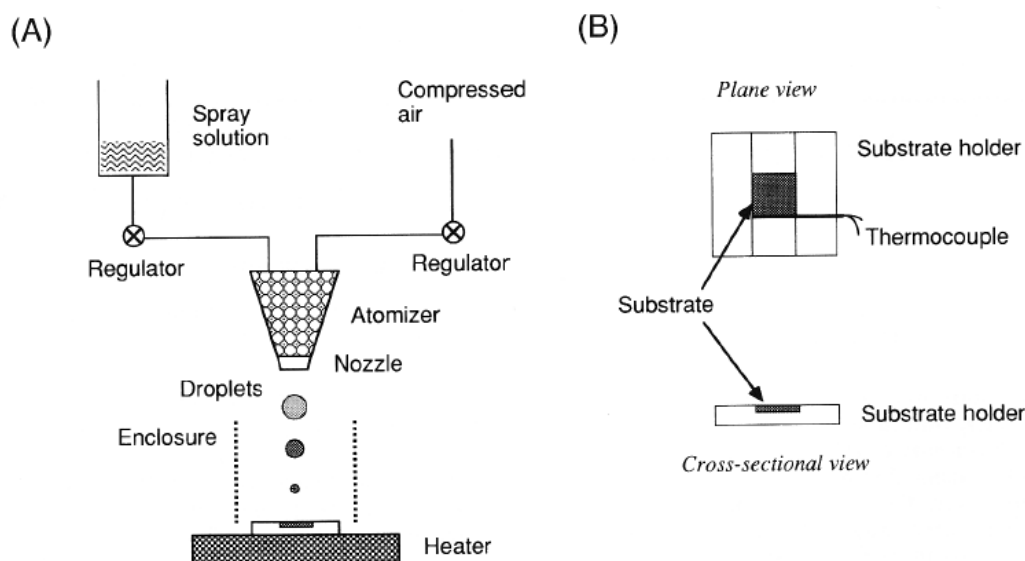


Fig. 2.17. (A) spray pyrolysis apparatus used and (B) substrate and holder

The spray pyrolysis deposition (SPD) technique is one of the most promising ones, since the structure of the apparatus shown in Fig. 2.17 is quite simple and the technique is applicable to produce thin films on a large scale.

Two kinds of starting solutions; TiCl<sub>4</sub> ethanol solution and Ti(i-OC<sub>3</sub>H<sub>7</sub>)<sub>4</sub> 2-propanol solution with TiCl<sub>4</sub> as an additive are prepared generally.<sup>83</sup> The apparatus used for the spray pyrolysis is described elsewhere.<sup>84</sup> For ethanol solution containing the starting compound is atomized by a pneumatic spraying system at an air pressure of 1.0 kg/cm<sup>2</sup>. The droplets are transported by the spraying air onto a heated glass substrate. The substrate is mounted on a cordierite ceramic holder (Fig. 2.17 B), and a thermocouple is set beside the substrate. The substrate temperature is corrected by the deviation in temperature between the center of the surface and the side of the substrate.

After setting up the spray gun approximately 30 cm above the glass substrate (25 x 25x 1mm<sup>3</sup> in size; Corning 7059) on the holder, the substrate is heated up between 300 and 450 °C, and then the pyrolysis procedure is initiated using 2.3 kg/cm<sup>2</sup> of compressed air or pure oxygen gas as a carrier gas.

Since the sprayed mist cooled down the substrate, the period and the volume of the solution for each spraying is fixed at 1.0 s and 1.0 ml, respectively. After recovering the substrate temperature, the same pyrolysis procedure is carried out again. Each procedure is then repeated several times for one substrate.

#### **2.1.6.2 Pulse laser deposition technique**

In pulsed-laser deposition (PLD) a laser beam is used to ablate material from a solid target. The experimental arrangement, which is very simple, is shown in Fig. 2.18. However, the laser–target interactions are very complex and result in the formation of a plume of material (often visible and brightly colored) that contains all the necessary components (often in the correct proportions) for film growth. Excimer lasers operating in the UV are the laser of choice for most PLD systems. Pulse energies up to 500 mJ are used with repetition rates up to several hundred hertz.

In PLD technique the stoichiometric transfer, the pulsed nature of high energy laser makes it possible to utilize laser to precisely deposit almost any type of solid state materials via changing the laser conditions for distinct materials<sup>85</sup>. Moreover, it becomes possible to produce complex composite film of controlled composition gradients, alloys or super lattices and polymer-metal system, by using compound target. There has been tremendous success in synthesis of complex oxide materials with extremely high purity compared with chemical methods. Therefore, ions doped TiO<sub>2</sub> thin films are expected to be successfully fabricated by PLD by employing compound targets under specific conditions.

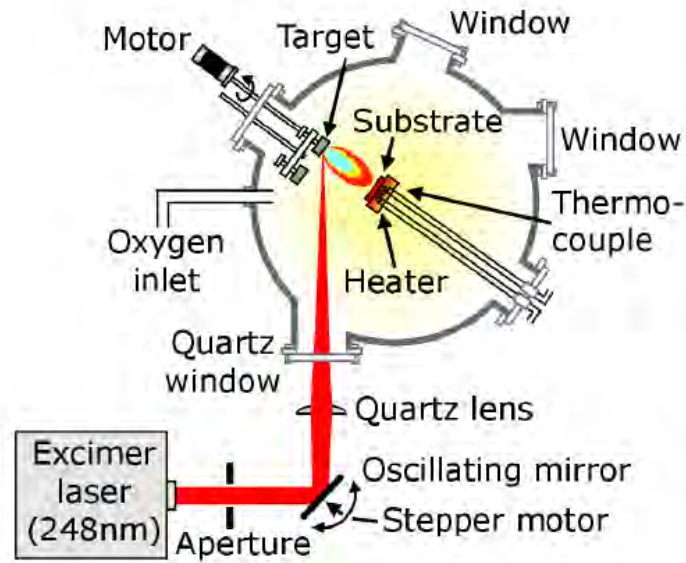


Fig. 2.18. Illustration of pulsed laser deposition process.

### 2.1.6.3 Spin coating method

The development of  $\text{TiO}_2$  thin films is of particular interest because of the numerous technological applications of this inorganic oxide. Using molecular precursors to obtain an oxide network via inorganic polymerization reactions, the sol-gel process provides new approaches and a better control in the preparation of materials compared with solid state reactions.<sup>86</sup> New morphologies can be obtained and new physical properties may be expected depending on the structure which are not produced by the usual processes.<sup>87</sup> This simple method has also the advantage to produce particles in a relatively shorter processing time at lower temperatures. The rheological properties of sols and gels can give rise to the formation of fibers and films shown in Fig. 2.19 and thus considerably increase the anisotropy of the material and its chemical reactivity.

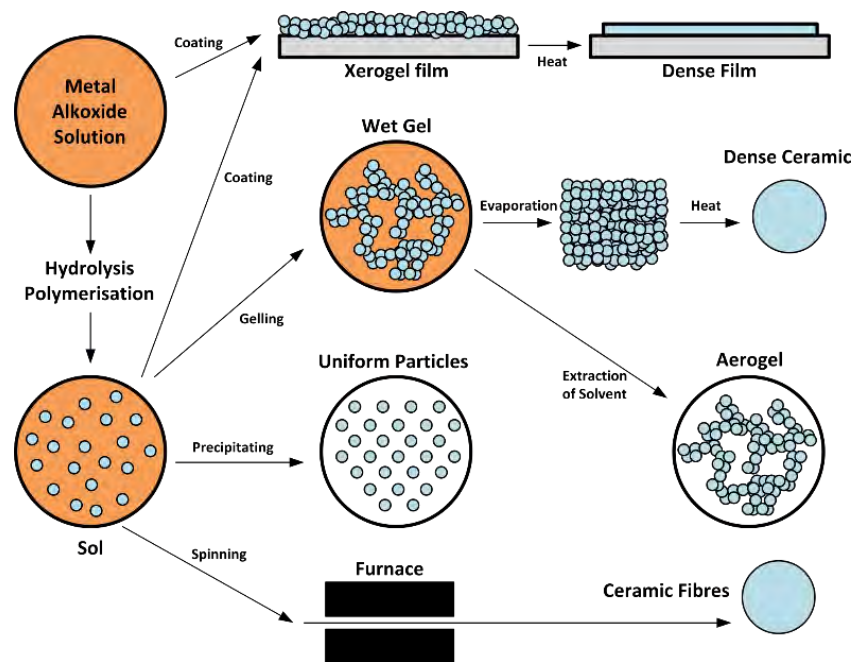
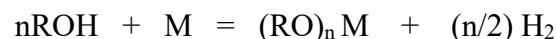


Fig. 2.19. Simplified chart of sol-gel technologies and their application.

### *Aqueous sol-gel technique*

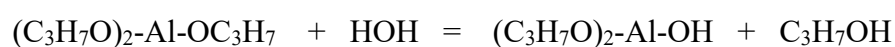
In most sol-gel processes the reactants are solutions of metal alkoxy compounds. Alkoxides result from the reaction of metals (M) with alcohols. The general reaction is:



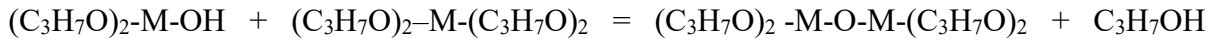
where R is an organic group. For ethanol, R is the ethoxy group  $\text{C}_2\text{H}_5$ . Catalysts are often necessary to increase reaction rates.

To make metal oxide powders from organometallic precursors it is necessary to start with a solution (“sol”) of the metal alkoxy in alcohol. The alcohol is usually the same one that was used for alkoxy formation. Water is added to the alcohol solution. Two reactions then occur, which, using aluminum isopropoxide as an example, may be written as follows

Reaction 1: Hydrolysis



Reaction 2: Condensation

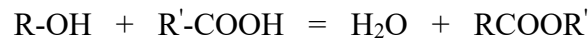


The remaining alkoxy groups (–OR) of the condensation product can be hydrolyzed further to form a crosslinked, three-dimensional network of metal–oxygen bonds.

The available alkoxides for TiO<sub>2</sub> thin film are tetraisopropoxides of titanium<sup>88</sup>, titanium (IV)-n butoxide<sup>89</sup> etc. Moreover solvents used in TiO<sub>2</sub> preparations are ethanol, butanol and water etc. The prepared solgel solution is spin coated on various substrate. Then the film is dried and annealed at specific temperature.

### *Non-aqueous sol-gel technique*

It is a common practice to introduce water in the solution to initiate hydrolysis.<sup>90</sup> In particular case, using water induces the immediate formation of a white precipitate due to the high reactivity of the alcoxide. As it is of technical importance to obtain precursor solutions with long-term stability, water is replaced by acetic acid to decrease the kinetics of the hydrolysis and polycondensation of Ti(O-nBu)<sub>4</sub>. As titanium alkoxide is among the most reactive, the speed of hydrolysis and condensation is very high, therefore, it is difficult to form a stable sol. Acetylacetone (acac) is added as a chelating agent to decrease the reactivity and stabilize the sol. Then, acetic acid is slowly added to the alkoxide solution with constant stirring. Acetic acid allows to initiate hydrolysis via an esterification reaction as follows:



Moreover, it has been shown that acetic acid induces the modification of the molecular structure of the precursor.<sup>91</sup> Here, steric hindrance is then reduced and titanium (IV) reactivity is enhanced. A colorless sol was obtained and at a concentration higher than 2.4 M, it transforms into gel after 6 weeks. Since preparation of thin films by dip-coating requires a weak concentration of sol (~0.5 M), another complexing agent must be added.

The molar ratios of  $\frac{n_{acetic}}{n_{Ti}}$  and  $\frac{n_{acac}}{n_{Ti}}$  were optimized to obtain stable sols of various concentrations between 0.1 M and 0.5 M. The sols viscosities, measured at 25<sup>0</sup> C, are equal to 3.20 cSt for 0.1 M and 3.66 cSt for 0.5 M. TiO<sub>2</sub> precursor solutions are prepared first by stabilizing titanium n-butoxide, dissolved in n-butanol, with acetylacetone, stirring for 30 min. Acetic acid is then added to initialize hydrolysis by esterification reaction with n-butanol. The



final mixture is stirred for 30 min at room temperature. The pH of the sols was less or equal to 2 and the sols are stable for more than two months at various concentrations (0.1 M–0.5 M). Xerogels are obtained after calcination at 100° C for 24 h.

## 2.2 Bismuth Ferrite (BiFeO<sub>3</sub>)

Bismuth ferrite (BiFeO<sub>3</sub>), a prototypical multiferroic, is the most intensely studied multiferroic material in recent years because it exhibits electric and magnetic ordering up to significantly high temperatures. Its ferroelectric transition point or Curie temperature is ~1103 K, and its antiferromagnetic Neel temperature is ~640 K.<sup>23</sup> Its structure has been described as a rhombohedrally distorted perovskite structure belonging to the space group R3c<sup>23</sup>. If imagined as an ideal perovskite unit cell the Bi<sup>3+</sup> atoms take the corner positions, while the O<sup>2-</sup> ions make up the octahedral cage inside of which sits the Fe<sup>3+</sup> ion. The rhombohedral distortion amounts to rotating the oxygen octahedron along the pseudo-cubic [111] direction shown in Fig. 2.20, with adjacent octahedron having a rotation of the opposite sense, and off centering of the Fe<sup>3+</sup> ions resulting in a non-centrosymmetric structure essential for ferroelectricity.

The magnetic structure is of the G-type antiferromagnetic type<sup>23</sup>. It means that, each Fe<sup>3+</sup> ion is surrounded by six other Fe<sup>3+</sup> ions of the opposite spin. The spins aren't exactly anti-parallel; the small canting of the spins would have given rise to weak ferromagnetism, but the presence of a spin cycloid masks such a possibility. The cycloid consists of Fe<sup>3+</sup> ion spins being rotated slightly in going from one ion to the next along the [110]<sub>h</sub> direction completing a full period after 64 nm, thus making the cycloid incommensurate with the crystal lattice<sup>23</sup>.

But there are some problems associated with BiFeO<sub>3</sub>. Its antiferromagnetic nature substantially decreases its utility. For most of the devices envisioned using multiferroics, some ferromagnetism is necessary. Bulk BFO suffers from a high leakage current, thought to be the result of vacancies invariably produced due to the volatility of Bi<sub>2</sub>O<sub>3</sub>. High leakage current translates into loss of stored charged. Phase instability is encountered in solid-state synthesis. Impurity phases lead to deteriorated electric and magnetic properties.

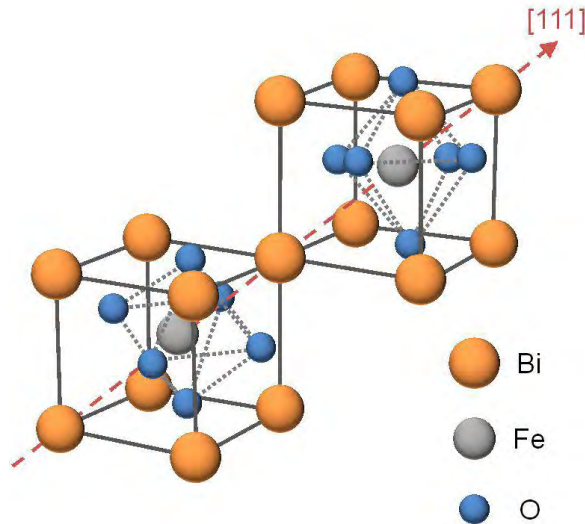


Fig. 2.20. Schematic view of the R3c structure built up from two cubic perovskite BFO unit cells. The cations are displaced along the [111] direction relative to the anions, and the oxygen octahedra rotate with alternating sense around the [111] axis. In the ideal cubic perovskite structure the oxygen ions would occupy the face-centered sites.

Recent works have focused on overcoming these problems by various ways such as:

- Doping rare earth lanthanide ions ( $\text{La}^{3+}$ ,  $\text{Nd}^{3+}$ ,  $\text{Ho}^{3+}$  or  $\text{Sm}^{3+}$ ) or divalent ions ( $\text{Ca}^{2+}$ ,  $\text{Sr}^{2+}$ ,  $\text{Ba}^{2+}$ ,  $\text{Pb}^{2+}$ ) at the A site of BFO for substituting part of  $\text{Bi}^{3+}$  or with ions of  $\text{Nb}^{5+}$ ,  $\text{Mn}^{4+}$ ,  $\text{Cr}^{3+}$ ,  $\text{Ti}^{4+}$  at the B site for substituting part of  $\text{Fe}^{3+}$ .<sup>92,93 94</sup>
- Fabricating a solid solution of BFO with other  $\text{ABO}_3$  perovskite materials, such as  $\text{BaTiO}_3$ .
- Synthesizing BFO nano particles with grain size below 64 nm to achieve ferromagnetism by destroying spiral spin structure.<sup>23</sup>
- Depositing ultra-thin BFO single layer or multilayer films to enhance ferroelectric property.<sup>95</sup>
- Fabricating high quality single crystal of BFO to solve non-stoichiometric problems<sup>96</sup>

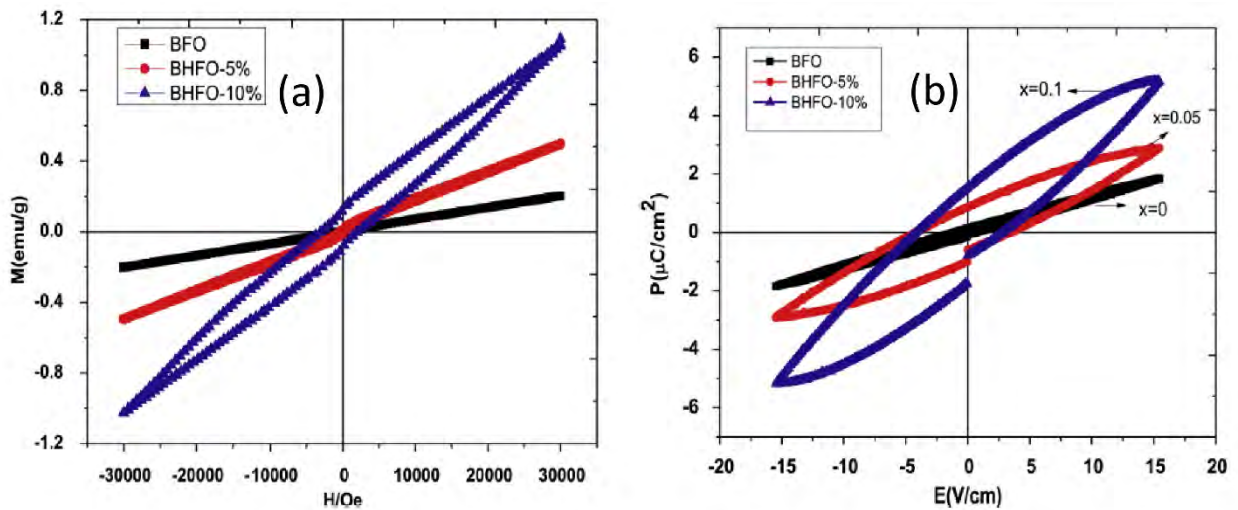


Fig. 2.21. (a) Magnetization versus magnetic field curves and (b) Electric field dependence of polarization (P–E) hysteresis loops for  $\text{Bi}_{1-x}\text{Ho}_x\text{FeO}_3$  samples where  $x=0.0, 0.05, 0.1$ .

Among these approaches, it has been proved doping with tri-positive rare-earth ions ( $\text{R}^{3+}$ ) at the Bi site has been proposed to mitigate some of the issues mentioned above.<sup>25</sup> Previous reports suggest that 10 mol.% Holmium ( $\text{Ho}^{3+}$ ) doping at Bi site increases the magnetization by 6 times compared to pure BFO as can be seen from Fig. 2.21 (a).<sup>25</sup> Indeed, hysteresis loop of 10 mol.%  $\text{Ho}^{3+}$  doped BFO is wider than that of pure BFO and 5 mol.%  $\text{Ho}^{3+}$  doped BFO implying that 10 mol.%  $\text{Ho}^{3+}$  doped BFO has hard magnetism. Besides, the substitution of  $\text{Ho}^{3+}$  ions for  $\text{Bi}^{3+}$  ions can decrease the oxygen vacancy density and minimize the oxygen vacancy effects on ferroelectricity shown in Fig 2.21 (b).<sup>25</sup> This phenomenon ultimately lowers the leakage current of  $\text{Bi}_{1-x}\text{Ho}_x\text{FeO}_3$  ( $x=0.05, 0.1$ ) by two orders of magnitude compared to that of BFO. Among them 10 mol.%  $\text{Ho}^{3+}$  doped BFO exhibits higher resistivity than the pure one.<sup>25</sup> Moreover,  $\text{Ho}^{3+}$  is a rare earth metal it is expected that 10 mol.%  $\text{Ho}^{3+}$  doped BFO ( $\text{Bi}_{0.9}\text{Ho}_{0.1}\text{FeO}_3$ ) nanoparticles will have better absorbance in the visible region and lower band gap than BFO.<sup>23</sup>

### 2.2.1 Crystal structure of BiFeO<sub>3</sub>

The room-temperature phase of BFO is classed as rhombohedral (point group R3c)<sup>23</sup>. The perovskite-type unit cell has a lattice parameter,  $a_{pc}$ , of 3.965 Å and a rhombohedral angle,  $\alpha_{pc}$ , of 89.3–89° at room temperature<sup>97</sup> with ferroelectric polarization along  $[111]_{\text{pseudocubic}}$ .<sup>98</sup>

A very important structural parameter is the rotation angle of the oxygen octahedra. This angle would be 0° for a cubic perovskite with perfectly matched ionic sizes. A measure of how well the ions fit into a perovskite unit cell is the ratio  $(r_{\text{Bi}} + r_{\text{O}})/l$ , where  $r$  is the ionic radius of the respective ion and  $l$  is the length of the octahedral edge. This is completely analogous to the commonly used Goldschmidt tolerance factor,<sup>97</sup> which is defined as  $t = (r_{\text{Bi}} + r_{\text{O}})/(r_{\text{Fe}} + r_{\text{O}})$ . For BiFeO<sub>3</sub> we obtain  $t=0.88$  using the ionic radii of Shannon,<sup>99</sup> with Bi<sup>3+</sup> in eightfold coordination (the value for 12-fold coordination is not reported) and Fe<sup>3+</sup> in sixfold coordination and high spin. When this ratio is smaller than one, the oxygen octahedra must buckle in order to fit into a cell that is too small. For BFO,  $\omega$  is ca. 11–14° around the polar  $[111]$  axis<sup>97</sup>.

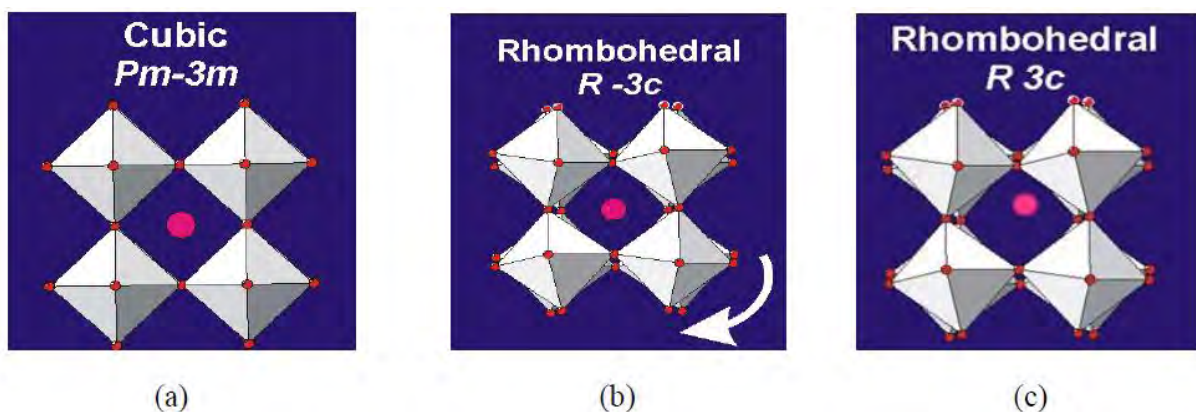


Fig. 2.22. Schematic illustration of a structural transition process (a) ideal cubic structure Pm-3m without tilting ( $a_0a_0a_0$ ); (b) R-3c structure tilted along three axes with the same angle ( $a-a-a$ ); (c) Displacement of Bi ion towards  $[111]$  direction based on R3c.

The displacement of the A-site bismuth cation (shown in Fig. 2.22) along the  $[111]$  axis brings about a non-centrosymmetric polarization resulting in the ferroelectric property. Fig. 2.22 illustrates the structural transition process.

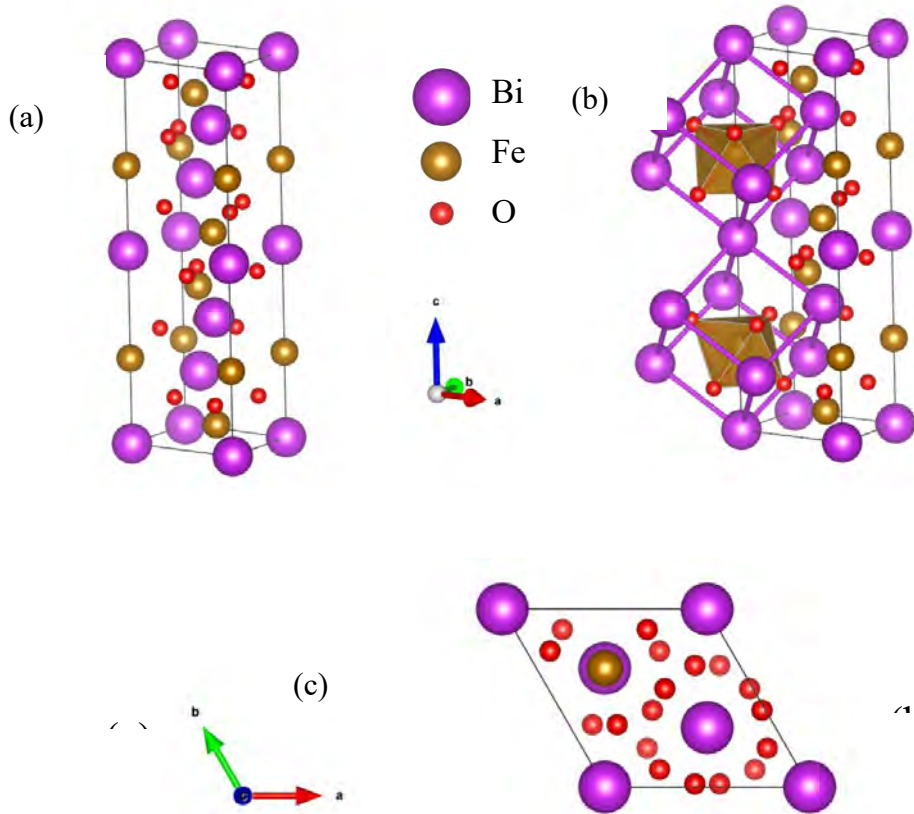


Fig. 2.23. Crystal structure of bismuth ferrite (a) in the hexagonal setting, (b) in the hexagonal setting with the distorted perovskite sub-structure shown, and (c) viewed along the  $c$ -axis. In the figure, the displacement of the  $\text{Bi}^{2+}$  ions along the  $[001]$  direction can be easily seen.

The lattice parameter and crystal structure of BFO are dependent on the temperature. It was well documented that, except for the long Bi-Fe bond distance, the lattice parameter  $a$ ,  $c$ , the volume of unit cell, the short bond distance of Bi-Fe as well as the bond angles gradually increase with increase in temperature. As a consequence of these variations, magnetism and polarization are reported to be gradually reduced, and structural phase transitions are also induced from the rhombohedrally distorted  $R3c$  perovskite structure to an orthorhombic  $Pnma$  structure and eventually to a cubic  $Pm-3m$  structure. The unit cell can also be described in a hexagonal frame of reference, with the hexagonal  $c$ -axis parallel to the diagonals of the perovskite cube, i.e.,  $[001]_{\text{hexagonal}} \parallel [111]_{\text{pseudocubic}}$ . The hexagonal lattice parameters are  $a_{\text{hex}} = 5.58 \text{ \AA}$  and  $c_{\text{hex}} = 13.90 \text{ \AA}$ <sup>23</sup>. The structure is shown in Fig. 2.23.

The  $\text{Fe}^{3+}$  ion sitting between two  $\text{Bi}^{2+}$  ions is not in the middle in Fig. 2.23 (a). The distortion of the oxygen octahedra can also be visualized in context with the pseudo-cubic perovskite setting. The bottom octahedron is rotated along the [001] axis in relation to the top octahedron, Fig. 2.23 (b). In Fig. 2.23 (c) the three-fold symmetry of the structure due to the 3-fold axes running perpendicular to the page is shown.

### 2.2.2 Magnetism of $\text{BiFeO}_3$

The magnetic properties of BFO nanoparticles with a mean size of 245 nm are very similar to those of the bulk. A magnetic response in BFO is initiated when the size of the system is less than 62 nm. The magnetic response of BFO nanoparticles greatly increases for samples below 62 nm (the period length of the spiral modulated spin structure of BFO), as compared with the bulk. The local short range magnetic ordering of BFO is G-type antiferromagnetic: each  $\text{Fe}^{3+}$  spin is surrounded by six antiparallel spins on the nearest Fe neighbors (Fig. 2.24). The antiparallel alignment is a result of the super-exchange (or Kramers–Anderson superexchange) interaction, which is the strong (usually) antiferromagnetic coupling between two next-to-nearest neighbor cations through a non-magnetic anion. In this way, it differs from direct exchange in which there is coupling between nearest neighbor cations not involving an intermediary anion<sup>100</sup>. Unlike a perfect antiferromagnet, however, the spins are not exactly anti-parallel to each other. There is a small canting angle, a slight tilt in each of the spins away from perfect co-linearity. Spin canting is due to two contrasting factors: isotropic exchange would align the spins exactly anti-parallel, while antisymmetric exchange arising from relativistic effects (spin-orbit coupling) would align the spins at  $90^\circ$  to each other. The net result, as shown in Fig. 2.25, is a small perturbation, the extent of which depends on the relative strength of these effects.

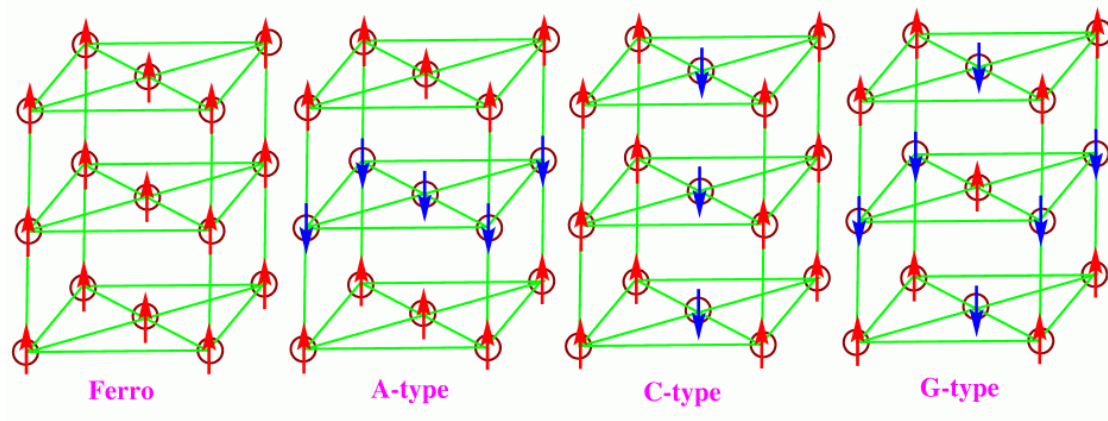


Fig. 2.24. Schematic showing different types of magnetic ordering – the last three are types of antiferromagnetism

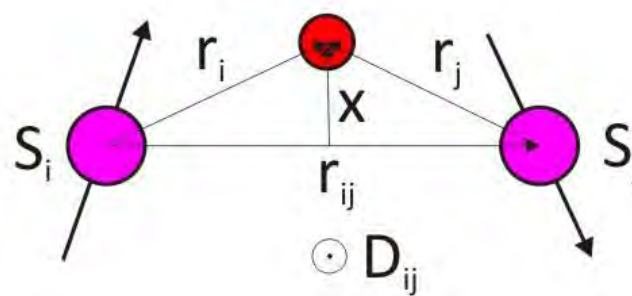


Fig. 2.25. Spin canting due to anti-symmetric exchange

### 2.2.2.1 Tuning of magnetism in BiFeO<sub>3</sub>

The antiferromagnetic nature of BFO can be changed and magnetism can be introduced into it by doping and adopting proper synthesis technique. The doping and nanoparticles (<62 nm) suppressed the spin cycloid structure and render ferromagnetism in BiFeO<sub>3</sub>.

#### *Doping induced magnetism in BiFeO<sub>3</sub>*

The substitution of Fe<sup>3+</sup> by other magnetic (Mn<sup>3+</sup>, Ni<sup>2+</sup>, Co<sup>2+</sup>, Cr<sup>3+</sup> etc.) or non- magnetic (Ti<sup>4+</sup>, Ta<sup>5+</sup>, Zr<sup>4+</sup>, Nb<sup>5+</sup> etc.) ions will have an effect on the magnetic properties of bismuth ferrite. Non-magnetic, i.e d<sup>0</sup> ions will act as ‘spin vacancies’ in the magnetic sub-structure and thus will have impact on the total cycloid and magnetic behavior. Similarly, other magnetic ions with spin magnetic moment unequal to Fe<sup>3+</sup> will alter the magnetic structure because now, the

anti-alignment will leave a local net magnetic moment due to unequal spins on the foreign ion and  $\text{Fe}^{3+}$  ion; a sort of local ferrimagnetism. Moreover, B-site doping may indirectly influence the spin arrangement by causing structural distortion which alters the Fe-O-Fe bond length/angle, change in symmetry of the crystal structure giving rise to modified interactions between the  $\text{Fe}^{3+}$  ions, or the dopant ion may itself be magnetic and have a direct influence on the magnetic property of BFO. Recently, doping with tri-positive rare-earth ions ( $\text{R}^{3+}$ ) at the Bi site has been proposed to mitigate some of the issues mentioned above.<sup>25</sup> Previous reports suggest that 10 mol.% Holmium ( $\text{Ho}^{3+}$ ) doping at Bi site increases the magnetization by 6 times compared to pure BFO

### *Synthesis method to tune magnetism of $\text{BiFeO}_3$*

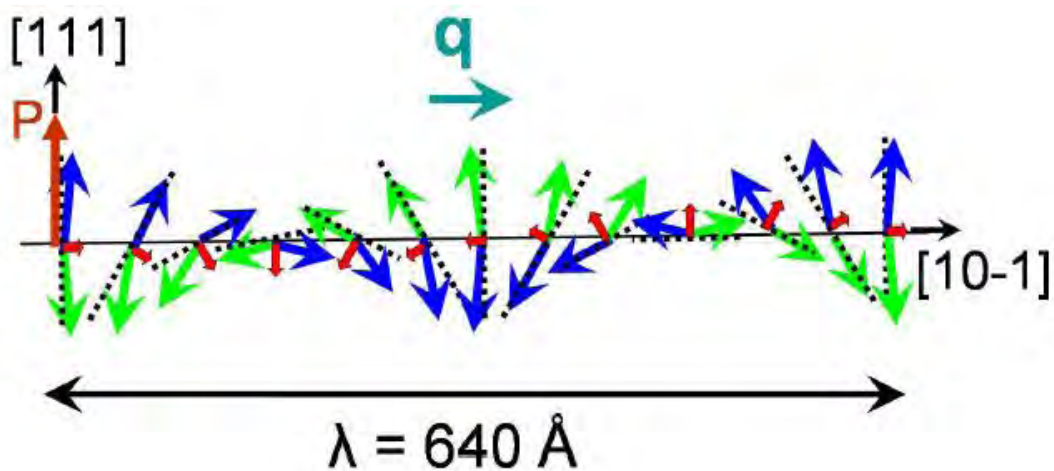


Fig. 2.26: Schematics of the 64 nm antiferromagnetic circular cycloid.

The magnetic ordering of BFO is G-type antiferromagnet: each  $\text{Fe}^{3+}$  spin is surrounded by six nearly antiparallel spins on the nearest Fe neighbours (Fig. 2.26). The antiferromagnetic spin ordering is not homogeneous but is manifested as an incommensurate cycloid structure with a wavelength of  $\sim 64 \text{ nm}$  along  $\langle 110 \rangle$ , as can be seen in Fig. 2.26.<sup>101</sup> In this cycloid structure the net magnetic moment of the spins cancel out each other and results in zero net magnetization.

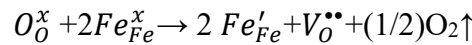
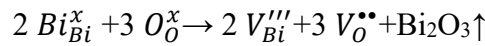
The canted antiferromagnetic spins (blue and green arrows) give rise to a net magnetic moment (purple arrows) that is specially averaged out to zero due to the cycloidal rotation. The spins are contained within the plane defined by the polarization vector.<sup>102</sup>



When the nanoparticle size of BFO is smaller than 62 nm, it achieves magnetism. Nanoparticles can be produced by hydrothermal, sol-gel, co-precipitation and pechini method etc.

### 2.2.3 Electrical properties of BiFeO<sub>3</sub>

The leakage current of pure BFO from a previous study is found to be  $5.9 \times 10^{-5}$  A/cm<sup>2</sup> at 5.71 kV/cm<sup>103</sup>. The following Kroger-Vink notations are usually used to explain the leakage behavior of BFO by virtue of formation of oxygen and Bi vacancies and charge variation of Fe (Fe<sup>2+</sup>/Fe<sup>3+</sup>)<sup>104,105</sup>.



where  $Bi_{Bi}^x$ ,  $Fe_{Fe}^x$  and  $O_O^x$  are the Bi, Fe and oxygen ions respectively in the lattice,  $V_{Bi}'''$ ,  $V_O^{''}$  indicate Bi and oxygen vacancies with three negative and two positive charges respectively.

#### 2.2.3.1 Engineering of electrical properties in BiFeO<sub>3</sub>

The suppression of oxygen vacancies in BFO is only way to reduce leakage current in BFO. Different types of doping make stronger bond with oxygen and hence reduces the tendency of sublimation from the lattice of BFO.

##### *Doping to improve electrical properties*

The presence of oxygen vacancies causes bulk BFO to exhibit high leakage current making it difficult to achieve good ferroelectric properties. The ion doping of BFO has been widely explored to reduce the leakage current, improve the ferroelectric behavior, and strengthen the magnetoelectric (ME) coupling in BFO, Gd<sup>3+</sup>, Eu<sup>3+</sup>, Ba<sup>2+</sup>, Sr<sup>2+</sup> and Ho<sup>3+</sup> as A-site substitutions have been found to improve the stability of the structure, improve the magnetic properties and also reduce the tendency of the second phase formation during the synthesis of BFO<sup>106-109</sup>.

### 2.2.4 Optical properties of BiFeO<sub>3</sub>

The band structure of BFO has its conduction band composed of Fe 3d states and valence band of O 2p states, and the electronic transitions involved O:2p → Fe :3d charge transfer transitions, which could be a combination of MMLT (metal to metal charge transfer) or LMCT (ligand to metal charge transfer transition)<sup>110</sup> as shown in Fig. 2.27. Illumination of BFO promotes electrons transition from the valence band to the conduction band, leaving behind positively charged holes.

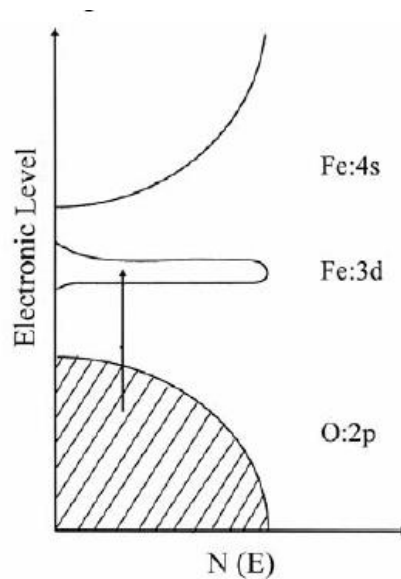


Fig. 2.27. Band structure for doped BFO

The absorbance spectra of BFO can be obtained from diffused reflectance data using Kubelka-Munk conversion function.<sup>111</sup>

The diffused reflectance data is converted to Kubelka-Munk function given by the following equation:

$$F(R) = \frac{(1 - R)^2}{2R}$$

where R is the diffused reflectance value. The band gap of doped BFO nanoparticles is obtained from  $[E * F(R)]^2$  vs E plot.

### 2.2.4.1 Tuning of optical properties in BiFeO<sub>3</sub>

The optical properties of BFO is tuned by doping which creates an intermediate layer between O 2p and Fe 3d. This phenomenon reduces the ultimate optical transition energy for BFO.

#### *Effect of doping on optical properties*

The doping of Sm, Ca, and Gd at Bi site,<sup>112</sup> and Mn, Ta at Fe sites<sup>23,94</sup> reduces the band gap of BFO. There may be several reasons behind this reduction of band gap in the doped BFO samples. For example a first principles calculation has shown that due to reduced degree of hybridization associated with a stable electronic configuration a unique energy level is formed in between Fe 3d and O 2p and therefore reduces effective band gap of doped BFO<sup>113</sup>. Moreover, previous investigations have shown that the changes in Fe-O bond length and Fe-O-Fe bond angle by cation doping plays a critical role in modifying one-electron bandwidth and hence band gap of BFO<sup>114</sup>.

### 2.2.5 Application of BiFeO<sub>3</sub>

#### 2.2.5.1 Ferroelectric and piezoelectric devices

Being a room-temperature multiferroic, BFO is an obvious candidate for applications. Interestingly, however, the first application that may reach the market might not use the multiferroic properties of BFO at all. The remnant polarization of BFO is very large, 100  $\mu\text{C}/\text{cm}^2$  along the polar  $[111]_{\text{pc}}$  direction. To put this into context, this is the biggest switchable polarization of any perovskite ferroelectric, and is roughly twice as big as the polarization of the most widely used material in ferroelectric memories, Lead Zirconate Titanate (PZT). Moreover, unlike PZT, BFO is a lead-free material, a bonus regarding health and safety. It is therefore not surprising that manufacturers of ferroelectric memories such as Fujitsu are considering BFO as the potential active material in their next generation of ferroelectric memory devices. For such an application to ever come into fruition, however, important obstacles must be removed, such as:

- i) the higher conductivity (and thus also higher dielectric losses) of BFO relative to PZT,
- ii) its tendency to fatigue<sup>115</sup>, and

- iii) the fact that it appears to thermally decompose at voltages quite close to the coercive voltage.<sup>116</sup>

A second potential application unrelated to magnetoelectric properties is piezoelectricity. The piezoelectric coefficient of pure BFO is actually quite small. However, its rhombohedral ground state means that mixing it with a tetragonal ferroelectric such as PbTiO<sub>3</sub> leads to a morphotropic phase boundary (MPB) at a composition of 30% mol PbTiO<sub>3</sub>.<sup>117</sup>

This is important because MPBs are commonly thought to be the key behind the large piezoelectric coefficients of PZT and relaxors,<sup>117</sup> so the MPB of BFO–PT might lead to equally large piezoelectric constants. A newer MPB with enhanced piezoelectric coefficients has been reported<sup>118</sup> for a solid solution of rhombohedral BFO with orthorhombic SmFeO<sub>3</sub>; it is likely that other solid solutions between BFO and any of the other orthoferrites should also display similar MPBs. In this context, it is surprising that the widely studied solid solution between BFO and LaFeO<sub>3</sub> does not appear to have yet been piezoelectrically characterized; perhaps this is due to its high conductivity.

### 2.2.5.2 Spintronics

The real drivers behind most of the applied research on BFO are magnetoelectric and spintronic applications<sup>119</sup>. Chief among these would be memories that can be written using a voltage and read using a magnetic field. Using a voltage for writing has three advantages:

- i) this can be implemented in a solid-state circuit without mobile parts,
- ii) it has a low-energy requirement, and
- iii) the voltage requirements automatically scale down with thickness.

Reading the memory magnetically, on the other hand, has the advantage that it is a non-destructive readout process, unlike direct ferroelectric reading, which requires switching the polarization in order to read it. For such memories to actually work, the magnetic state therefore must be, a) electrically switchable and b) magnetically readable.

The first condition is met by BFO, because the easy plane of its antiferromagnetic domains is correlated with the polar direction, and rotating the ferroelectric polarization results in a rotation of the sub lattice magnetization<sup>120</sup>, i.e., the magnetic state of the sample can be changed

by a voltage. On the other hand, the second condition is not directly met, because antiferromagnetic (or, at best, weakly canted antiferromagnetic) domains cannot be easily read.

An elegant solution to the problem of reading antiferromagnetic states consists of using the mechanism known as exchange bias. Briefly, exchange bias is the magnetic interaction between the spins at the uppermost layer of an antiferromagnet and a thin ferromagnetic layer attached to it. The exchange bias modifies the hysteresis loops of the ferromagnetic layer, either offsetting or widening them. What is relevant here is that voltage-induced changes to the underlying antiferromagnetic domains will result in changes to the ferromagnetic hysteresis of the upper layer, which can then be read by conventional mechanisms. The implementation of this concept for  $\text{Cr}_2\text{O}_3$  (which is magnetoelectric but not ferroelectric) was first done by Borisov et al.<sup>121</sup>, and the first investigation with an actual multiferroic ( $\text{YMnO}_3$ ) was done by Laukhin et al.<sup>122</sup>.

The race to implement this idea using BFO (which has the advantage over  $\text{YMnO}_3$  that it works at room temperature) has been on for a while, and has been punctuated by several important milestones, such as the observation of exchange bias in thin ferromagnetic layers grown on BFO, the correlation between exchange bias and ferroelectric domains<sup>123</sup>, the observation that the antiferromagnetic domains can be switched by a voltage<sup>120</sup>, and, most recently, the final proof of- concept that the exchange-biased ferromagnetic layer can indeed be switched by a voltage.

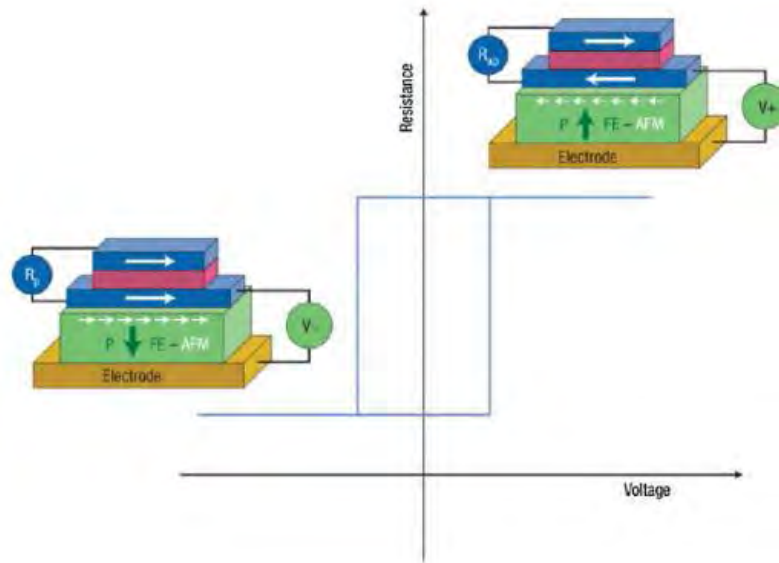


Fig. 2.28. MERAM based on exchange-bias coupling between a multiferroic that is ferroelectric and antiferromagnetic (FE-AFM, green layer), and a thin ferromagnetic electrode (blue). A tunneling barrier layer between the two top ferromagnetic layers provides the two resistive states. Interestingly, BFO could act not only as the magnetoelectric active layer, but also as the tunneling barrier.

A second line of work uses BFO as a barrier layer in spintronics. Sandwiching BFO between two ferromagnetic metals results in tunneling magnetoresistance <sup>123</sup>. For this, the only requirement is that the BFO layer be reasonably insulating down to tunneling thicknesses. However, an extra ingredient provided by BFO is the fact that it also remains a robust and switchable ferroelectric down to a thickness of 2 nm, and thus it could in principle be used as an electrically switchable tunnel junction, whereby the ferroelectric state controls the magnetic state of the thin ferromagnetic electrodes, thus modifying the tunneling magnetoresistance. A similar concept using a ferromagnetic multiferroic (La-BMO) was indeed demonstrated by Gajek et al.<sup>124</sup>, who showed that the tunneling resistivity could be controlled both by electric and magnetic fields, giving rise to a four-state memory device. The voltage-dependent barrier characteristics of BFO have not yet been established.

The above developments show that, at least in principle, it is now possible to develop an MERAM (Magnetoelectric Random Access Memory) based on BFO. A schematic of such a device has been proposed by Bibes and Barthelemy <sup>124</sup>, and is reproduced in Fig. 2.28.

### 2.2.5.3 Photocatalyst

One important technique for removing industrial waste is the use of light energy (electromagnetic radiation) and particles sensitive to this energy to mineralized waste which aids in its removal from solution. Multifunctional oxides have shown to be promising participants for photocatalytic applications, and accordingly, water insoluble  $\text{TiO}_2$  is one of the most efficient photocatalytic semiconductor due to its high quantum yield<sup>1</sup>. The recent research conveys the information at that stage where the large energy band gap (i.e.  $\sim 3.2$  eV) restricts the  $\text{TiO}_2$ , the narrow band gap (i.e.  $\sim 2.1$  eV) of multifunctional BFO and its excellent chemical stability makes it suitable for visible- light responsive photo-catalysis for water splitting and degradation of organic-inorganic pollutants<sup>125</sup>. The photocatalytic activity of the BFO is evaluated by degradation of Congo Red and Rhodamine B under the irradiation of visible light.

Generally, the photocatalysis process involves four stages: generation of photoinduced electron-hole pairs excited by incident light, transport of photoinduced carriers to the photocatalyst surface, recombination of electron-hole pairs internally or at the surface of photocatalyst, and subsequent reduction/oxidization of the adsorbed reactants directly by electrons/holes or indirectly by reactive oxygen species.

The hydroxyl radicals are produced during photocatalytic reaction, since the valence band potential is positive enough, and simultaneously,  $\text{O}_2$  is reduced to the conduction band potential, which is negative enough. The hydroxyl radical (or hole) is a powerful oxidizing agent and degrades organic pollutants in the vicinity of a semiconductor surface<sup>126</sup>. When BFO is doped additional surface states or sub-bands are created within the charge gap of the material and this acts in combination with the increased probability of charge carriers reacting at the surface due to reduced diffusion lengths<sup>126</sup>. This could be the reason for increased photocatalytic activity of doped BFO materials compared to undoped materials<sup>126</sup>.

### 2.2.6 Synthesis of $\text{BiFeO}_3$

Recent approaches have focused on developing novel structures such as zero-, one-, and two dimensional nanostructures of BFO. Up to now, several wet chemical routes (co-precipitation, hydrothermal, solvothermal, sonochemical, sol-gel and combustion) have been developed for the synthesis of BFO powders<sup>127-129</sup>. The most convenient methodology used to produce

nanoparticles is variations of the sol-gel technique (mostly Pechini technique)<sup>23</sup>. These methods allow the synthesis of particles ranging in size from less than 15 nm to greater than 100 nm. The Pechini method belongs to the sol–gel category of fabrication methods. In this method, an ahydroxy carboxylic-containing compound forms a polybasic acid chelate with metal cations; which successively polymerize with a polyhydroxy alcohol. After calcination process, nanometer-sized powders are achieved. When compared to other sol-gel methods, the Pechini- method has better compositional homogeneity, lower toxicity and lower cost. The method’s advantages include its relative simplicity.

### 2.2.6.1 Microwave associated hydrothermal synthesis

For the synthesis of BFO, an aqueous solution mixture of bismuth nitrate pentahydrate  $\text{Bi}(\text{NO}_3)_3 \cdot 5\text{H}_2\text{O}$  and iron nitrate nonahydrate ( $\text{Fe}(\text{NO}_3)_3 \cdot 9\text{H}_2\text{O}$ ) with the molar ratio of 1:1 are prepared firstly using stirring<sup>127</sup>. After that, NaOH solution (1.0 g/ L) and polyethylene glycol (1.5 g/ L) are slowly added to the mixture for the purpose of obtaining a brown precipitate under constant stirring 15.0 min.

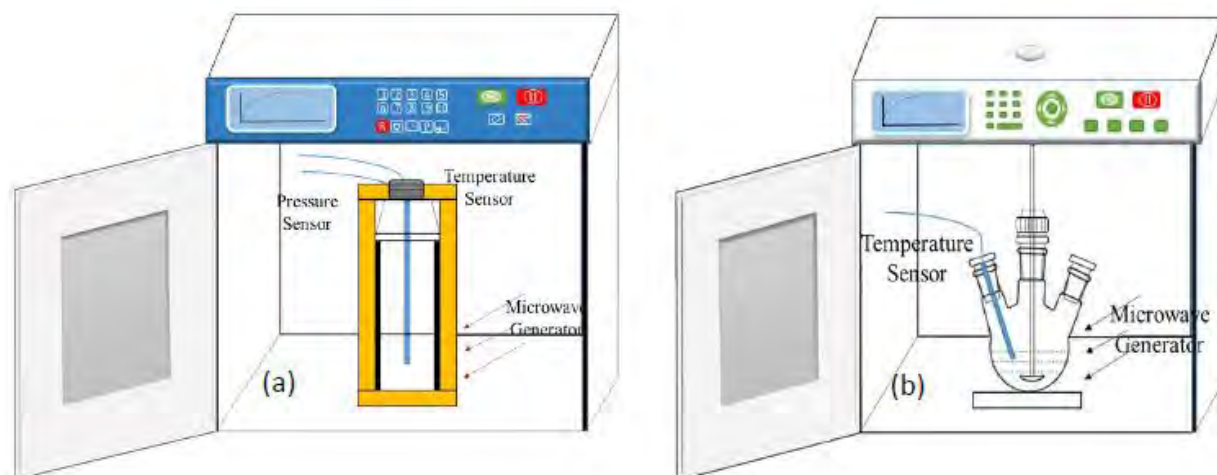


Fig. 2.29. (a) The experiment device schematic diagrams for synthesis and (b) reaction.

Subsequently, the solution is irradiated by 300.0 W of microwave irradiation for 30.0 min at constant temperature (190.0 °C) in a microwave oven (MDS-6G, Shanghai Sineo Microwave Chemistry Technology Co., Ltd, China, see Fig. 2.29) with frequency of 2450.0 Hz. The black powder generated by microwave irradiation and collected by filtration is washed using distilled



water and ethanol for three times. Finally, the obtained catalyst is dried in a vacuum drying oven at 60.0 °C for 12.0 h and ground into fine powder.

### **2.2.6.2 Co-precipitation route**

Amorphous powder of multiferroic BFO can be successfully synthesized by a cost effective co-precipitation route at low temperature (80 °C) <sup>128</sup>. The analytical grade iron nitrate nonahydrate  $\text{Fe}(\text{NO}_3)_3 \cdot 9\text{H}_2\text{O}$  and commercial grade bismuth oxide  $\text{Bi}_2\text{O}_3$  (99.98 % pure) are used as precursors. These are dissolved in nitric acid ( $\text{HNO}_3$ ) and deionized water to form solutions of 0.4 M. Both the solutions are mixed and stirred for 30 min to obtain a uniform transparent ionic mixture. An aqueous solution of sodium hydroxide ( $\text{NaOH}$ ) prepared in deionized water of 1.0 M is used as a precipitating agent. It is mixed quickly into the ionic solution during stirring on a hot plate heater to form uniform precipitates. For phase-purity and desired crystallite size, a value of  $\text{pH} = 12$  is maintained at 30 °C. After vigorous stirring for 30 min, the temperature of the solution is raised to  $80 \pm 2$  °C and kept it for 45 min to transform hydroxides into ferrite. The solution thus obtained is washed successively with deionized water till a  $\text{pH}$  of 7 was achieved. The precipitates thus obtained are dried in an electric oven at 100 °C. Dried chunks are ground in a mortar and pestle to obtain an amorphous powder. For crystallization and phase formation, powder is calcined at different temperatures (400–600) °C for 1 h with a step of 50 °C. For other characterization, powder is uniaxially pressed at a pressure of 10 MPa into green pellets. These pellets are further densified by cold iso-static pressing at 250 MPa and sintered at 500 °C for 2 h. All the heat treatments are carried out in the air.

### **2.2.6.3 Pechini sol-gel route**

Among the various wet chemical processes, the Pechini sol-gel route is found to be simple and cost effective for the synthesis of homogeneous and very fine crystalline nanopowders. The process is based on the mixing of reactants that oxidize easily, such as metal nitrates, and an organic chelating agent that acts as reducing agent. The various advantages of sol-gel synthesis as the prime method for the production of BFO are

- Self-purification due to the high exothermic temperatures involvement.

- Formation of nano- powders in the desired size and shape with uniform particle size distribution.
- Simple and cost effective.
- Synthesis of single phase materials at very low temperatures

Bismuth ferrite is prepared by a modified Pechini sol-gel method using citric acid as the chelating agent. In this process, stoichiometric proportion of  $\text{Bi}(\text{NO}_3)_3 \cdot 5\text{H}_2\text{O}$  and  $\text{Fe}(\text{NO}_3)_3 \cdot 9\text{H}_2\text{O}$  are initially dissolved in deionized water. The solution is stirred for about half an hour to obtain a clear solution. When the solution is transparent, citric acid ( $\text{C}_6\text{H}_8\text{O}_7$ ) as the chelating agent is added to the solution to complex the metal cations. The solution is then stirred and heated at 70-75 °C for 8-10 hrs to form a transparent blackish-red sol. Afterwards appropriate amount of ethylene glycol is added to the solution as polymerization agent. The resultant solution is heated at 85-90 °C to initiate the polymerization reaction and a few minutes later a gel is formed with vigorous boiling and fuming. The gel was dried at 100 °C for 24 hrs in a drier to obtain fluffy green xerogel. The xerogel samples are then ground into powders and annealed at 400-600 °C for 2 hrs in static air to get BFO nanoparticles.

# **3 EXPERIMENTAL**

### 3.1 Introduction

The specific aim of this work is to fabricate  $\text{TiO}_2\text{-Bi}_{0.9}\text{Ho}_{0.1}\text{FeO}_3$  composite thin film with a concentration on improving the optical, electrical and magnetic properties of  $\text{TiO}_2$ .

Keeping this in mind, there are three principal objectives of this work. These are:

- (a) Synthesis of multiferroic  $\text{Bi}_{0.9}\text{Ho}_{0.1}\text{FeO}_3$  (BHFO) nanoparticles,
- (b) Synthesis of pure  $\text{TiO}_2$  thin film and  $\text{TiO}_2\text{-BHFO}$  composite thin film, and
- (c) Investigation of the structural and functional properties of BHFO nanoparticles,  $\text{TiO}_2$  thin film and  $\text{TiO}_2\text{-BHFO}$  composite thin film.

### 3.2 Materials

Bismuth nitrate pentahydrate ( $\text{Bi}(\text{NO}_3)_3 \cdot 5\text{H}_2\text{O}$ , Merck -India), iron nitrate nonahydrate ( $\text{Fe}(\text{NO}_3)_3 \cdot 9\text{H}_2\text{O}$ , Merck-India), holmium nitrate pentahydrate ( $\text{Ho}(\text{NO}_3)_3 \cdot 5\text{H}_2\text{O}$ , Sigma Adrich-USA), citric acid ( $\text{C}_6\text{H}_8\text{O}_7$ , Merck -India) and ethylene glycol ( $\text{C}_2\text{H}_6\text{O}_2$ , Merck -India) were used for the synthesis of BHFO nanoparticles. In this case,  $\text{C}_6\text{H}_8\text{O}_7$  acted as the chelating agent to complex the metal cations and  $\text{C}_2\text{H}_6\text{O}_2$  was added as polymerization agent.<sup>23</sup>

The solutions of pure  $\text{TiO}_2$  thin film and  $\text{TiO}_2\text{-Bi}_{0.9}\text{Ho}_{0.1}\text{FeO}_3$  composite thin films were prepared using titanium(IV) n-butoxide ( $\text{Ti}(\text{O-nBu})_4$ , Aldrich-USA) as precursor and n-butyl alcohol (n-BuOH, Merck-India) as solvent. Besides, acetylacetone ( $\text{C}_5\text{H}_8\text{O}_2$ , Loba chemie) was added in the solution as chelating agent to decrease the reactivity of  $\text{Ti}(\text{O-nBu})_4$ .<sup>130</sup> Glacial acetic acid ( $\text{CH}_3\text{COOH}$ , Qualikems) was used further to begin hydrolysis via an esterification reaction.

### 3.3 Synthesis of BHFO Nanoparticles

BHFO nanoparticles were synthesized using a modified sol-gel method.<sup>23</sup>

- For a typical 1 g BHFO powder synthesis process, stoichiometric proportion of  $\text{Bi}(\text{NO}_3)_3 \cdot 5\text{H}_2\text{O}$  (0.003 mol),  $\text{Fe}(\text{NO}_3)_3 \cdot 9\text{H}_2\text{O}$  (0.0033 mol),  $\text{Ho}(\text{NO}_3)_3 \cdot 5\text{H}_2\text{O}$  (0.00033 mol),  $\text{C}_6\text{H}_8\text{O}_7$  (0.0067 mol) and  $\text{C}_2\text{H}_6\text{O}_2$  (10 ml) were dissolved in 400 ml deionized water.

- Consecutively the solution was heated under continuous stirring at 75-85 °C for 4h to obtain gel. The gel was dried at 100 °C for 24 h in a drier to obtain precursor xerogel.
- The ground precursor xerogel powders were annealed at 500 °C for two hours with a heating rate of 3 °C/ min to obtain BHFO nanoparticles.
- BHFO pellets (thickness 0.11 cm and diameter= 1.3 cm) were prepared by mixing precursor xerogel powders with PVA binder followed by pressing (5 tons pressure) and annealing at 500 °C with a heating rate of 3 °C / min to measure electrical properties.

### 3.4 Synthesis of Thin Films

#### 3.4.1 Synthesis of pure titania (TiO<sub>2</sub>) thin film

Pure TiO<sub>2</sub> thin film was fabricated using non-aqueous sol-gel method.<sup>130</sup>

- First off, n-BuOH (0.0884 mol) and C<sub>5</sub>H<sub>8</sub>O<sub>2</sub> (0.0015 mol) were mixed and, then Ti(O-nBu)<sub>4</sub> (0.005 mol) was added to the solution.
- Subsequently this mixture was stirred for 30 min at room temperature. CH<sub>3</sub>COOH (0.001 mol) was slowly added into the alkoxide solution and stirred continuously for another 30 min. Concentration of the final solution was 0.5 M and its color was yellowish.
- The yellowish solution was spin-coated onto the 2.5 x 2 cm<sup>2</sup> glass substrate at 2000 rpm for 30 s and dried at 200 °C for 10 mins. Micro pipette was used to ensure that specific amount of solution was taken every time.
- The spin-coating and drying processes were repeated three times. The pure film was annealed in static air at 500 °C for 2 h with a heating rate of 3 °C/ min.

#### 3.4.2 Synthesis of TiO<sub>2</sub> - BHFO composite thin film

Thin films containing 5 mol.% BHFO (marked as T<sup>95</sup>B<sup>5</sup>), 10 mol.% BHFO (marked as T<sup>90</sup>B<sup>10</sup>) and 20 mol.% BHFO (marked as T<sup>80</sup>B<sup>20</sup>) were prepared using non-aqueous sol-gel method . Fig. 3.1 illustrates the synthesis process of composite film.

- To synthesize composite films, molar amount of n-BuOH, C<sub>5</sub>H<sub>8</sub>O<sub>2</sub>, Ti(O-nBu)<sub>4</sub> and CH<sub>3</sub>COOH was kept similar as that of pure thin film.

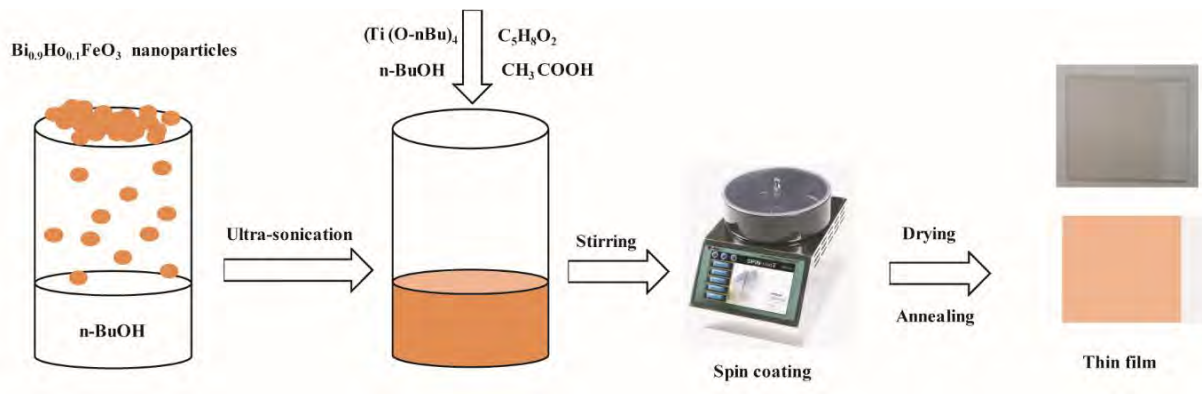


Fig. 3.1. Schematic representation of preparation process of composite thin films

- Firstly 0.0442 mol of  $\text{n-BuOH}$  was taken and calculated amount of BHFO nanoparticles was mixed into it for every composite film.
- The whole mixture was dispersed vigorously in an ultrasonic bath for 30 min to avoid the aggregation of BHFO nanoparticles.
- Then  $\text{C}_5\text{H}_8\text{O}_2$ ,  $\text{Ti}(\text{O-nBu})_4$  and rest of  $\text{n-BuOH}$  (0.0442 mol) were added into this mixture and it was stirred for 30 min on a stirring plate at room temperature.
- This mixture was then taken into ultrasonic bath in which  $\text{CH}_3\text{COOH}$  was added dropwise.
- The final mixture was under intensive stirring for 2 h in an ultrasonic bath. The prepared mixture eventually turned into brownish color.
- The brownish solution was spin-coated onto the  $2.5 \times 2 \text{ cm}^2$  glass substrate at 2000 rpm for 30 s and dried at  $200 \text{ }^\circ\text{C}$  for 10 mins. During coating brownish solution was in stirring state continuously so that BHFO nanoparticles did not settle down. Micro pipette was used to ensure that specific amount of solution was taken every time.
- The spin-coating and drying processes were repeated three times. The composite films were annealed in static air at  $500 \text{ }^\circ\text{C}$  for 2 h with a heating rate of  $3 \text{ }^\circ\text{C}/\text{min}$ .

### 3.5 Characterization

#### 3.5.1 Field emission scanning electron microscopy (FESEM)

Field emission scanning electron microscope (FESEM: JEOL, JSM,7600F) was employed to monitor the size and shape of nanoparticles. FESEM was utilized to determine the grain size, shape and roughness of thin films, and to determine the thickness of these thin films. Energy

dispersive X-ray spectroscopy (EDS) was used for mapping the elements present in the thin films. Prior to insertion in the FESEM, the samples were coated with platinum by ion sputtering method. This is required to make the sample conductive and so circumvent the charging phenomenon. Grain size was estimated by Image J software.

### **3.5.2 Crystal structure determination and phase identification**

X-Ray Diffractometer (PANalytical Empyrean) was used for structural and phase analysis of nanoparticles and thin films utilizing a Cu x-ray source (wavelength:  $K\alpha_1 = 1.540598 \text{ \AA}$  and  $K\alpha_2 = 1.544426 \text{ \AA}$ ). The diffraction was performed using Bragg angles between  $2\theta = 10^\circ$  to  $90^\circ$ . The Rietveld refinement of BHFO nanoparticles was done using FULLPROF software<sup>131</sup>.

### **3.5.3 Optical absorption measurement**

The absorption coefficient and band gap of nanoparticles and thin films were evaluated using UV/Vis/ NIR spectrometer (Perkin Elmer, Lambda 1050). A specific amount of BHFO nanoparticles was loaded on a holder and this holder was inserted into the spectrometer. On the other hand, there was no sample preparation step for thin films.

### **3.5.4 Magnetic properties determination**

The room temperature magnetic properties such as coercivity ( $H_c$ ) and saturation magnetization ( $M_s$ ) were determined using vibrating sample magnetometer (VSM: EV-9 Microsense). To measure the magnetic property of the thin films, 5 mm x 5 mm size sample was cut from every thin film substrate. On the other hand, 12 mg BHFO nanoparticles was taken to determine its magnetization.

### **3.5.5 Electrical characterization**

The conductivity of BHFO was measured using Precision Materials Analyzer (Radiant Technologies, Inc.: P-PMF, PMF0215-377). To measure the conductivity of BHFO, the pellet was coated on its both sides with silver paste.

On the other hand, Hall measurement was carried out using the van der Pauw configuration method (HMS-3300). The four points contacts were made by indium tin alloy soldering which enabled us to obtain the carrier concentration, resistivity and mobility of thin films.

# **4 RESULTS AND DISCUSSION**



## 4.1 X-Ray Diffraction Analysis

Fig. 4.1 shows room temperature XRD patterns of nanoparticles, pure TiO<sub>2</sub> thin film and TiO<sub>2</sub>-BHFO composite thin films. The obtained pattern of TiO<sub>2</sub> as depicted in Fig. 4.1 (a) shows satisfactory correspondence with anatase phase. The diffraction peaks at  $2\theta = 25.2^\circ$  (101),  $37.8^\circ$  (004),  $48.0^\circ$  (200),  $53.9^\circ$  (105) and  $55.1^\circ$  (211) are matched well with the standard diffraction data of tetragonal crystal structure of TiO<sub>2</sub>.<sup>132</sup>

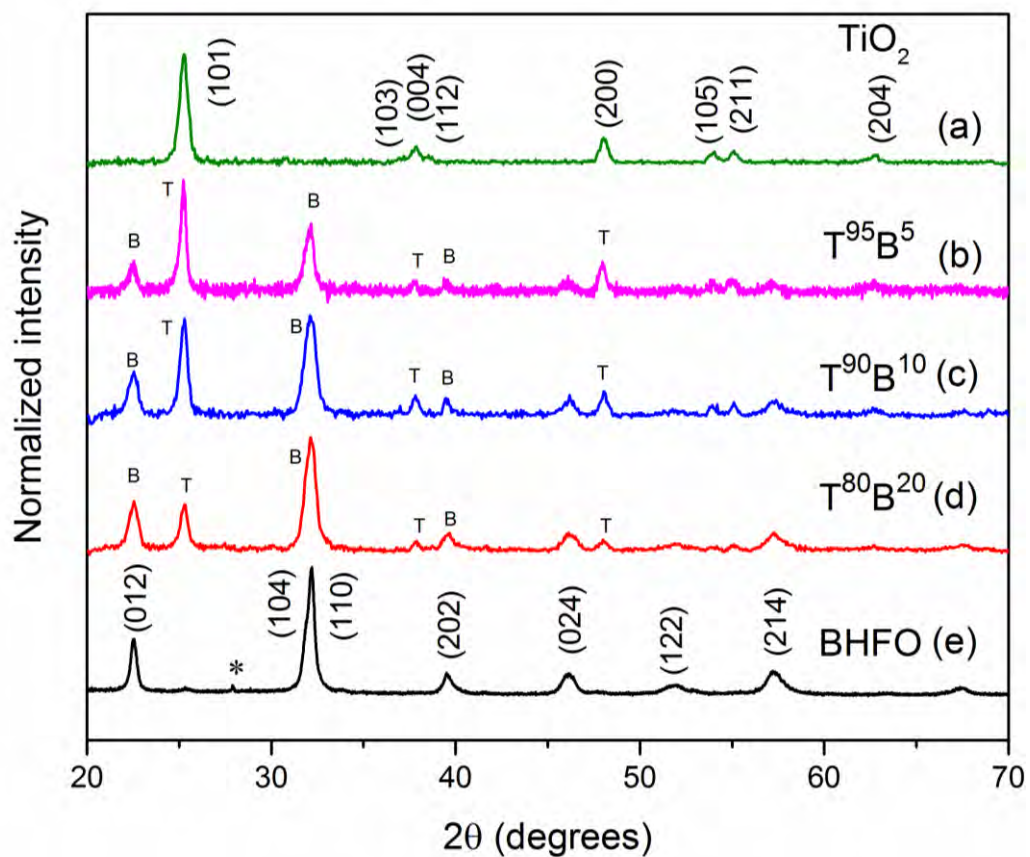


Fig.4.1. XRD patterns of the prepared pure film, composite films and nanoparticles. Here B and T stand for some major peaks of BHFO and TiO<sub>2</sub> respectively

Thus, it is confirmed that the annealed TiO<sub>2</sub> film deposited on glass substrates has anatase phase with no trace of other polymorphs of TiO<sub>2</sub> (e.g., rutile and brookite).

On the other hand, XRD pattern of BHFO nanoparticles as shown in Fig. 4.1(e) is in line with previous report of Ho<sup>3+</sup> doped BFO ceramics.<sup>133</sup> In addition to the desired spectra, one extra

peak [marked by asterisk (\*)] becomes visible which indicates the presence of impurity phase. Generally, pure BFO crystallizes in a rhombohedrally distorted perovskite structure, which belongs to the space group R3c. The perovskite structure of BFO transforms from rhombohedral (R3c) to tetragonal (P4 mm) or orthorhombic (Pnma) or cubic (Pm-3m) and so on depending on the nature of the A site and B site doping.<sup>134-136</sup> As a result, diversified structural reports are available for Bi<sub>0.9</sub>Ho<sub>0.1</sub>FeO<sub>3</sub> (BHFO) in which the neighboring peaks such as (012), (110)/(104), (006)/(202), (116)/(112) and (018/214) are merged together.<sup>133,137</sup> It can be appreciated by observing the XRD patterns in Fig. 4.2 and Fig. 4.3 that substantial structural modification has occurred in the Ho substituted BFO nanoparticles in the current study.

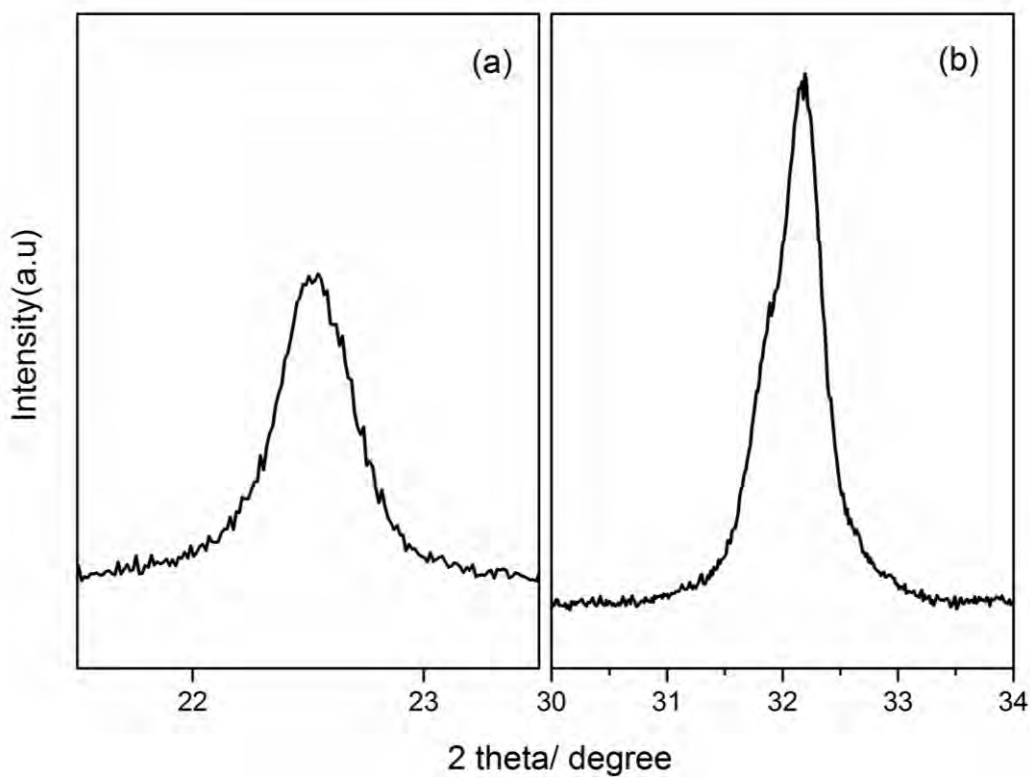


Fig. 4.2. Magnified XRD patterns of BHFO nanoparticles in the range of (a) 2 theta/degree = 21.5-23.5° and (b) 2 theta/degree = 30- 34°.

A magnified portions of XRD patterns (see Fig. 4.2) for the ranges of  $2\theta = 21.5^\circ$ - $23^\circ$  and  $2\theta = 30^\circ$ - $34^\circ$  shows that there is partial merging of (012) and (110)/(104) peaks, which immediately indicates a possible structural transition in the synthesized BHFO nanoparticles. This possible

merging due to ion doping has been reported in previous studies as an indication of rhombohedral to orthorhombic or tetragonal phase transition.<sup>138</sup>

To uncover the crystal structure and the impurity phase, Rietveld refinement of BHFO was carried out using the FULLPROF software.<sup>131</sup> Weight fraction of the phases, lattice parameters and Rietveld agreement factors are listed in Table 4.1 and fitted plot of XRD pattern is shown in Fig. 4.3.

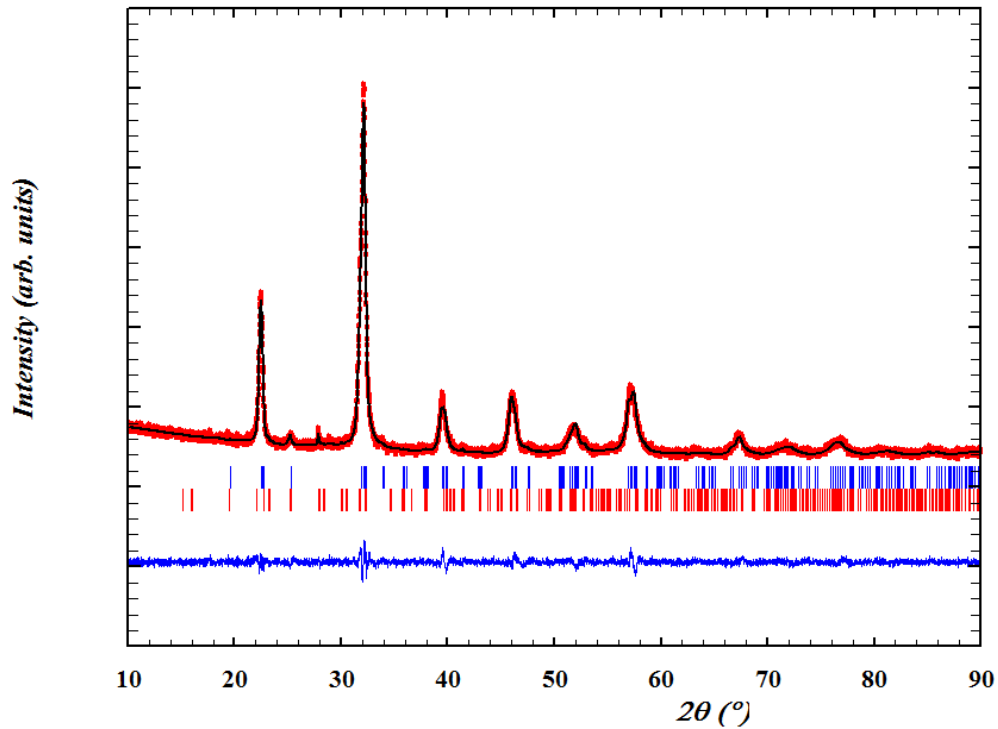


Fig. 4.3. Plot showing the observed (red dot), calculated (black line), and difference (blue line) patterns obtained from Rietveld refinement. First and second row of ticks indicates Bragg positions for the Pnma phase and Pbam phase respectively.

Table 4.1. Summary of data obtained from Rietveld refinement and agreement factors of BHFO nanoparticles

Sample	Phase(s) present	Unit cell parameters	Bond length (Å)	Bond angle	Rietveld factors
BHFO	Pnma 91.42 %	a=5.544209 Å b= 5.614142 Å c= 7.835147 Å V = 243.9 Å <sup>3</sup>	B-O1=2.18 B-O2=2.12 Fe-O1=1.49 Fe-O2=1.82	Fe-O1-Fe=147.91 Fe-O2-Fe=151.33	R <sub>p</sub> = 19.6 R <sub>wp</sub> = 15.7 R <sub>exp</sub> = 13.1
	Pbam Bi <sub>2</sub> Fe <sub>4</sub> O <sub>9</sub> 8.58 %	a= 7.6526 Å b =9.1057 Å c=5.5454 Å V = 386.415 Å <sup>3</sup>			χ <sup>2</sup> =1.441

The refinement corroborated that BHFO crystallizes in a orthorhombically distorted perovskite structure having Pnma space group and the extra peak in the XRD pattern belongs to Bi<sub>2</sub>Fe<sub>4</sub>O<sub>9</sub> impurity phase (see Fig. 4.3 and Table 4.1). Rietveld refinement was carried out for rhombohedral, tetragonal, triclinic, monoclinic and orthorhombic structure. The Goodness of Fit (GoF) of our sample with orthorhombic structure (space group -Pnma) and with a second phase Bi<sub>2</sub>Fe<sub>4</sub>O<sub>9</sub> (space group–Pbam) is found to be within 1.44 indicating the reliability of the refinement. Indeed, rare earth metal doped BFO crystallizes with orthorhombic structure.<sup>133,137</sup>

However, refinement indicates that Ho substituted BFO has different bond angles (Fe-O2-Fe =151.33° , Fe-O1-Fe= 147.91°) and bond lengths (Fe-O1=1.49 Å, Fe-O2=1.82 Å) compared

to that of undoped BFO. <sup>23</sup> The alternation of these parameters is expected to have profound influence on the magnetic and optical properties of BHFO.

However, looking at the XRD patterns for composite thin films (see Figs. 4.1 (b) to 4.1(d)) it can be immediately appreciated that intensity of the peaks of BHFO increases with an increase mol.% of BHFO nanoparticles. In particular, no impurity peak can be discerned in any of the composite films. This observation solidifies the notion that the anatase phase of TiO<sub>2</sub> is retained in the films and addition of nanoparticles does not introduce any phase changes. Another feature of the composite thin films to be observed is that the addition of BHFO has shifted the diffraction peaks of different planes of composite films and the lattice parameters have changed with respect to pure TiO<sub>2</sub> (see Table 4.2). The positions of diffraction peaks (101) and (200) were determined using Pseudo -Voight function in High Score Plus Software and lattice parameters were calculated using the following formulae <sup>139</sup>

$$\frac{1}{d_{hkl}^2} = [h^2 + k^2 + l^2 \left(\frac{a^2}{c^2}\right)] \frac{1}{a^2}$$

where  $d_{hkl}$  spacing has been calculated using the Bragg's law

Table 4.2. Position ( $2\theta$ ) and lattice parameters values obtained from XRD for pure film and composite films.

Compound	<i>Position</i> ( $2\theta$ ) <sub>(101)</sub>	<i>Position</i> ( $2\theta$ ) <sub>(200)</sub>	Lattice parameters	
			a=b (Å)	c (Å)
TiO <sub>2</sub>	25.2681	48.0128	3.7867	9.5092
T <sup>95</sup> B <sup>5</sup>	25.2907	48.0459	3.7843	9.4964
T <sup>90</sup> B <sup>10</sup>	25.2452	48.0097	3.7869	9.5136
T <sup>80</sup> B <sup>20</sup>	25.2485	47.9995	3.7877	9.5136

The peak shifting in composite films may be attributed to the diffusion of  $\text{Fe}^{3+}$ ,  $\text{Ho}^{3+}$  or  $\text{Bi}^{3+}$  ions into  $\text{TiO}_2$  across the interfaces of BHFO and  $\text{TiO}_2$ . Table 4.2 shows that diffraction peaks (101) and (200) have shifted to higher angle for  $\text{T}^{95}\text{B}^5$  and this film has the lowest lattice parameters. According to a previous study, this phenomenon manifests the introduction of tensile stresses due to the interstitial incorporation of doping ions in the crystal lattice of  $\text{TiO}_2$ .<sup>140</sup> Some other previous studies also report that Fe ions can go either in octahedral interstitial sites or in the substitutional positions of  $\text{TiO}_2$  lattice.<sup>141,142</sup> Since the ionic radii of  $\text{Fe}^{3+}$  (0.785 Å) is lower than that of  $\text{Bi}^{3+}$  (1.14 Å) and  $\text{Ho}^{3+}$  (1.015 Å),<sup>143</sup>  $\text{Fe}^{3+}$  ions have the highest chance of interstitial incorporation in  $\text{TiO}_2$ . On the other hand, the diffraction peaks of  $\text{T}^{90}\text{B}^{10}$  and  $\text{T}^{80}\text{B}^{20}$  has shifted to the lower angle and they have larger lattice parameters compared to the pure film (see Table 4.2). These can be ascribed to the generation of compressive stresses as a result of substitutional incorporation of  $\text{Bi}^{3+}$  (1.14 Å),  $\text{Ho}^{3+}$  (1.015 Å) or  $\text{Fe}^{3+}$  (0.785 Å).<sup>140,143</sup> The comparatively larger ionic radii of Bi, Ho and Fe compared to  $\text{Ti}^{4+}$  (0.745 Å) ion<sup>143</sup> possibly cause an expansion of the crystal lattice and concordant shift in the  $\text{TiO}_2$  diffraction peaks to a smaller angle. The substituted  $\text{Ti}^{4+}$  ions may have also diffused in crystal structure of BHFO.

## 4.2 Morphological And Elemental Analysis

Fig. 4.4 exhibits the surface images of nanoparticles and films annealed at 500 °C. The observed nanoparticles are nearly spherical in shape with average diameter of 45 nm as depicted in Fig. 4.4(a). It can be clearly seen from Fig. 4.4 (a) that nanoparticles are agglomerated and thus they were dispersed in an ultrasonic bath before composite thin film preparation. On the other side, the grains of pure  $\text{TiO}_2$  film are polygonal and crack-free (see Fig. 4.4(b)) signifying the fact that annealing and densification has occurred to a satisfactory degree. The average grain size of this film is larger than that of nanoparticles and is found to be 60 nm. The average diameter of nanoparticles and grain size of thin films were estimated using Image J software. The addition of only 5 mol.% BHFO in  $\text{TiO}_2$  has introduced crack as well as has diminished uniformity and polygonality of the grains. Upon closer inspections, small clusters of spherical BHFO nanoparticles are found to be distributed throughout the surface (encircled area in the Fig. 4.4(c)).

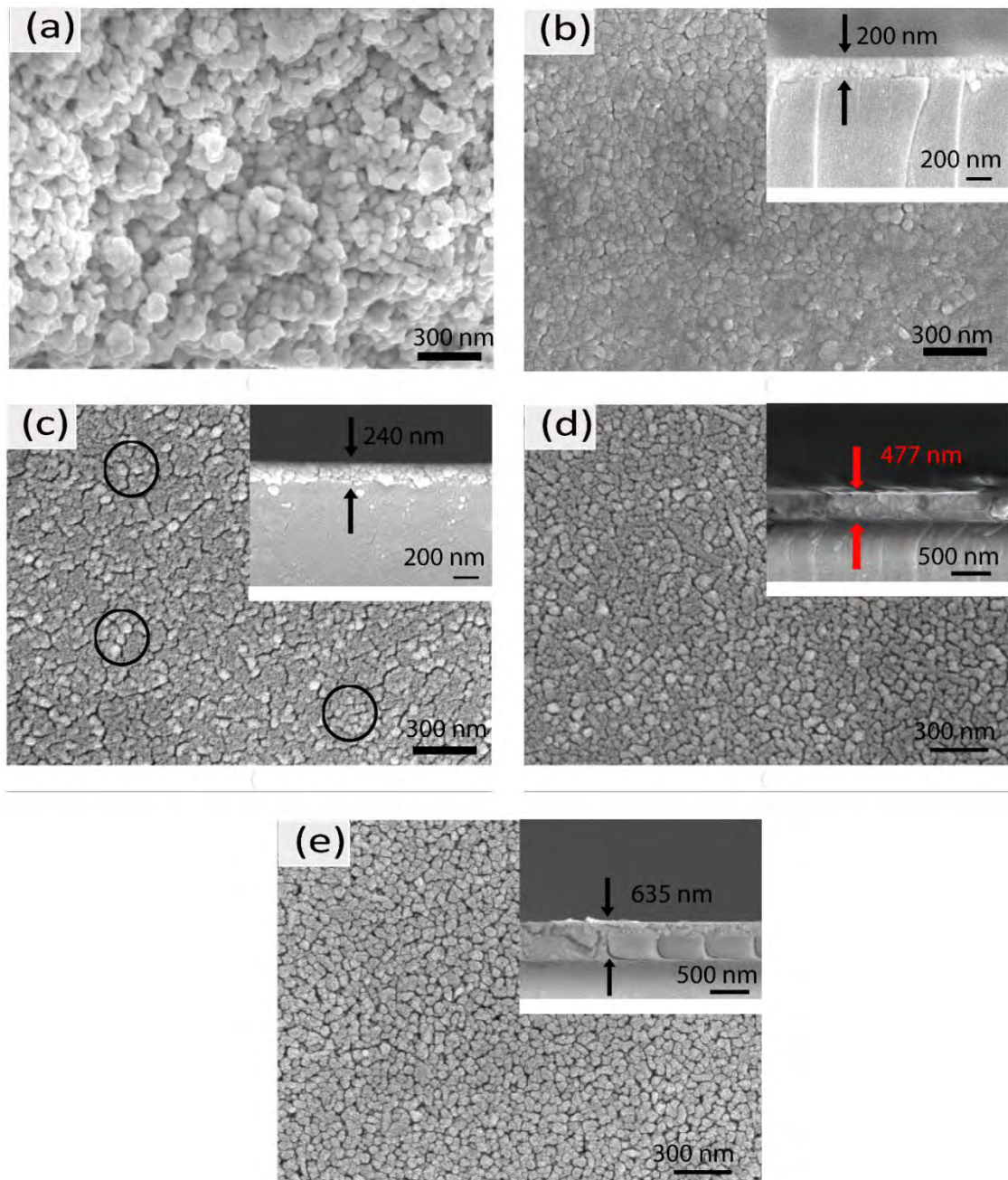


Fig. 4.4. FESEM images of (a) BHFO nanoparticles (b) TiO<sub>2</sub> film (c) T<sup>95</sup>B<sup>5</sup> film (d) T<sup>90</sup>B<sup>10</sup> film and (e) T<sup>80</sup>B<sup>20</sup> film along with the films' cross-section micrographs. The magnification for all the images is x50000.

Furthermore, in order to gain insight on spatial distribution of elements, EDS analysis and elemental mapping were performed on T<sup>95</sup>B<sup>5</sup> as shown in Fig. 4.5. Although the EDS spectrum

and elemental mappings in Figs. 4.5 (b–g) are exhibiting good homogeneous distribution of the elements (Ti (green), Bi (blue), Ho (pink), Fe (yellow), and O (red)), this homogeneous distribution could be attributed to large interaction volume produced during the EDS operation. An incident electron beam of 15 kV utilized during this operation was expected to penetrate a depth of 1 to 2  $\mu\text{m}$  into the film in all directions. Fig. 4.4 (c) clearly depicts that the distance between two consecutive clusters of BHFO is lower than 1  $\mu\text{m}$  and therefore a homogeneous distribution of elements is expected to be recorded by the detector of FESEM.

The addition of 10 and 20 mol. % BHFO nanoparticles has totally changed the morphology of thin films (see Fig. 4.4 (d) and (e)).  $\text{T}^{90}\text{B}^{10}$  and  $\text{T}^{80}\text{B}^{20}$  films have irregular polygonal grains and spherical nanoparticles which have made the surface rough. It has become difficult to identify  $\text{TiO}_2$  and BHFO nanoparticles separately from Fig. 4.4 (d) and (e). Indeed,  $\text{T}^{80}\text{B}^{20}$  with 20 mol.% BHFO has larger number of porosities, cracks and rougher surface compared to  $\text{T}^{90}\text{B}^{10}$ . The FESEM surface morphology of  $\text{T}^{80}\text{B}^{20}$  film is consistent with the peak intensities ( $2\theta = 22.54^\circ, 32.14^\circ, 39.48^\circ, 46.185^\circ$  and  $57.34^\circ$ ) of XRD pattern (as depicted in Fig. 4.1) implying high amount of BHFO nanoparticles in the  $\text{TiO}_2$  matrix. Moreover, the thickness of the films is increasing with increasing mol. % of BHFO nanoparticles. It can be seen from the insets of Fig. 4.4 (b) to (e), the average thicknesses of  $\text{TiO}_2$ ,  $\text{T}^{95}\text{B}^5$ ,  $\text{T}^{90}\text{B}^{10}$  and  $\text{T}^{80}\text{B}^{20}$  are 200, 244, 477, and 635 nm, respectively. The cross sections of the films also indicate the well-adherence of films with the glass substrate. Considering all these aforementioned observations it can be reasonably stated that there is no appreciable segregation of BHFO nanoparticles in the  $\text{TiO}_2$  matrix.



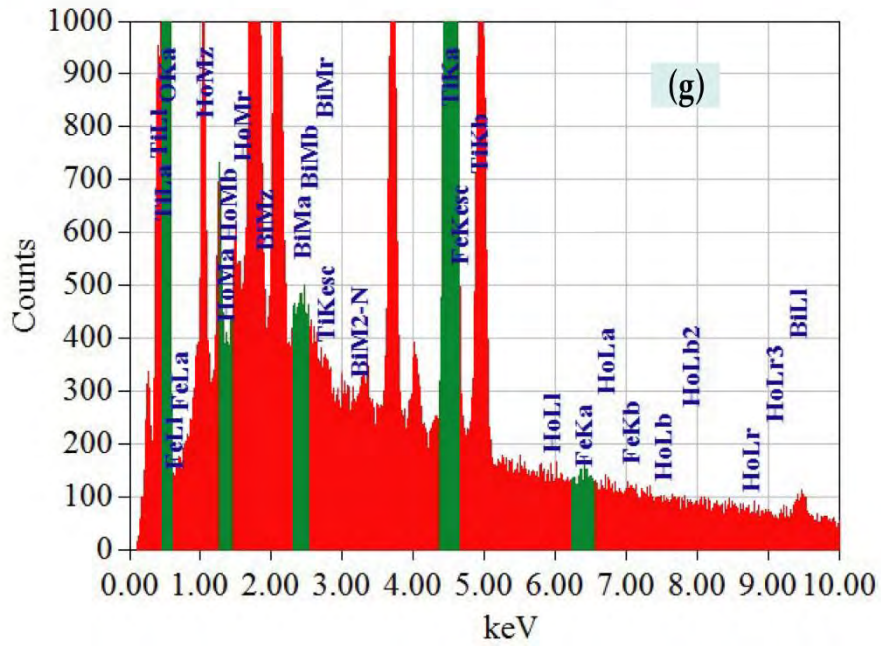
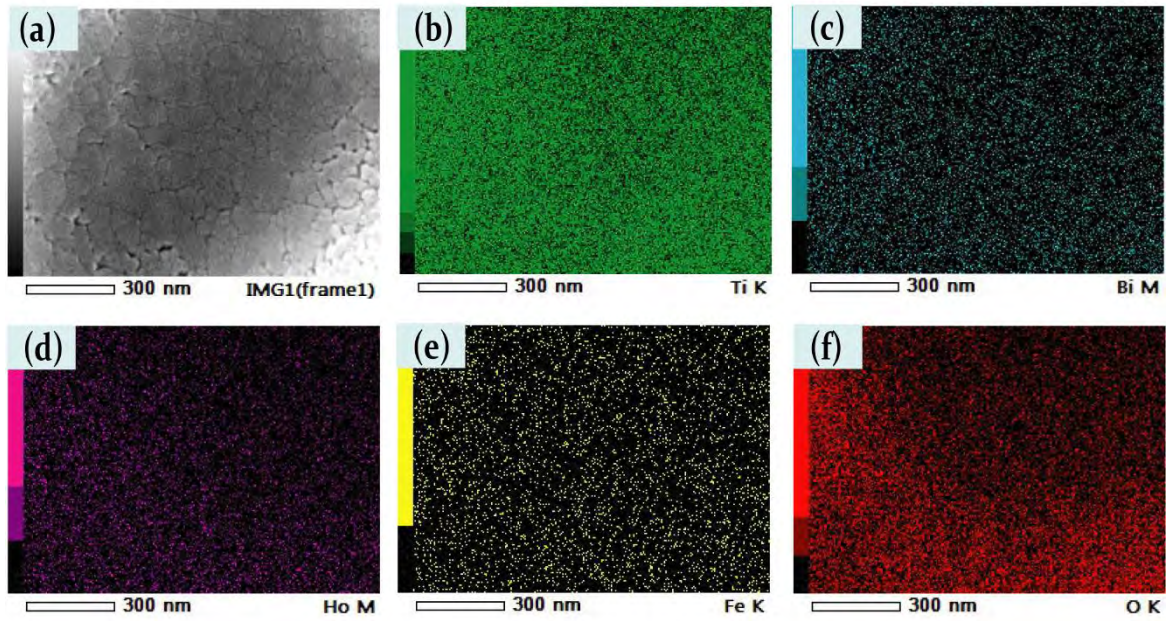


Fig. 4.5. Elemental mapping of (b) Ti (green), (c) Bi (blue), (d) Ho (pink), (e) Fe (yellow), and (f) O (red) taken from the selected area of the FESEM image of  $T^{95}B^5$  film as shown in (a). (g) EDS pattern with the composition of the elements for the film.

### 4.3 Optical Properties Study

Fig. 4. 6 depicts the absorbance spectra for thin films and nanoparticles. The absorbance of BHFO nanoparticles shown in the inset of Fig. 4.6 was obtained from diffused reflectance data using Kubelka-Munk conversion function.<sup>111</sup> The diffused reflectance data was converted to Kubelka-Munk function given by the following equation:

$$F(R) = \frac{(1 - R)^2}{2R}$$

where R is the diffused reflectance value. On the other hand the absorbance of the films was determined using Beer- Lambert law as follows:<sup>144,145</sup>

$$A = \log \frac{(1-R)^2}{T}$$

Where A, T and R stand for the absorbance, transmittance and reflectance of the film.

Nanoparticles exhibit extensive visible light absorbance and absorb larger wavelength than synthesized films. The steep shape of the spectrum indicates that the visible light absorption has happened as a result of electronic transition from the valence band to conduction band ( $O^{2-} 2p \rightarrow F^{3+} 3d$ ) in BHFO lattice.<sup>23</sup> This phenomenon will be discussed in detail in the following section. In contrast, the pure  $TiO_2$  film does not start absorbing substantially until the incident wavelength falls below 370 nm (see Fig. 4.6). This is typical behavior of  $TiO_2$  film.<sup>19</sup> It is noticeable from Fig. 4.6 that the absorption edge of composite thin films shows progressive shift between the pure  $TiO_2$  thin film and BHFO nanoparticles. The absorption edge of  $T^{95}B^5$  film does not shift much and still absorb shorter wavelength(  $\sim 380$  nm) than two other composite films. Fig. 4.6 clearly depicts that  $T^{90}B^{10}$  and  $T^{80}B^{20}$  films show a redshift and absorb visible light. The absorption edges of  $T^{90}B^{10}$  and  $T^{80}B^{20}$  films are 440 and 545 nm respectively (see Fig. 4.6). It has been established that the interfacial charge of  $TiO_2$  gets affected by diffusion of foreign ions which in turn influence the optical properties.<sup>146,147</sup> Indeed, the increment in lattice parameters of  $T^{90}B^{10}$  and  $T^{80}B^{20}$  films (see Table 4.2) suggest the possibility of  $Bi^{3+}$ ,  $Ho^{3+}$  and  $Fe^{3+}$  ions diffusion in the crystal structure of  $TiO_2$ . Therefore, the bathochromic shift of  $T^{90}B^{10}$  and  $T^{80}B^{20}$  films occurs probably due to the interdiffusion of  $Fe^{3+}$ ,  $Ho^{3+}$  or  $Bi^{3+} / Ti^{4+}$  ions across the interfaces of BHFO and  $TiO_2$ . In fact, due to interdiffusion of ions the electrons of these two films could be excited from the partially filled d orbitals of

$\text{Fe}^{3+}$  (rather than the lower-lying O p orbitals) to the Ti 3d orbitals with lower energy visible light.<sup>1</sup>

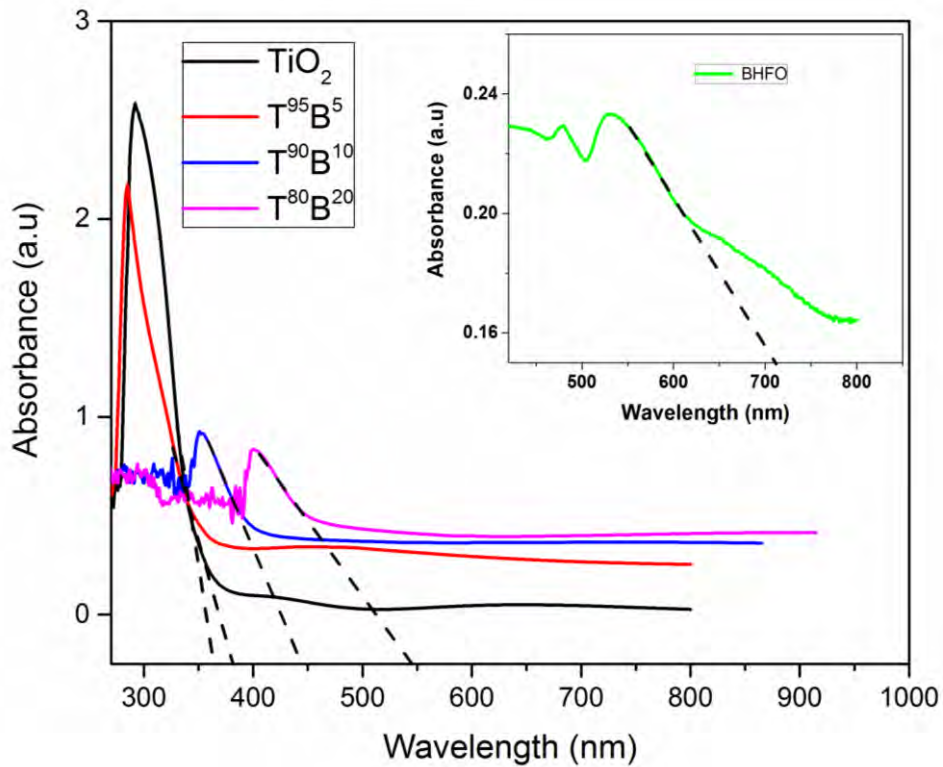


Fig. 4.6. UV-vis absorbance spectra of films. The inset shows the absorbance spectra of BHFO nanoparticles.

In order to have better ideas on the optical properties of the films, their band gaps were determined as shown in Fig. 4.7. The band gap of BHFO nanoparticles obtained from  $[E * F(R)]^2$  vs  $E$  plot depicted in Fig. 4.7 (a) is found to be 1.88eV, which is notably smaller than the previously reported values for both undoped<sup>148</sup> and many doped BFO.<sup>112</sup> The reduced band gap of BHFO could be attributed to the following reasons: (a)  $\text{Ho}^{3+}$  ions likely have minimal degree of hybridization for a stable electronic configuration ( $4f^{10} 5d^0 6s^0$ ) which in turn may lead to the formation of unique energy level in between Fe 3d and O 2p and thereby diminish the effective band gap of Ho doped BFO.

(b) According to some previous investigations, changes in Fe- O bond length and Fe-O-Fe bond angle by cation doping play a pivotal role in modifying one-electron bandwidth ( $W$ ) and thus band gap of BFO.<sup>23,114</sup> This claim has been substantiated by the empirical formula relating

W with bond length and angle:  $W \approx \frac{\cos\omega}{d_{Fe-O}^{3.5}}$ , where  $\omega$  stands for  $\frac{1}{2}[\pi - (\text{Fe-O-Fe})]$  and  $d_{Fe-O}$  is the Fe-O bond length.<sup>149</sup> The relationship between band gap and W can be given as:  $E_g = \Delta - W$  where  $\Delta$  is the charge transfer energy<sup>149</sup>.

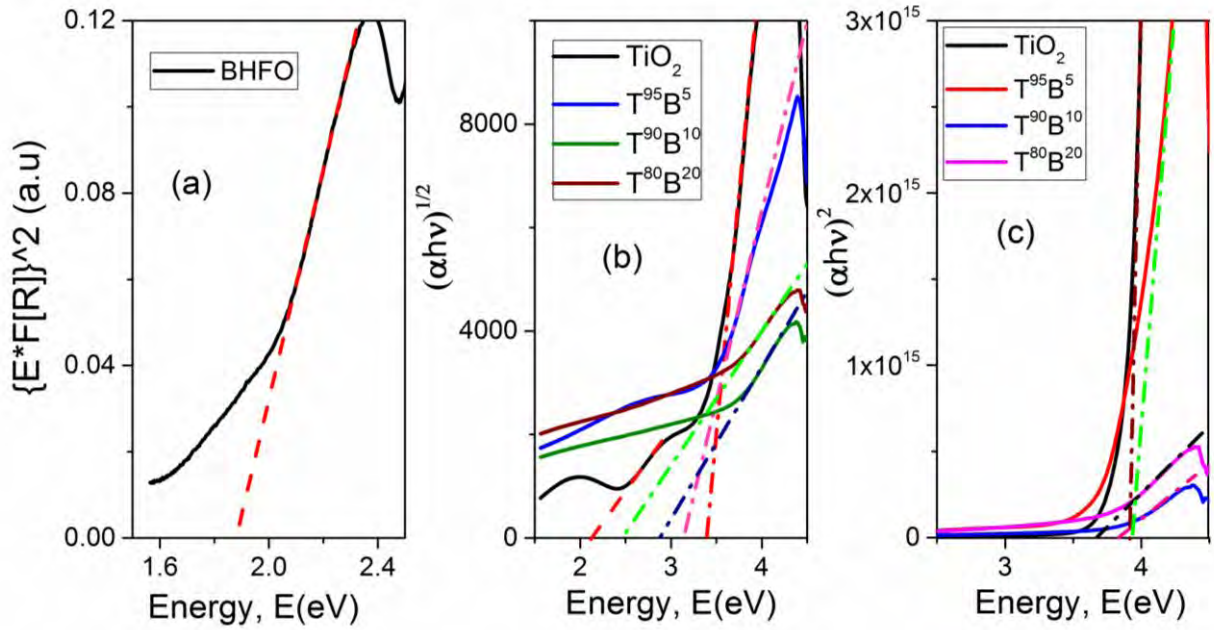


Fig. 4.7. (a)  $[E \cdot F(R)]^2$  vs energy, E plot to calculate band gap energy of nanoparticles (b) indirect and (c) direct Tauc's plots demonstrating the band gap energies of pure and composite thin films

Generally, BFO crystallizes in a rhombohedral phase and bond length (Fe-O) of this phase is greater than that of orthorhombic phase.<sup>23</sup> Since BHFO nanoparticles have orthorhombic phase and have smaller bond length, they have appreciably larger bandwidth (W) value than that of BFO which could reduce the effective band gap energy of BHFO.

The optical band gap of the films were calculated using the Tauc's law<sup>54</sup> as given below:

$$(\alpha h\nu) = A' (E - E_g)^n$$

where  $A'$  is a constant, E is the photon energy,  $E_g$  is the band gap energy,  $\alpha$  is absorption coefficient and n is the power factor of the optical transition mode in a semiconductor, i.e.,

direct transition ( $n=1/2$ ) or indirect transition ( $n=2$ ). The band gaps of the films were obtained by extrapolating the linear portion of  $(\alpha h\nu)^2$  vs E plot for direct transition (see Fig. 4.7 (c) ) and  $(\alpha h\nu)^{1/2}$  vs E plot for indirect transition (see Fig. 4.7 (b) ). Since the indirect band gaps of the films are more related to their absorption edge values (see Fig. 4.6) they have been assigned to the respective composite thin films. Even both experimental results and theoretical modeling suggest that TiO<sub>2</sub> has a direct forbidden gap, which is almost degenerated with an indirect allowed transition. Therefore, the indirect allowed transition dominates in the optical absorption just above the absorption edge due to the weak strength of the direct forbidden transition.<sup>150</sup>

The Tauc's plots of composite thin films corresponding to indirect transition shown in Fig. 4.7 have only one linear region. However, the curve for pure TiO<sub>2</sub> has more than one linear regions which indicates that there is more than one optical transition occurring in this film. The first transition of pure film occurred at 3.4 eV is its effective band gap which agrees reasonably well with previous studies.<sup>140,151</sup> The second indirect transition occurs at 2.1 eV and it is believed that this sort of transition is attributed to the presence of oxygen vacancies (OVs) in deposited TiO<sub>2</sub> film.<sup>19</sup>

The indirect band gaps of T<sup>95</sup>B<sup>5</sup>, T<sup>90</sup>B<sup>10</sup> and T<sup>80</sup>B<sup>20</sup> films are 3.13, 2.87 and 2.46 respectively (see Fig. 4.7). Thus, the optical transition energies of composites thin films monotonically decrease with increasing mol.% of BHFO nanoparticles. A perceptive explanation for the reduced band gap is related to conduction band of two different semiconductors. The hypothesis is that if the conduction band edge of the sensitizing material is higher than the conduction band edge of TiO<sub>2</sub>, electrons can transfer from the smaller band gap material to the conduction band of TiO<sub>2</sub>.<sup>18,19</sup> According to some previous reports, BFO has relatively high conduction band edge<sup>1,152</sup> which makes electrons in BFO nanoparticles to be transferred easily into the lower lying conduction band of TiO<sub>2</sub> through the interface. Thus it is required to determine the conduction band (CB) and valence band (VB) positions of both BHFO and TiO<sub>2</sub> to elucidate optical transition phenomenon. The CB potential of BHFO and TiO<sub>2</sub> at the point of zero charge can be calculated successfully by the following empirical equation.<sup>153,154</sup>

$$E_{CB} = \chi_s - E^e - 0.5E_g \quad (4.1)$$

where  $E_{CB}$  is the CB edge potential,  $E^e$  is the energy of free electrons on the hydrogen scale ( $\sim 4.5$  eV),  $E_g$  is the band gap energy of the semiconductor,  $\chi_S$  is the electronegativity of the semiconductor, which is the geometric mean of the electronegativity of the constituent atoms:

154

$$\chi_S = \sqrt[N]{\chi_1^a \chi_2^b \dots \chi_{n-1}^p \cdot \chi_n^q} \quad (4.2)$$

where  $\chi_n$ ,  $q$  and  $N$  are the electronegativity of the constituent atom, the number of species, and the total number of atoms in the compound, respectively. Herein the electronegativity of an atom is the arithmetic mean of the atomic electron affinity (EA) and the first ionization potential (FIP):

$$\chi_n = \frac{FIP + EA}{2}$$

Table 4.3. EA, FIP, and calculated electronegativity for several atoms.

Elements	FIP (eV)	EA (eV)	Electronegativity, ( $\chi_n$ ) (eV)
Ti	6.826	0.078	3.452
O	13.618	1.4614	7.539
Bi	7.285	0.945	4.115
Ho	6.018	0.518	3.268
Fe	7.87	0.162	4.016

Using Eq. (4.2) and Table 4.3, the electronegativity of  $\text{Bi}_{0.9}\text{Ho}_{0.1}\text{FeO}_3$ , can be calculated as:

$$\chi_{BHFO} = \sqrt[5]{(4.12)_{Bi}^{0.9} (3.268)_{Ho}^{0.1} (4.016)_{Fe}^1 (7.539)_O^3} = 5.86$$

Similarly the electronegativity of  $\text{TiO}_2$  is found to be 5.81.

Plugging  $E^e$ ,  $\chi_s$  values of  $\text{TiO}_2$  ( 5.81 eV) and BHFO (5.86 eV), and their corresponding  $E_g$  values into the Eq. 4.1,  $E_{CB}$  of  $\text{TiO}_2$  and BHFO stands as -0.39 and 0.42 eV respectively. The valence band edge potential  $E_{VB}$  can be obtained by the equation:  $E_{VB}=E_{CB}+E_g$  and the calculated  $E_{VB}$  of  $\text{TiO}_2$  and BHFO are 3.01 and 2.3 eV respectively. Figure 4.8 depicts the calculated energy levels of  $\text{TiO}_2$  and BHFO.

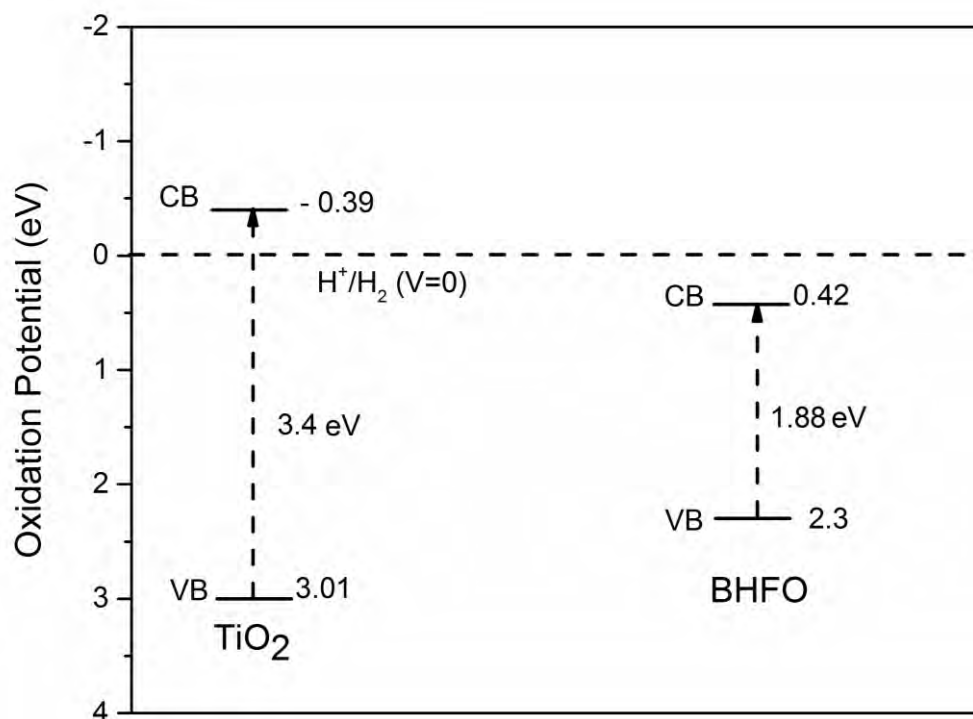
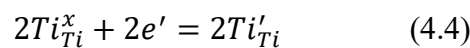
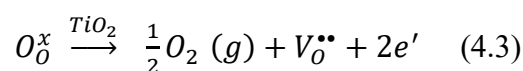


Fig. 4.8. Schematic illustration for the calculated energy level diagram indicating the conduction and valence band potentials of  $\text{TiO}_2$  film and BHFO nanoparticles.

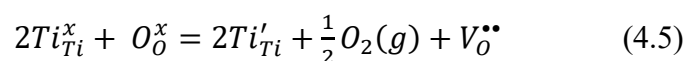
It can be clearly seen from Fig. 4.8 that BHFO has relatively higher CB potential than that of  $\text{TiO}_2$ . As discussed earlier, the redshift shown by  $\text{T}^{90}\text{B}^{10}$  and  $\text{T}^{80}\text{B}^{20}$  films is probably induced by Fe, Bi, Ho/Ti interdiffusion in the interfaces which could raise the CB edge potentials of BHFO and  $\text{TiO}_2$  and hence lower the optical transition energy at the interface between BHFO and  $\text{TiO}_2$ . Such reduced band-gaps of  $\text{T}^{90}\text{B}^{10}$  and  $\text{T}^{80}\text{B}^{20}$  could be beneficial for the efficient utilization of visible light for photocatalysis.

## 4.4 Electrical Properties Analysis

From the Hall effect analysis, the Hall coefficient is found to be negative for all the thin films which indicates that they are n- type semiconductors. Generally, TiO<sub>2</sub> is an intrinsic n-type semiconductor.<sup>8</sup> The formation of the OVs and titanium interstitials are responsible for this sort of conductivity.<sup>66</sup> TiO<sub>2</sub> is a sub-stoichiometric compound with excess titanium under standard conditions. This sub -stoichiometry is accommodated as OVs or titanium interstitials formation. The following reaction mechanisms can be considered for the formation of OVs in TiO<sub>2</sub> crystal<sup>67</sup>:



Combining Eq. (4.3) and Eq. (4.4)



The n-type conductivity behavior found in TiO<sub>2</sub> implies Eq. (4.5) to be the dominant step for providing two excess electrons. The carrier concentration (CC), resistivity and mobility of pure TiO<sub>2</sub> thin film deposited using non aqueous sol-gel method are found to be 2.0x10<sup>16</sup> cm<sup>-3</sup>, 1550.8 Ω-cm and 208 cm<sup>2</sup>/V.s respectively. The CC of TiO<sub>2</sub> found in the literatures ranges from 1x10<sup>16</sup> cm<sup>-3</sup> to 1x10<sup>20</sup> cm<sup>-3</sup>.<sup>68,69</sup> Thus the measured value of CC is within accepted range. The measured mobility of the film is also consistent with the previous study which reported almost similar CC.<sup>8</sup> The resistivity of conductor and semiconductor normally varies from 10<sup>3</sup> to 10<sup>8</sup> Ω -cm.<sup>70</sup> Based on this range, pure TiO<sub>2</sub> film can be classified as semiconductor. However, the resistivity of this pure TiO<sub>2</sub> film is lower than prepared by many methods such as chemical bath deposition,<sup>70</sup> spray pyrolysis<sup>155</sup> and DC magnetron sputtering technique.<sup>26</sup>



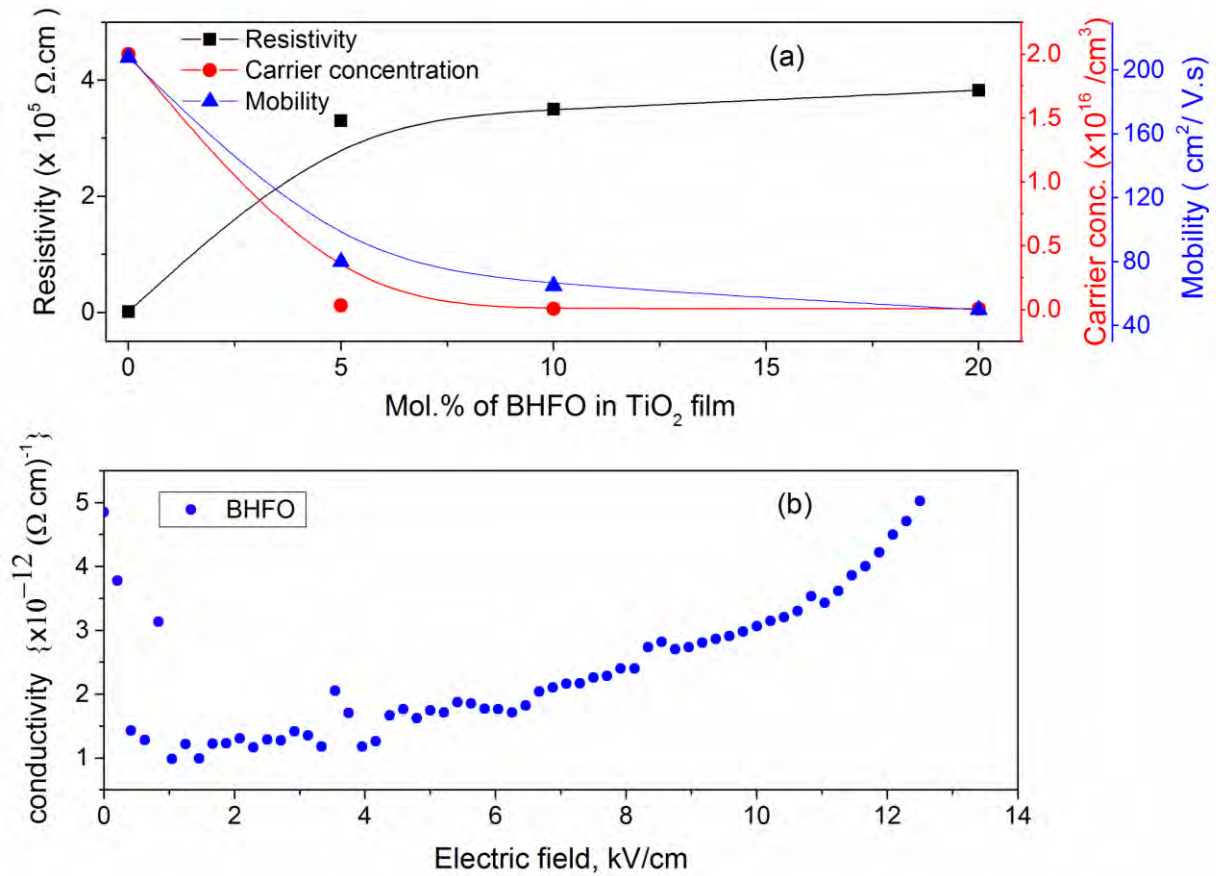


Fig. 4.9. (a) Resistivity, carrier concentration and mobility of films with different mol. % of BHFO (b) Conductivity ( $\Omega$ -cm) vs. Electric Field, E (kV/cm) plot of BHFO nanoparticles.

Fig. 4.9 (a) depicts that 5 mol.% BHFO addition has significantly altered the CC, mobility and resistivity of the film. The resistivity of  $T^{95}B^5$  film is  $\sim 2.33$  orders of magnitude higher than pure film while the CC and mobility of this film are 62.5 and 2.6 times lower than those of pure one. Moreover, the charge carriers of  $T^{95}B^5$  film are dominated by free electrons at 5 mol.% BHFO addition, even though, BFO is reported to be a p-type semiconductor where holes are the majority carriers. Here, substitution of  $Bi^{3+}$  with  $Ho^{3+}$  should retain BHFO as p-type semiconductor.<sup>156,157</sup> The determination of CC of BHFO was out of scope for the current study. Moreover, to the best of our knowledge there is no report on CC of BFO or on doped BFO.<sup>156,157</sup> The total CC of the composite film decreases with the addition of BHFO. An intuitive inception of this behavior can be related to OV's formation in BHFO and interstitial incorporation of Fe ions through BHFO/TiO<sub>2</sub> interface as mentioned earlier for  $T^{95}B^5$  film. Generally, Bi-vacancies and compensating OV's form in BFO and doped BFO during

annealing.<sup>24,158</sup> Hence, the possibility of these vacancies formation in BHFO cannot be ruled out during annealing of composite films. In such case, oxygen could leave BHFO lattice either as O<sub>2</sub> gas into the atmosphere or by migration as O<sup>2-</sup> ions from BHFO to TiO<sub>2</sub> due to OV gradient set up by the sub-stoichiometry of TiO<sub>2</sub> lattice as stated earlier. The creation of such positively charged OVs compensates the hole formation process in BHFO which in turns could reduce the overall concentration of hole. Moreover, the migration of O<sup>2-</sup> ions may fill up the vacancies of TiO<sub>2</sub> without hampering its concentration of electrons. The aforementioned phenomenon could be responsible for electrons as predominant charge carrier in T<sup>95</sup>B<sup>5</sup>. However, the concentration of electrons may be affected subtly by the diffused Fe ions. Since Fe ions have more than one valence states such as Fe<sup>2+</sup> or Fe<sup>3+</sup>,<sup>158</sup> some of diffused Fe<sup>3+</sup> may have changed into Fe<sup>2+</sup> by accepting free electrons of TiO<sub>2</sub> matrix and reduces total CC of T<sup>95</sup>B<sup>5</sup> slightly. To summarize 5 mol.% BHFO addition generates new interfacial area between TiO<sub>2</sub> and BHFO which allows O<sup>2-</sup> and Fe ions to migrate from BHFO into TiO<sub>2</sub> at their direct contact interfaces, reducing the overall hole concentration of BHFO substantially and electron concentration of TiO<sub>2</sub> to some extent.

The additions of 10 and 20 mol.% BHFO have not changed the electrical properties of T<sup>90</sup>B<sup>10</sup> and T<sup>80</sup>B<sup>20</sup> films (see Fig. 4. 9(a)) appreciably. The mobilities of T<sup>90</sup>B<sup>10</sup> and T<sup>80</sup>B<sup>20</sup> films have decreased by a factor of 1.23 and 1.6 respectively and the CCs of these two films have been reduced by a factor of ~ 4 .1 when compared to those of T<sup>95</sup>B<sup>5</sup> film. Similarly, the resistivities of T<sup>90</sup>B<sup>10</sup> and T<sup>80</sup>B<sup>20</sup> films are 1.05 and 1.15 times higher than that of T<sup>95</sup>B<sup>5</sup> film. However, the charge carriers of T<sup>90</sup>B<sup>10</sup> and T<sup>80</sup>B<sup>20</sup> films are still found to be dominated by free electrons. The aforestated variations in CC, mobility and resistivity point out that addition of higher mol. % of BHFO has little effect on electrical properties of composite films. The trivial reduction of CC in T<sup>90</sup>B<sup>10</sup> and T<sup>80</sup>B<sup>20</sup> films depends on diffused Ho<sup>3+</sup>, Fe<sup>3+</sup> and Bi<sup>3+</sup> ions which substitute Ti<sup>4+</sup> from the lattice sites of TiO<sub>2</sub> as discussed in XRD pattern analysis section. This substitution may lead to formation of holes compensating free electrons in TiO<sub>2</sub> and eventually reduces films' electron concentration. However, further reduction of CC is probably hindered by intergranular cracks and pores formation in films (see Fig. 4.4 (d) and (e) ) as well as the direct contact interface areas between BHFO and TiO<sub>2</sub>, which are likely to become gradually saturated at higher BHFO nanoparticles content (10 and 20 mol.%) in the composite films. These phenomena could hamper further enhancement in migration of O<sup>2-</sup>, Ho<sup>3+</sup>, Fe<sup>3+</sup> from BHFO to

TiO<sub>2</sub> in T<sup>90</sup>B<sup>10</sup> and T<sup>80</sup>B<sup>20</sup> restricting any marked alteration in overall carrier concentration of the system.

The increased resistivity of composite thin films is directly related to low conductivity of BHFO (see Fig. 4.9 (b)). The conductivity of BHFO varies from 1x 10<sup>-12</sup> to 5 x10<sup>-12</sup> (Ω. cm)<sup>-1</sup> which is lower than that of previously reported doped BFO.<sup>23</sup> The CC and mobility are also related to resistivity via the following equation:<sup>159</sup>

$$\rho = \frac{1}{qn\mu}$$

where q is the electron charge, n is carrier concentration and μ is the mobility. The reduced CC and mobility of composite films could be ascribed to increased resistivity of films. Moreover, the poor morphology of the films may reduce mobility of films. Yasuno et al.<sup>160</sup> and Trinh et al.<sup>161</sup> observed that electrical properties of the film depend on surface roughness and porosity of film. These surface roughness and porosity increase the scattering of electrons and holes which in turn reduce their mean free path. From FESEM images it is clear that the pure film has a smoother surface than the composite films. With increasing mol.% of BHFO, the surface roughness and porosity of the films increase and charge carrier mean free path of the films decreases. Thus, the mobilities of films are decreasing with reduced mean path of electron. The composite films with enhanced resistivity, and reduced CC and mobility will have minimum leakage current and reduced power losses in devices. Therefore, these films could be electrically reliable for resistors, sensors and memory devices.

## 4.5 Magnetic Properties Study

Generally BFO nanoparticles exhibit G-type antiferromagnetism due to its cycloid spiral spin structure.<sup>23</sup> However, an enhancement in magnetization by Ho-doping at Bi-site is evidenced in this study ( see Fig. 4.10 (a) ). The saturation magnetization (M<sub>s</sub>), coercivity (H<sub>c</sub>) and magnetic susceptibility (χ<sub>M</sub>) of BHFO nanoparticles are 24.33 emu/cm<sup>3</sup>, 260 Oe and 0.247 respectively. The density of BHFO is 8.40 g/cm<sup>3</sup> which was calculated from unit cell parameters listed in Table 4.1. The magnetization unit of BHFO was converted from emu/gm to emu/cm<sup>3</sup> by multiplying with 8.40 g/cm<sup>3</sup>. The bond lengths and bond angles of BHFO listed

in Table 4.1 are quite different from the reported bond lengths and bond angles of pure BFO.<sup>23</sup> The enhanced magnetization could be attributed to these changes in bond angle and bond length which modify the tilting angle of FeO<sub>6</sub> octahedron and thereby suppress spiral modulated spin structure.<sup>23</sup> Moreover, the substitution of non-magnetic Bi<sup>3+</sup> ([Xe] 4f<sup>14</sup> 5d<sup>10</sup> 6s<sup>2</sup> 6p<sup>0</sup>) with magnetic Ho<sup>3+</sup> ([Xe] 4f<sup>10</sup>) having high magnetic moment (10.6 μ<sub>B</sub>) could lead to improved magnetization.

Room temperature M-H curve of thin films were obtained after subtracting the contribution of glass substrate. TiO<sub>2</sub> film deposited on this substrate is diamagnetic (see Fig. 4.10 (b)) and the diamagnetic susceptibility ( $\chi_D'$ ) is  $\sim -1.58 \times 10^{-03}$ . Donor type defects (e.g. OVs) have been proposed to be a vital element for ferromagnetism in TiO<sub>2</sub><sup>162,163</sup> indicating that synthesized TiO<sub>2</sub> film may not have sufficient amount of OVs to induce magnetism. The other three composite thin films show no such diamagnetic behavior yet they display no complete ferromagnetic loop either. The composite thin films have ferromagnetic behavior accompanied with a diamagnetic component. The discernably open hysteretic loop shown in the inset of Fig. 4.10 (b) is signifying the presence of a ferromagnetic component. The actual saturation magnetization of all the composite thin films likely occurs at low magnetic field and all the films have diamagnetic components at higher magnetic field. Fig. 4.10 (b) clearly depicts that saturation magnetization of films is increasing with increasing mol.% of BHFO. T<sup>80</sup>B<sup>20</sup> has higher magnetization and coercivity than two other composite films (see inset of Fig. 4.10 (b)). Moreover, it has retained its ferromagnetism upto 11 kOe and has the lowest diamagnetic susceptibility ( $-3.28 \times 10^{-4}$ ). The diamagnetic susceptibilities of other two films are  $-1.01 \times 10^{-03}$  (T<sup>95</sup>B<sup>5</sup>) and  $-6.045 \times 10^{-4}$  (T<sup>90</sup>B<sup>10</sup>).

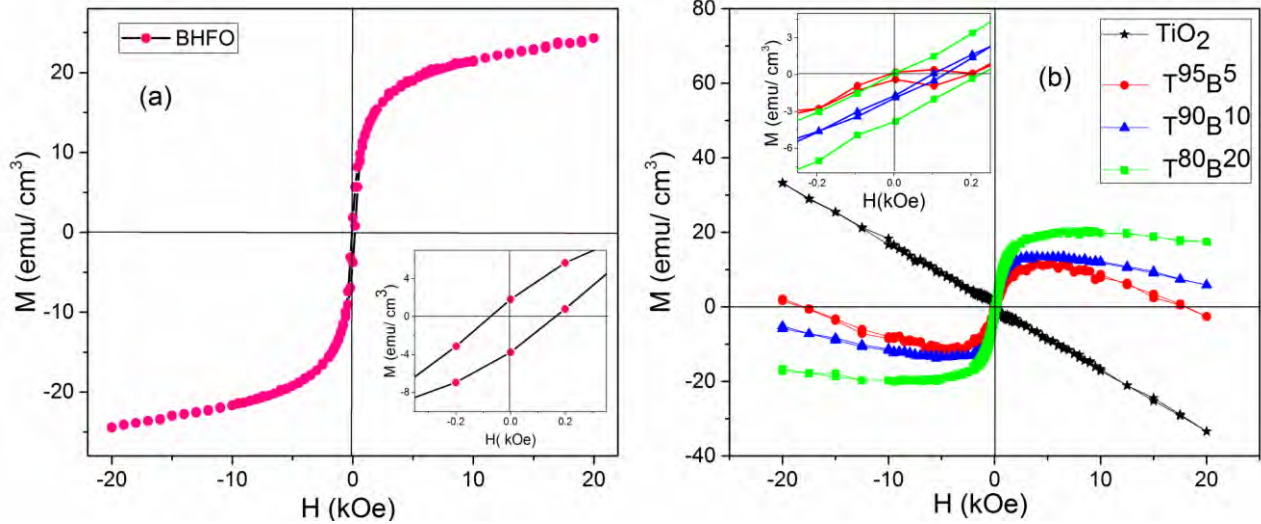


Fig. 4.10. Room temperature (a) M-H hysteresis loop for BHFO nanoparticles with inset showing its magnified M-H loop (b) M-H hysteresis loops for pure and composite films with inset showing magnified M-H loops of T<sup>95</sup>B<sup>5</sup>, T<sup>90</sup>B<sup>10</sup> and T<sup>80</sup>B<sup>20</sup> films.

Previous investigations reveal that diffusion of magnetic ions into an oxide ceramic through interfaces aids in emergence of room temperature ferromagnetism.<sup>61,164</sup> As conferred earlier, the interdiffusion of Fe<sup>3+</sup>, Ho<sup>3+</sup> and Bi<sup>3+</sup> in the interfaces could bring about a change in the crystal structure of TiO<sub>2</sub>. The ferromagnetic exchange between the diffused magnetic ions (Fe<sup>3+</sup> or Ho<sup>3+</sup>) and OVs could induce magnetism.<sup>61,165</sup> As discussed in electrical section, only 5 mol.% BHFO incorporation in TiO<sub>2</sub> appreciably decreases existing OVs and further addition of BHFO may not have any marked influence on the amount of OVs. The lacking of sufficient OVs to couple with the magnetic ions possibly leads to diamagnetism at higher magnetic field. Since T<sup>95</sup>B<sup>5</sup> and T<sup>90</sup>B<sup>10</sup> have lower mol.% of BHFO compared to T<sup>80</sup>B<sup>20</sup>, they are expected to have smaller amount of diffused Fe<sup>3+</sup> or Ho<sup>3+</sup> ions in TiO<sub>2</sub> phase than that of T<sup>80</sup>B<sup>20</sup>. Therefore, the ferromagnetic exchange of T<sup>95</sup>B<sup>5</sup> and T<sup>90</sup>B<sup>10</sup> is weak due to small amount of diffused magnetic ions and insufficient OVs, and thus diamagnetic susceptibility of these films is higher than that of T<sup>80</sup>B<sup>20</sup>. On the other hand, T<sup>80</sup>B<sup>20</sup> film has higher amount of magnetic ions when compared with other two composite films. Hence, a stronger ferromagnetic exchange between magnetic ions and insufficient OVs is expected in T<sup>80</sup>B<sup>20</sup> film leading to a lower diamagnetic susceptibility compared to the other two composite films. Indeed, composites thin film with further addition of BHFO nanoparticles (>20 mol.%) will have dominant diamagnetic component. It can be seen from Fig. 4.11 that the reduction in diamagnetic susceptibility from

TiO<sub>2</sub> film to T<sup>95</sup>B<sup>5</sup> film is prominent but further addition of BHFO nanoparticles does not bring such kind of change.

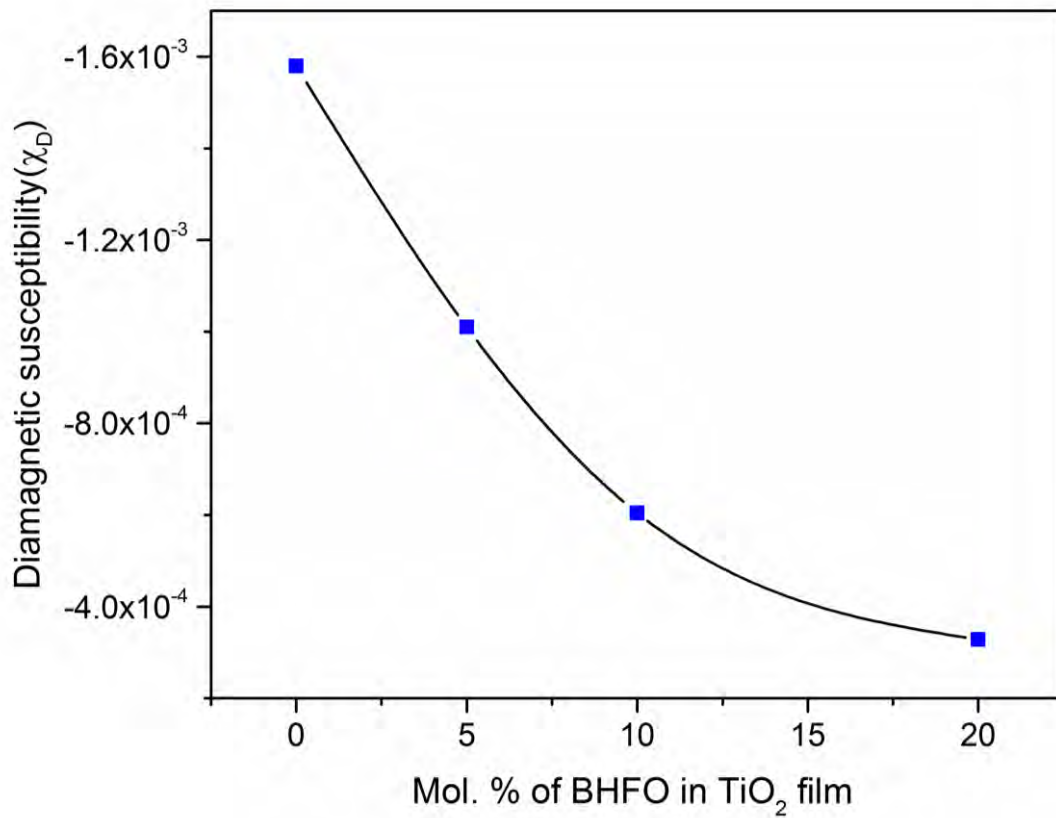


Fig. 4.11. Diamagnetic susceptibility of films with different mol. % of BHFO nanoparticles

In fact Fig. 4.11 depicts that diamagnetic susceptibility of T<sup>80</sup>B<sup>20</sup> film is approaching saturation phenomenon conforming our explanation provided in electrical section. The presence of pores and cracks in films ( see Fig. 4.4 (d) and (e) ) as well as possible saturation of total amount of direct contact interface areas between BHFO and TiO<sub>2</sub> not only affect the electrical properties but also the magnetic properties of T<sup>90</sup>B<sup>10</sup> and T<sup>80</sup>B<sup>20</sup> films. Nevertheless, this finding suggests that incorporation of BHFO nanoparticles into TiO<sub>2</sub> matrix introduces magnetism in final product which can be applied to thin films-based spintronics application.

# 5 CONCLUSION

The current study can be summarized as follows:

1. To the best of our knowledge TiO<sub>2</sub>-BHFO composite thin films were prepared for the first time by non-aqueous sol-gel method.
2. The incorporation of BHFO nanoparticles improves magnetism and electrical properties of composite thin films, and also reduces their band gaps.
3. Phase analysis by X-ray diffraction confirms that TiO<sub>2</sub> and BHFO retain anatase and orthorhombic (Pnma) phase respectively in composite thin films.
4. Field emission scanning electron microscopy (FESEM) depicts that pores, crack and surface roughness of the films increase with increasing mol.% of BHFO. Energy dispersive spectroscopy (EDS) reveals the homogeneous distribution of BHFO nanoparticles on TiO<sub>2</sub> matrices.
5. The composite thin films exhibit a redshift in optical absorption edge and absorb visible light. Thin films containing 20 mol. % BHFO nanoparticles exhibit a stronger absorption in visible region and indirect band gap of TiO<sub>2</sub> ( 3.4 eV) is significantly reduced to 2.46 eV. This behavior has been attributed to interdiffusion of Fe<sup>3+</sup>, Ho<sup>3+</sup>, Bi<sup>3+</sup> O<sup>2-</sup>/ Ti<sup>4+</sup> ions through the interfaces between BHFO and TiO<sub>2</sub>. Such reduced band-gaps of films could be beneficial for the efficient utilization of visible light for photocatalysis.
6. Hall measurements affirms that composite thin films have semiconducting behavior with n type carriers and the resistivity increased by ~ 2 orders of magnitude at 5 mol% BHFO nanoparticle addition. The CC and mobility of this film are 62.5 and 2.6 times lower than those of pure one The additions of 10 and 20 mol.% BHFO have not changed the electrical properties of films appreciably. The direct contact areas between BHFO and TiO<sub>2</sub> in composite films control the migration of these ions through their interfaces which eventually determines the CC of the films. The composite films with enhanced resistivity, and reduced CC and mobility will have minimum leakage current and



reduced power losses in devices. Therefore, these films could be electrically reliable for resistors, sensors and memory devices.

7. Moreover, while the pure thin film exhibits diamagnetism, composite thin films have both larger ferromagnetic and smaller diamagnetic components. The diamagnetic susceptibility of composite films decreases 4.81 times compared to pure one at 20 mol.% BHFO addition. The ferromagnetic exchange between the diffused magnetic ions ( $\text{Fe}^{3+}$  or  $\text{Ho}^{3+}$ ) and OVs has been considered to influence the induction of magnetism in composite thin films. This finding suggests that incorporation of BHFO nanoparticles into  $\text{TiO}_2$  matrix introduces magnetism in final product which can be applied to thin films-based spintronics application.

# **6 SUGGESTION FOR FUTURE WORK**

TiO<sub>2</sub>-BHFO composite thin films have opened many dimensions for future works. Some of them are listed below:

- Synthesis of TiO<sub>2</sub>-BHFO composite thin film using different techniques such as chemical bath deposition method, aqueous sol-gel method or spray pyrolysis method.
- The interdiffusion of Bi<sup>3+</sup>, Ho<sup>3+</sup>, Fe<sup>3+</sup> /Ti<sup>4+</sup> through the interface of BHFO/ TiO<sub>2</sub> control the magnetic, optical and electrical properties. A complete description of the interdiffusion mechanism of ions in the interface requires more intensive research.
- Fabrication of crack and pore free thin film to enhance magnetic and electrical properties.
- Commercialization of the non-aqueous sol-gel synthesis technique.
- The efficiency of TiO<sub>2</sub>-BHFO as photocatalyst can be found out by monitoring the degradation of organic pollutants such as dyes, detergents and pesticides etc.
- Fabricating resistors and memory devices using the developed material on availability of the device fabrication lab equipments.

## REFERENCE

- 1 Li, S., Lin, Y.-H., Zhang, B.-P., Li, J.-F. & Nan, C.-W. BiFeO<sub>3</sub>/TiO<sub>2</sub> core-shell structured nanocomposites as visible-active photocatalysts and their optical response mechanism. *Journal of Applied Physics* **105**, 054310 (2009).
- 2 Wang, X., Li, J.-G., Kamiyama, H., Moriyoshi, Y. & Ishigaki, T. Wavelength-sensitive photocatalytic degradation of methyl orange in aqueous suspension over iron (III)-doped TiO<sub>2</sub> nanopowders under UV and visible light irradiation. *The Journal of Physical Chemistry B* **110**, 6804-6809 (2006).
- 3 Nkosi, S. et al. An instant photo-excited electrons relaxation on the photo-degradation properties of TiO<sub>2-x</sub> films. *Journal of Photochemistry and Photobiology A: Chemistry* **293**, 72-80 (2014).
- 4 Serpone, N., Lawless, D., Disdier, J. & Herrmann, J.-M. Spectroscopic, photoconductivity, and photocatalytic studies of TiO<sub>2</sub> colloids: naked and with the lattice doped with Cr<sup>3+</sup>, Fe<sup>3+</sup>, and V<sup>5+</sup> cations. *Langmuir* **10**, 643-652 (1994).
- 5 Weissmann, M. & Errico, L. A. The role of vacancies, impurities and crystal structure in the magnetic properties of TiO<sub>2</sub>. *Physica B: Condensed Matter* **398**, 179-183 (2007).
- 6 Gale, E. TiO<sub>2</sub>-based memristors and ReRAM: materials, mechanisms and models (a review). *Semiconductor Science and Technology* **29**, 104004 (2014).
- 7 Wang, Z. et al. Extraordinary Hall effect and ferromagnetism in Fe-doped reduced rutile. *Applied Physics Letters* **83**, 518-520 (2003).
- 8 Li, X. et al. Structures and magnetic properties of p-type Mn: TiO<sub>2</sub> dilute magnetic semiconductor thin films. *Journal of Applied Physics* **106**, 043913 (2009).
- 9 Chen, X. & Burda, C. The electronic origin of the visible-light absorption properties of C-, N- and S-doped TiO<sub>2</sub> nanomaterials. *Journal of the American Chemical Society* **130**, 5018-5019 (2008).
- 10 Kim, Y. J. et al. Growth and properties of molecular beam epitaxially grown ferromagnetic Fe-doped TiO<sub>2</sub> rutile films on TiO<sub>2</sub> (110). *Applied physics letters* **84**, 3531-3533 (2004).
- 11 Kim, J.-Y. et al. Ferromagnetism Induced by Clustered Co in Co-Doped Anatase TiO<sub>2</sub> Thin Films. *Physical review letters* **90**, 017401 (2003).
- 12 Gao, X., Liu, X., Zhu, Z., Wang, X. & Xie, Z. Enhanced photoelectrochemical and photocatalytic behaviors of MFe<sub>2</sub>O<sub>4</sub> (M= Ni, Co, Zn and Sr) modified TiO<sub>2</sub> nanorod arrays. *Scientific reports* **6**, 30543 (2016).
- 13 Van Suchtelen, J. Product properties: a new application of composite materials. *Philips Res. Rep* **27**, 28-37 (1972).

- 14 Watson, S., Beydoun, D. & Amal, R. Synthesis of a novel magnetic photocatalyst by direct deposition of nanosized TiO<sub>2</sub> crystals onto a magnetic core. *Journal of Photochemistry and Photobiology A: Chemistry* **148**, 303-313 (2002).
- 15 Huang, W., Tang, X., Felner, I., Koltypin, Y. & Gedanken, A. Preparation and characterization of Fe<sub>x</sub>O<sub>y</sub>-TiO<sub>2</sub> via sonochemical synthesis. *Materials research bulletin* **37**, 1721-1735 (2002).
- 16 Cheng, C. et al. Enhanced photocatalytic performance of TiO<sub>2</sub>-ZnO hybrid nanostructures. *Scientific reports* **4**, 4181 (2014).
- 17 Mu, J. et al. Enhancement of the visible-light photocatalytic activity of In<sub>2</sub>O<sub>3</sub>-TiO<sub>2</sub> nanofiber heteroarchitectures. *ACS applied materials & interfaces* **4**, 424-430 (2011).
- 18 Yang, Y. et al. Electrospun nanofibers of p-type BiFeO<sub>3</sub>/n-type TiO<sub>2</sub> hetero-junctions with enhanced visible-light photocatalytic activity. *RSC Advances* **4**, 31941-31947 (2014).
- 19 Larsen, G. K., Fitzmorris, B. C., Longo, C., Zhang, J. Z. & Zhao, Y. Nanostructured homogenous CdSe-TiO<sub>2</sub> composite visible light photoanodes fabricated by oblique angle codeposition. *Journal of Materials Chemistry* **22**, 14205-14218 (2012).
- 20 Zhang, Y., Schultz, A. M., Salvador, P. A. & Rohrer, G. S. Spatially selective visible light photocatalytic activity of TiO<sub>2</sub>/BiFeO<sub>3</sub> heterostructures. *Journal of Materials Chemistry* **21**, 4168-4174 (2011).
- 21 Zhu, A., Zhao, Q., Li, X. & Shi, Y. BiFeO<sub>3</sub>/TiO<sub>2</sub> nanotube arrays composite electrode: construction, characterization, and enhanced photoelectrochemical properties. *ACS applied materials & interfaces* **6**, 671-679 (2013).
- 22 Sarkar, A., Singh, A. K., Sarkar, D., Khan, G. G. & Mandal, K. Three-dimensional nanoarchitecture of BiFeO<sub>3</sub> anchored TiO<sub>2</sub> nanotube arrays for electrochemical energy storage and solar energy conversion. *ACS Sustainable Chemistry & Engineering* **3**, 2254-2263 (2015).
- 23 Hasan, M. et al. Saturation magnetization and band gap tuning in BiFeO<sub>3</sub> nanoparticles via co-substitution of Gd and Mn. *Journal of Alloys and Compounds* **687**, 701-706 (2016).
- 24 Sakar, M., Balakumar, S., Saravanan, P. & Jaisankar, S. Annealing temperature mediated physical properties of bismuth ferrite (BiFeO<sub>3</sub>) nanostructures synthesized by a novel wet chemical method. *Materials Research Bulletin* **48**, 2878-2885 (2013).
- 25 Song, G. et al. Crystal structure refinement, ferroelectric and ferromagnetic properties of Ho<sup>3+</sup> modified BiFeO<sub>3</sub> multiferroic material. *Journal of Alloys and Compounds* **696**, 503-509 (2017).
- 26 Yildiz, A., Lisesivdin, S., Kasap, M. & Mardare, D. Electrical properties of TiO<sub>2</sub> thin films. *Journal of Non-Crystalline Solids* **354**, 4944-4947 (2008).

- 27 Hong, N. H., Sakai, J., Poirot, N. & Brizé, V. Room-temperature ferromagnetism observed in undoped semiconducting and insulating oxide thin films. *Physical Review B* **73**, 132404 (2006).
- 28 Vayssieres, L. *On solar hydrogen and nanotechnology*. (John Wiley & Sons, 2010).
- 29 Deng, Q. *Band gap tuning and structural engineering of TiO<sub>2</sub> for photocatalysis and solar cells*, University of Bolton, (2012).
- 30 Alireza, K. & Ali, M. G. *Nanostructured titanium dioxide materials: Properties, preparation and applications*. (World scientific, 2011).
- 31 Kitano, M., Matsuoka, M., Ueshima, M. & Anpo, M. Recent developments in titanium oxide-based photocatalysts. *Applied Catalysis A: General* **325**, 1-14 (2007).
- 32 Carp, O., Huisman, C. L. & Reller, A. Photoinduced reactivity of titanium dioxide. *Progress in solid state chemistry* **32**, 33-177 (2004).
- 33 Takeuchi, M. et al. Photocatalytic decomposition of NO under visible light irradiation on the Cr-ion-implanted TiO<sub>2</sub> thin film photocatalyst. *Catalysis Letters* **67**, 135-137 (2000).
- 34 Devi, L. G., Kumar, S. G., Murthy, B. N. & Kottam, N. Influence of Mn<sup>2+</sup> and Mo<sup>6+</sup> dopants on the phase transformations of TiO<sub>2</sub> lattice and its photocatalytic activity under solar illumination. *Catalysis Communications* **10**, 794-798 (2009).
- 35 Wang, M. C., Lin, H. J. & Yang, T. S. Characteristics and optical properties of iron ion (Fe<sup>3+</sup>)-doped titanium oxide thin films prepared by a sol-gel spin coating. *Journal of Alloys and Compounds* **473**, 394-400 (2009).
- 36 Barakat, M., Schaeffer, H., Hayes, G. & Ismat-Shah, S. Photocatalytic degradation of 2-chlorophenol by Co-doped TiO<sub>2</sub> nanoparticles. *Applied Catalysis B: Environmental* **57**, 23-30 (2005).
- 37 Yu, H., Li, X.-J., Zheng, S.-J. & Xu, W. Photocatalytic activity of TiO<sub>2</sub> thin film non-uniformly doped by Ni. *Materials chemistry and physics* **97**, 59-63 (2006).
- 38 Colon, G., Maicu, M., Hidalgo, M. s. & Navio, J. Cu-doped TiO<sub>2</sub> systems with improved photocatalytic activity. *Applied Catalysis B: Environmental* **67**, 41-51 (2006).
- 39 Liang, B., Mianxin, S., Tianliang, Z., Xiaoyong, Z. & Qingqing, D. Band gap calculation and photocatalytic activity of rare earths doped rutile TiO<sub>2</sub>. *Journal of rare earths* **27**, 461-468 (2009).
- 40 Zhang, Y., Zhang, H., Xu, Y. & Wang, Y. Significant effect of lanthanide doping on the texture and properties of nanocrystalline mesoporous TiO<sub>2</sub>. *Journal of Solid State Chemistry* **177**, 3490-3498 (2004).

- 41 Xu, A.-W., Gao, Y. & Liu, H.-Q. The preparation, characterization, and their photocatalytic activities of rare-earth-doped TiO<sub>2</sub> nanoparticles. *Journal of Catalysis* **207**, 151-157 (2002).
- 42 Li, G., Liu, C. & Liu, Y. Different effects of cerium ions doping on properties of anatase and rutile TiO<sub>2</sub>. *Applied Surface Science* **253**, 2481-2486 (2006).
- 43 Xiao, Q., Si, Z., Zhang, J., Xiao, C. & Tan, X. Photoinduced hydroxyl radical and photocatalytic activity of samarium-doped TiO<sub>2</sub> nanocrystalline. *Journal of Hazardous Materials* **150**, 62-67 (2008).
- 44 Zhang, C. et al. Charge recombination and band-edge shift in the dye-sensitized Mg<sup>2+</sup>-doped TiO<sub>2</sub> solar cells. *The Journal of Physical Chemistry C* **115**, 16418-16424 (2011).
- 45 Kumaresan, L., Mahalakshmi, M., Palanichamy, M. & Murugesan, V. Synthesis, characterization, and photocatalytic activity of Sr<sup>2+</sup> doped TiO<sub>2</sub> nanoplates. *Industrial & Engineering Chemistry Research* **49**, 1480-1485 (2010).
- 46 Zhou, J., Takeuchi, M., Ray, A. K., Anpo, M. & Zhao, X. Enhancement of photocatalytic activity of P<sub>25</sub>TiO<sub>2</sub> by vanadium-ion implantation under visible light irradiation. *Journal of colloid and interface science* **311**, 497-501 (2007).
- 47 Asahi, R., Morikawa, T., Ohwaki, T., Aoki, K. & Taga, Y. Visible-light photocatalysis in nitrogen-doped titanium oxides. *science* **293**, 269-271 (2001).
- 48 Senthilnathan, J. & Philip, L. Photocatalytic degradation of lindane under UV and visible light using N-doped TiO<sub>2</sub>. *Chemical engineering journal* **161**, 83-92 (2010).
- 49 Irie, H., Watanabe, Y. & Hashimoto, K. Carbon-doped anatase TiO<sub>2</sub> powders as a visible-light sensitive photocatalyst. *Chemistry Letters* **32**, 772-773 (2003).
- 50 Umabayashi, T., Yamaki, T., Tanaka, S. & Asai, K. Visible light-induced degradation of methylene blue on S-doped TiO<sub>2</sub>. *Chemistry Letters* **32**, 330-331 (2003).
- 51 Dong, X., Tao, J., Li, Y. & Zhu, H. Enhanced photoelectrochemical properties of F-containing TiO<sub>2</sub> sphere thin film induced by its novel hierarchical structure. *Applied Surface Science* **255**, 7183-7187 (2009).
- 52 Lin, Z., Orlov, A., Lambert, R. M. & Payne, M. C. New insights into the origin of visible light photocatalytic activity of nitrogen-doped and oxygen-deficient anatase TiO<sub>2</sub>. *The journal of physical chemistry B* **109**, 20948-20952 (2005).
- 53 Wang, H. & Lewis, J. P. Effects of dopant states on photoactivity in carbon-doped TiO<sub>2</sub>. *Journal of Physics: Condensed Matter* **17**, L209 (2005).
- 54 Tauc, J., Grigorovici, R. & Vancu, A. Optical properties and electronic structure of amorphous germanium. *physica status solidi (b)* **15**, 627-637 (1966).
- 55 Sosnowska, I., Neumaier, T. P. & Steichele, E. Spiral magnetic ordering in bismuth ferrite. *Journal of Physics C: Solid State Physics* **15**, 4835 (1982).

- 56 Matsumoto, Y. et al. Room-temperature ferromagnetism in transparent transition metal-doped titanium dioxide. *Science* **291**, 854-856 (2001).
- 57 Du, X., Li, Q., Su, H. & Yang, J. Electronic and magnetic properties of V-doped anatase TiO<sub>2</sub> from first principles. *Physical Review B* **74**, 233201 (2006).
- 58 Bryan, J. D., Santangelo, S. A., Keveren, S. C. & Gamelin, D. R. Activation of high-TC ferromagnetism in Co<sup>2+</sup>: TiO<sub>2</sub> and Cr<sup>3+</sup>: TiO<sub>2</sub> nanorods and nanocrystals by grain boundary defects. *Journal of the American Chemical Society* **127**, 15568-15574 (2005).
- 59 Mallia, G. & Harrison, N. Magnetic moment and coupling mechanism of iron-doped rutile TiO<sub>2</sub> from first principles. *Physical Review B* **75**, 165201 (2007).
- 60 Griffin, K., Varela, M., Pennycook, S. J., Pakhomov, A. & Krishnan, K. M. Atomic-scale studies of cobalt distribution in Co–TiO<sub>2</sub> anatase thin films: Processing, microstructure, and the origin of ferromagnetism. *Journal of applied physics* **99**, 08M114 (2006).
- 61 Zhang, L. et al. Interfacial effect on Mn-doped TiO<sub>2</sub> nanoparticles: from paramagnetism to ferromagnetism. *RSC Advances* **6**, 57403-57408 (2016).
- 62 Lu, J., Yang, K., Jin, H., Dai, Y. & Huang, B. First-principles study of the electronic and magnetic properties of oxygen-deficient rutile TiO<sub>2</sub> (1 1 0) surface. *Journal of Solid State Chemistry* **184**, 1148-1152 (2011).
- 63 Dong-Xiang, L. et al. Defect types and room-temperature ferromagnetism in undoped rutile TiO<sub>2</sub> single crystals. *Chinese Physics B* **22**, 037504 (2013).
- 64 von Oertzen, G. U. & Gerson, A. R. The effects of O deficiency on the electronic structure of rutile TiO<sub>2</sub>. *Journal of Physics and Chemistry of Solids* **68**, 324-330 (2007).
- 65 Álvarez, P. M., Jaramillo, J., Lopez-Pinero, F. & Plucinski, P. K. Preparation and characterization of magnetic TiO<sub>2</sub> nanoparticles and their utilization for the degradation of emerging pollutants in water. *Applied Catalysis B: Environmental* **100**, 338-345 (2010).
- 66 Morgan, B. J. & Watson, G. W. Intrinsic n-type defect formation in TiO<sub>2</sub>: a comparison of rutile and anatase from GGA+ U calculations. *The Journal of Physical Chemistry C* **114**, 2321-2328 (2010).
- 67 Walsh, A. & Catlow, C. R. A. Photostimulated reduction processes in a titania hybrid metal–organic framework. *ChemPhysChem* **11**, 2341-2344 (2010).
- 68 Lee, E.-J. & Pyun, S.-I. Analysis of nonlinear Mott-Schottky plots obtained from anodically passivating amorphous and polycrystalline TiO<sub>2</sub> films. *Journal of applied electrochemistry* **22**, 156-160 (1992).
- 69 Enache, C. S., Schoonman, J. & Van Krol, R. The photoresponse of iron- and carbon-doped TiO<sub>2</sub> (anatase) photoelectrodes. *Journal of electroceramics* **13**, 177-182 (2004).



- 70 Manurung, P., Putri, Y., Simanjuntak, W. & Low, I. M. Synthesis and characterisation of chemical bath deposited TiO<sub>2</sub> thin-films. *Ceramics International* **39**, 255-259 (2013).
- 71 Wang, Z. et al. Ferromagnetism in chromium-doped reduced-rutile titanium dioxide thin films. *Journal of applied physics* **95**, 7381-7383 (2004).
- 72 Yoon, S. D. et al. Oxygen-defect-induced magnetism to 880 K in semiconducting anatase TiO<sub>2- $\delta$</sub>  films. *Journal of Physics: Condensed Matter* **18**, L355 (2006).
- 73 Fujishima, A., Rao, T. N. & Tryk, D. A. Titanium dioxide photocatalysis. *Journal of photochemistry and photobiology C: Photochemistry reviews* **1**, 1-21 (2000).
- 74 Zaleska, A. Doped-TiO<sub>2</sub>: a review. *Recent patents on engineering* **2**, 157-164 (2008).
- 75 Chen, Y., Sun, Z., Yang, Y. & Ke, Q. Heterogeneous photocatalytic oxidation of polyvinyl alcohol in water. *Journal of Photochemistry and Photobiology A: Chemistry* **142**, 85-89 (2001).
- 76 Asiltürk, M., Sayılkan, F. & Arpaç, E. Effect of Fe<sup>3+</sup> ion doping to TiO<sub>2</sub> on the photocatalytic degradation of Malachite Green dye under UV and vis-irradiation. *Journal of Photochemistry and Photobiology A: Chemistry* **203**, 64-71 (2009).
- 77 Li, Z., Shen, W., He, W. & Zu, X. Effect of Fe-doped TiO<sub>2</sub> nanoparticle derived from modified hydrothermal process on the photocatalytic degradation performance on methylene blue. *Journal of Hazardous Materials* **155**, 590-594 (2008).
- 78 Hung, W.-C., Chen, Y.-C., Chu, H. & Tseng, T.-K. Synthesis and characterization of TiO<sub>2</sub> and Fe/TiO<sub>2</sub> nanoparticles and their performance for photocatalytic degradation of 1, 2-dichloroethane. *Applied Surface Science* **255**, 2205-2213 (2008).
- 79 Choi, W., Termin, A. & Hoffmann, M. R. The role of metal ion dopants in quantum-sized TiO<sub>2</sub>: correlation between photoreactivity and charge carrier recombination dynamics. *The Journal of Physical Chemistry* **98**, 13669-13679 (1994).
- 80 Teoh, W. Y., Amal, R., Mädler, L. & Pratsinis, S. E. Flame sprayed visible light-active Fe-TiO<sub>2</sub> for photomineralisation of oxalic acid. *Catalysis Today* **120**, 203-213 (2007).
- 81 Wolf, S. et al. Spintronics: a spin-based electronics vision for the future. *Science* **294**, 1488-1495 (2001).
- 82 Kim, D. et al. Investigations on the nature of observed ferromagnetism and possible spin polarization in Co-doped anatase TiO<sub>2</sub> thin films. *Journal of Applied Physics* **93**, 6125-6132 (2003).
- 83 Okuya, M., Prokudina, N. A., Mushika, K. & Kaneko, S. TiO<sub>2</sub> thin films synthesized by the spray pyrolysis deposition (SPD) technique. *Journal of the European Ceramic Society* **19**, 903-906 (1999).
- 84 Murakami, K., Yagi, I. & Kaneko, S. Oriented growth of tin oxide thin films on glass substrates by spray pyrolysis of organotin compounds. *Journal of the American Ceramic Society* **79**, 2557-2562 (1996).

- 85 Miotello, A. & Ossi, P. M. Laser-surface interactions for new materials production. Vol. 130 (Springer, 2010).
- 86 Livage, J., Henry, M. & Sanchez, C. Sol-gel chemistry of transition metal oxides. Progress in solid state chemistry **18**, 259-341 (1988).
- 87 Aldebert, P., Baffier, N., Gharbi, N. & Livage, J. Layered structure of vanadium pentoxide gels. Materials Research Bulletin **16**, 669-676 (1981).
- 88 Mechiakh, R. et al. TiO<sub>2</sub> thin films prepared by sol-gel method for waveguiding applications: correlation between the structural and optical properties. Optical Materials **30**, 645-651 (2007).
- 89 Dholam, R., Patel, N., Adami, M. & Miotello, A. Hydrogen production by photocatalytic water-splitting using Cr-or Fe-doped TiO<sub>2</sub> composite thin films photocatalyst. International Journal of Hydrogen Energy **34**, 5337-5346 (2009).
- 90 Xu, W.-X., Zhu, S. & Fu, X.-C. XPS study of TiO<sub>x</sub> thin films deposited on glass substrates by the sol-gel process. Applied surface science **136**, 194-205 (1998).
- 91 Chaput, F., Boilot, J. P. & Beauger, A. Alkoxide-Hydroxide Route to Synthetize BaTiO<sub>3</sub>-Based Powders. Journal of the American Ceramic Society **73**, 942-948 (1990).
- 92 Jun, Y.-K. & Hong, S.-H. Dielectric and magnetic properties in Co-and Nb-substituted BiFeO<sub>3</sub> ceramics. Solid State Communications **144**, 329-333 (2007).
- 93 Kumar, M. & Yadav, K. Rapid liquid phase sintered Mn doped BiFeO<sub>3</sub> ceramics with enhanced polarization and weak magnetization. Applied physics letters **91**, 242901 (2007).
- 94 Islam, M. R. et al. Evidence of superparamagnetism and improved electrical properties in Ba and Ta co-doped BiFeO<sub>3</sub> ceramics. Journal of Alloys and Compounds **735**, 2584-2596 (2018).
- 95 Kim, J. K., Kim, S. S., Kim, W.-J., Bhalla, A. S. & Guo, R. Enhanced ferroelectric properties of Cr-doped BiFeO<sub>3</sub> thin films grown by chemical solution deposition. Applied physics letters **88**, 132901 (2006).
- 96 Cazayous, M., Malka, D., Lebeugle, D. & Colson, D. Electric field effect on BiFeO<sub>3</sub> single crystal investigated by Raman spectroscopy. Applied Physics Letters **91**, 071910 (2007).
- 97 Kubel, F. & Schmid, H. Structure of a ferroelectric and ferroelastic monodomain crystal of the perovskite BiFeO<sub>3</sub>. Acta Crystallographica Section B: Structural Science **46**, 698-702 (1990).
- 98 Palewicz, A., Sosnowska, I., Przenioslo, R. & Hewat, A. BiFeO<sub>3</sub> crystal structure at low temperatures. Acta Physica Polonica-Series A General Physics **117**, 296 (2010).

- 99 Shannon, R. D. Revised effective ionic radii and systematic studies of interatomic distances in halides and chalcogenides. *Acta crystallographica section A: crystal physics, diffraction, theoretical and general crystallography* **32**, 751-767 (1976).
- 100 Anderson, P. Antiferromagnetism. Theory of superexchange interaction. *Physical Review* **79**, 350 (1950).
- 101 Smolenskii, G. & Chupis, I. Ferroelectromagnets. *Soviet Physics Uspekhi* **25**, 475 (1982).
- 102 Ortiz-Quiñonez, J. L. et al. Easy synthesis of high-purity BiFeO<sub>3</sub> nanoparticles: new insights derived from the structural, optical, and magnetic characterization. *Inorganic chemistry* **52**, 10306-10317 (2013).
- 103 Nalwa, K., Garg, A. & Upadhyaya, A. Effect of samarium doping on the properties of solid-state synthesized multiferroic bismuth ferrite. *Materials Letters* **62**, 878-881 (2008).
- 104 Lahmar, A. et al. Off-stoichiometry effects on BiFeO<sub>3</sub> thin films. *Solid State Ionics* **202**, 1-5 (2011).
- 105 Basu, S. et al. Photoconductivity in BiFeO<sub>3</sub> thin films. *Applied Physics Letters* **92**, 091905 (2008).
- 106 Basith, M. et al. The 10% Gd and Ti co-doped BiFeO<sub>3</sub>: a promising multiferroic material. *Journal of Alloys and Compounds* **694**, 792-799 (2017).
- 107 Zhang, X., Sui, Y., Wang, X., Wang, Y. & Wang, Z. Effect of Eu substitution on the crystal structure and multiferroic properties of BiFeO<sub>3</sub>. *Journal of Alloys and Compounds* **507**, 157-161 (2010).
- 108 Rangi, M. et al. Crystal structure and magnetic properties of Bi<sub>0.8</sub>A<sub>0.2</sub>FeO<sub>3</sub> (A= La, Ca, Sr, Ba) multiferroics using neutron diffraction and Mossbauer spectroscopy. *AIP Advances* **4**, 087121 (2014).
- 109 Song, G. et al. Crystal structure refinement, ferroelectric and ferromagnetic properties of Ho<sup>3+</sup> modified BiFeO<sub>3</sub> multiferroic material. *Journal of Alloys and Compounds* **696**, 503-509 (2017).
- 110 Li, K., Wang, D., Wu, F., Xie, T. & Li, T. Surface electronic states and photovoltage gas-sensitive characters of nanocrystalline LaFeO<sub>3</sub>. *Materials chemistry and physics* **64**, 269-272 (2000).
- 111 VON KUBELKA, P. Ein Beitrag zur Optik der Farbanstriche. *Zeitschrift für technische Physik*, 593-601 (1931).
- 112 Zhou, W. et al. Effects of Sm and Mn co-doping on structural, optical and magnetic properties of BiFeO<sub>3</sub> films prepared by a sol-gel technique. *Materials Letters* **144**, 93-96 (2015).

- 113 Gao, N. et al. First principles investigation on the electronic, magnetic and optical properties of  $\text{Bi}_{0.8}\text{M}_{0.2}\text{Fe}_{0.9}\text{Co}_{0.1}\text{O}_3$  (M= La, Gd, Er, Lu). *Computational and Theoretical Chemistry* **1084**, 36-42 (2016).
- 114 Zhang, Z., Wu, P., Chen, L. & Wang, J. Systematic variations in structural and electronic properties of  $\text{BiFeO}_3$  by A-site substitution. *Applied Physics Letters* **96**, 012905 (2010).
- 115 Jang, H. et al. Epitaxial (001)  $\text{BiFeO}_3$  membranes with substantially reduced fatigue and leakage. *Applied Physics Letters* **92**, 062910 (2008).
- 116 Lou, X. et al. Formation of magnetite in bismuth ferrite under voltage stressing. *Applied physics letters* **90**, 262908 (2007).
- 117 Woodward, D. I., Reaney, I. M., Eitel, R. E. & Randall, C. A. Crystal and domain structure of the  $\text{BiFeO}_3$ - $\text{PbTiO}_3$  solid solution. *Journal of applied physics* **94**, 3313-3318 (2003).
- 118 Fujino, S. et al. Combinatorial discovery of a lead-free morphotropic phase boundary in a thin-film piezoelectric perovskite. *Applied Physics Letters* **92**, 202904 (2008).
- 119 Béa, H., Gajek, M., Bibes, M. & Barthélémy, A. Spintronics with multiferroics. *Journal of Physics: Condensed Matter* **20**, 434221 (2008).
- 120 Lebeugle, D. et al. Electric-field-induced spin flop in  $\text{BiFeO}_3$  single crystals at room temperature. *Physical review letters* **100**, 227602 (2008).
- 121 Laukhin, V. et al. Electric-field control of exchange bias in multiferroic epitaxial heterostructures. *Physical review letters* **97**, 227201 (2006).
- 122 Dho, J., Qi, X., Kim, H., MacManus-Driscoll, J. L. & Blamire, M. G. Large electric polarization and exchange bias in multiferroic  $\text{BiFeO}_3$ . *Advanced Materials* **18**, 1445-1448 (2006).
- 123 Chu, Y.-H. et al. Electric-field control of local ferromagnetism using a magnetoelectric multiferroic. *Nature materials* **7**, 478 (2008).
- 124 Bibes, M. & Barthélémy, A. Multiferroics: Towards a magnetoelectric memory. *Nature materials* **7**, 425 (2008).
- 125 Catalan, G. & Scott, J. F. Physics and applications of bismuth ferrite. *Advanced Materials* **21**, 2463-2485 (2009).
- 126 Madhu, C., Bellakki, M. B. & Manivannan, V. Synthesis and characterization of cation-doped  $\text{BiFeO}_3$  materials for photocatalytic applications. (2010).
- 127 Li, S. et al. Microwave-assisted synthesis of  $\text{BiFeO}_3$  nanoparticles with high catalytic performance in microwave-enhanced Fenton-like process. *RSC Advances* **6**, 82439-82446 (2016).

- 128 Shami, M. Y., Awan, M. & Anis-ur-Rehman, M. Phase pure synthesis of BiFeO<sub>3</sub> nanopowders using diverse precursor via co-precipitation method. *Journal of Alloys and Compounds* **509**, 10139-10144 (2011).
- 129 Gao, T. et al. Synthesis of BiFeO<sub>3</sub> nanoparticles for the visible-light induced photocatalytic property. *Materials Research Bulletin* **59**, 6-12 (2014).
- 130 Legrand-Buscema, C., Malibert, C. & Bach, S. Elaboration and characterization of thin films of TiO<sub>2</sub> prepared by sol-gel process. *Thin solid films* **418**, 79-84 (2002).
- 131 Rodriguez-Carvajal, J. in satellite meeting on powder diffraction of the XV congress of the IUCr. (Toulouse, France:[sn]).
- 132 ICSD code-154604.
- 133 Qi, Y., Alima, B. & Shifeng, Z. Lattice distortion of holmium doped bismuth ferrite nanofilms. *Journal of Rare Earths* **32**, 884-889 (2014).
- 134 Hussain, S. et al. Size and lone pair effects on the multiferroic properties of Bi<sub>0.75</sub>A<sub>0.25</sub>FeO<sub>3-δ</sub> (A= Sr, Pb, and Ba) ceramics. *Journal of the American Ceramic Society* **96**, 3141-3148 (2013).
- 135 Jayakumar, O. et al. Theoretical and experimental evidence of enhanced ferromagnetism in Ba and Mn cosubstituted BiFeO<sub>3</sub>. *Applied Physics Letters* **96**, 032903 (2010).
- 136 Khomchenko, V. et al. Intrinsic nature of the magnetization enhancement in heterovalently doped Bi<sub>1-x</sub>A<sub>x</sub>FeO<sub>3</sub> (A= Ca, Sr, Pb, Ba) multiferroics. *Journal of Physics D: Applied Physics* **41**, 102003 (2008).
- 137 Hou, Z.-L. et al. Enhanced ferromagnetism and microwave absorption properties of BiFeO<sub>3</sub> nanocrystals with Ho substitution. *Materials Letters* **84**, 110-113 (2012).
- 138 Pradhan, S. & Roul, B. Effect of Gd doping on structural, electrical and magnetic properties of BiFeO<sub>3</sub> electroceramic. *Journal of Physics and Chemistry of Solids* **72**, 1180-1187 (2011).
- 139 Ladd, M. F. C., Palmer, R. A. & Palmer, R. A. *Structure determination by X-ray crystallography*. (Springer, 1985).
- 140 Munir, S., Shah, S. M. & Hussain, H. Effect of carrier concentration on the optical band gap of TiO<sub>2</sub> nanoparticles. *Materials & Design* **92**, 64-72 (2016).
- 141 Shah, S., Li, W., Huang, C.-P., Jung, O. & Ni, C. Study of Nd<sup>3+</sup>, Pd<sup>2+</sup>, Pt<sup>4+</sup>, and Fe<sup>3+</sup> dopant effect on photoreactivity of TiO<sub>2</sub> nanoparticles. *Proceedings of the National Academy of Sciences* **99**, 6482-6486 (2002).
- 142 Nguyen, V. N., Nguyen, N. K. T. & Nguyen, P. H. Hydrothermal synthesis of Fe-doped TiO<sub>2</sub> nanostructure photocatalyst. *Advances in Natural Sciences: Nanoscience and Nanotechnology* **2**, 035014 (2011).

- 143 Shannon, R. T. & Prewitt, C. T. Effective ionic radii in oxides and fluorides. *Acta Crystallographica Section B: Structural Crystallography and Crystal Chemistry* **25**, 925-946 (1969).
- 144 Beer, A. Bestimmung der absorption des rothen lichts in farbigen flussigkeiten. *Ann. Physik* **162**, 78-88 (1852).
- 145 Lambert, J. H. *Photometria sive de mensura et gradibus luminis, colorum et umbrae.* (Klett, 1760).
- 146 Nagaveni, K., Hegde, M. & Madras, G. Structure and Photocatalytic Activity of  $Ti_{1-x}M_xO_{2+\delta}$  (M= W, V, Ce, Zr, Fe, and Cu) Synthesized by Solution Combustion Method. *The Journal of Physical Chemistry B* **108**, 20204-20212 (2004).
- 147 Moriguchi, I., Maeda, H., Teraoka, Y. & Kagawa, S. Preparation of  $TiO_2$  ultrathin film by newly developed two-dimensional sol-gel process. *Journal of the American Chemical Society* **117**, 1139-1140 (1995).
- 148 Mocherla, P. S., Karthik, C., Ubig, R., Ramachandra Rao, M. & Sudakar, C. Tunable bandgap in  $BiFeO_3$  nanoparticles: the role of microstrain and oxygen defects. *Applied Physics Letters* **103**, 022910 (2013).
- 149 Medarde, M. et al. High-pressure neutron-diffraction study of the metallization process in  $PrNiO_3$ . *Physical Review B* **52**, 9248 (1995).
- 150 Tang, H., Prasad, K., Sanjines, R., Schmid, P. & Levy, F. Electrical and optical properties of  $TiO_2$  anatase thin films. *Journal of applied physics* **75**, 2042-2047 (1994).
- 151 Ahamed, M., Khan, M. M., Akhtar, M. J., Alhadlaq, H. A. & Alshamsan, A. Ag-doping regulates the cytotoxicity of  $TiO_2$  nanoparticles via oxidative stress in human cancer cells. *Scientific reports* **7**, 17662 (2017).
- 152 Luo, J. & Maggard, P. A. Hydrothermal Synthesis and Photocatalytic Activities of  $SrTiO_3$ -Coated  $Fe_2O_3$  and  $BiFeO_3$ . *Advanced Materials* **18**, 514-517 (2006).
- 153 Kim, Y. I., Atherton, S. J., Brigham, E. S. & Mallouk, T. E. Sensitized layered metal oxide semiconductor particles for photochemical hydrogen evolution from nonsacrificial electron donors. *The Journal of Physical Chemistry* **97**, 11802-11810 (1993).
- 154 Butler, M. & Ginley, D. Prediction of flatband potentials at semiconductor-electrolyte interfaces from atomic electronegativities. *Journal of the Electrochemical Society* **125**, 228-232 (1978).
- 155 Rashti, M. & Brodie, D. The photoresponse of high resistance anatase  $TiO_2$  films prepared by the decomposition of titanium isopropoxide. *Thin Solid Films* **240**, 163-167 (1994).
- 156 Perejón, A. et al. Preparation of phase pure, dense fine grained ceramics by conventional and spark plasma sintering of La-substituted  $BiFeO_3$  nanoparticles. *Journal of the European Ceramic Society* **35**, 2283-2293 (2015).

- 157 Perejón, A. et al. Single phase, electrically insulating, multiferroic La-substituted BiFeO<sub>3</sub> prepared by mechano-synthesis. *Journal of Materials Chemistry C* **2**, 8398-8411 (2014).
- 158 Song, G. et al. Effect of Ho<sup>3+</sup> doping on the electric, dielectric, ferromagnetic properties and TC of BiFeO<sub>3</sub> ceramics. *Ceramics International* **40**, 3579-3587 (2014).
- 159 Neaman, D. A. *Semiconductor physics and devices*. (Irwin Chicago, 1992).
- 160 Yasuno, S. et al. Physical properties of amorphous In–Ga–Zn–O films deposited at different sputtering pressures. *Japanese Journal of Applied Physics* **52**, 03BA01 (2013).
- 161 Trinh, T. T., Jang, K., Velumani, S., Dao, V. A. & Yi, J. Role of Schottky barrier height at source/drain contact for electrical improvement in high carrier concentration amorphous InGaZnO thin film transistors. *Materials Science in Semiconductor Processing* **38**, 50-56 (2015).
- 162 Coey, J., Venkatesan, M. & Fitzgerald, C. Donor impurity band exchange in dilute ferromagnetic oxides. *Nature materials* **4**, 173-179 (2005).
- 163 Zhao, T. et al. Electric field effect in diluted magnetic insulator anatase Co: TiO<sub>2</sub>. *Physical review letters* **94**, 126601 (2005).
- 164 García, M. et al. Interface double-exchange ferromagnetism in the Mn-Zn-O system: new class of biphasic magnetism. *Physical review letters* **94**, 217206 (2005).
- 165 Choudhury, B. & Choudhury, A. Room temperature ferromagnetism in defective TiO<sub>2</sub> nanoparticles: Role of surface and grain boundary oxygen vacancies. *Journal of Applied Physics* **114**, 203906 (2013).